UNIVERSITÀ DEGLI STUDI
DI MODENA E REGGIO EMILIA

Dottorato di ricerca in Ingegneria Industriale e del Territorio/ Industrial and Environmental Engineering

Ciclo XXXIV

CMAS corrosion resistance of thermal barrier coatings (TBCs): influence of the coating microstructure, materials and architecture

RESISTENZA A CORROSIONE DA CMAS DI BARRIERE TERMICHE (TBCs): INFLUENZA DELLA MICROSTRUTTURA, MATERIALI E ARCHITETTURA DEL RIVESTIMENTO

Candidato: Stefania Morelli

Relatore (Tutor): Prof. Luca Lusvarghi

Correlatore (Co-Tutor): Dr. Ing. Giovanni Bolelli

Coordinatore del Corso di Dottorato: Prof. Alberto Muscio

Contents

Summary (English version)

Thermal barrier coatings (TBCs) are refractory oxide ceramic coatings applied on metallic components (combustion liner; transition piece; blades and vanes; shrouds; etc.) in the hot section of industrial gas turbines (IGT), where gas temperatures are higher than the melting point of the metallic substrates or too high for the metallic components to retain adequate mechanical properties without a proper thermal insulation. TBCs provide the required thermal insulation for the underlying metal parts: acting in synergy with an internal air-cooling system, TBCs reduce the temperatures of the metal down to tolerable levels.

The "state of the art" for TBCs is 7-8 wt.% (≈ 3.5 mol.%) Y_2O_3-stabilized zirconia (YSZ) whose high melting point (2690 °C), phase stability up to 1200 °C, and low thermal conductivity match the technical requirements. In industrial gas turbines for the production of electric energy, a typical coating system comprises a bi-layer architecture, where a porous, thermally insulating YSZ layer is deposited by plasma spraying onto a metallic bond coat (MCrAlY alloys, M = Ni, Co or NiCo) which protects the superalloy substrate against oxidation and improves the top layer adhesion. During exposure to high temperatures and an oxidizing atmosphere, between these two layers, a further layer called thermally grown oxide (TGO) made of α-Al_2O_3 is formed by oxidation of the MCrAlY bond coat.

Failure of TBCs during service can be due either to the cyclic thermal stresses induced by starting and stopping the turbine, which cause the nucleation and growth of delamination cracks, or by chemical degradation. Specifically, when gas turbines operate in dusty environments, they can ingest silicate powders, which then form molten deposits based on CaO-MgO-Al_2O_3-SiO_2 (CMAS) mixtures on the surface of hot-section components. Chemical and mechanical issues can be associated to CMAS infiltration into a YSZ coating, leading to its delamination. The present work is especially focused on studying TBC systems with improved chemical resistance to molten CMAS deposits.

- The first part of this Thesis studies the infiltration behaviour and reaction mechanism between the CMAS deposit and 8YSZ coatings with various kinds of microstructures: a porous layer deposited by atmospheric plasma spraying (APS) of standard and high-purity YSZ feedstock; a dense-vertically cracked (DVC) APS layer; and a columnar YSZ coating obtained by suspension plasma spraying (SPS). All were deposited on the same type of High Velocity Oxygen Fuel (HVOF) sprayed MCrAlY bond coat. In

general, it was found that CMAS dissolves YSZ along the grain boundaries and proceeding towards the inner microstructure. The intensity of the attack is affected by the different microstructures and chemical purity of the coatings. When comparing the microstructures, it was observed that the combination of high porosity and fine grain sizes leads to a sever chemical attack. For each microstructure the following considerations can be made:

In the **APS porous layer,** fine-grained regions produced by molten YSZ particles are more severely attacked than coarse-grained.

The **SPS columnar layer** shows the most severe degradation. CMAS penetrated along intercolumnar gaps, infiltrated the abundant intra-columnar porosity, and corroded the boundaries among the small 8YSZ grains, which are much finer than in all APS coatings. Small grains are thus separated from one another, and the mechanical integrity of the coating is compromised.

DVC-APS coating, denser than other coatings, does not offer easy access to the CMAS melt. In this case the degradation proceeded in a slower way compared to other microstructures. The main issue for the DVC-APS sample is, however, the large-scale penetration of CMAS into the segmentation cracks. As CMAS solidifies during cooling, it compromises the compliance of the coating and causes "cold shock".

Comparing the chemical purity of the feedstock materials, it was found that a low-purity material accelerates the dissolution by molten CMAS. According to the literature, impurities tend to concentrate mainly along grain boundaries, exactly where CMAS starts to dissolve YSZ. This explains why the presence of impurities can facilitate the dissolution by CMAS.

- In the second part of this work, having established the DVC microstructure as the most promising for improved resistance to CMAS corrosion, tests were carried out on three promising coating materials with potentially improved durability in contact with molten CMAS: Gd/Yb/Y co-doped ZrO_2, Gd_2ZrO_7 and ZrO_2-55 wt.%Y_2O_3. All were manufactured as DVC layers on the same type of HVOF-sprayed MCrAlY bond coat. Porous and DVC 8YSZ were employed as terms of comparison. In addition, six ceramic bilayers systems were also tested, where 8YSZ with either porous or DVC microstructure was employed as a bottom layer under a DVC top layer of either Gd/Yb/Y co-doped ZrO_2, Gd_2ZrO_7 or ZrO_2-55 wt.%Y_2O_3. These systems were

subjected to CMAS corrosion tests and thermal cycling fatigue (TCF) tests. Although none of the alternative materials exhibited the same thermal cycling fatigue resistance of porous 8YSZ, multilayered coatings showed longer thermal cycling fatigue life compared to monolayer coatings. On the other hand, CMAS tests showed that the novel materials do exhibit improved corrosion resistance. DVC Gd_2ZrO_7 layers, in particular, exhibited excellent CMAS corrosion resistance because the formation of a solid Gd-apatite layer at the interface with molten CMAS blocked further reaction and slowed down CMAS penetration. Whilst pure Gd_2ZrO_7 would not be usable as a TBC due to its poor TCF resistance, the combination of a Gd_2ZrO_7 top layer with a porous 8YSZ bottom layer shows enhanced resistance to thermal cycling fatigue. Although the bi-layer system does not attain the same TCF resistance of pure YSZ, the combination between reasonable TCF life and excellent CMAS resistance (far superior to either porous of DVC 8YSZ) makes it a good choice for turbines operating in demanding environmental conditions.

Summary (Italian version)

Le barriere termiche (TBC) sono rivestimenti ceramici applicati su componenti metallici nelle sezioni calde delle turbine a gas industriali (IGT). In esse, le temperature dei gas sono tali da far diminuire le proprietà meccaniche dei substrati metallici così tanto da non rispettare i requisiti tecnici o addirittura sono superiori al loro punto di fusione. Le TBC forniscono isolamento termico alle parti metalliche sottostanti: agendo in sinergia con un sistema interno di raffreddamento ad aria, le TBC riducono le temperature superficiali del metallo.

Lo "stato dell'arte" delle TBC è rappresentato dalla zirconia stabilizzata con il 7-8% (≈ 3.5 mol. %) in peso di Y_2O_3 (YSZ) che ha un alto punto di fusione (2690 °C), una stabilità di fase sopra i 1200 °C, e bassa conducibilità termica. Nelle turbine a gas industriali per la produzione di energia elettrica, un tipico sistema di rivestimento comprende un'architettura a doppio strato, in cui uno strato YSZ poroso e termoisolante è depositato mediante spruzzatura al plasma su un *bond coat* metallico (leghe MCrAlY, M = Ni, Co o NiCo) che protegge il substrato di superlega dall'ossidazione e migliora l'adesione dello strato superiore. Durante l'esposizione ad alte temperature, tra questi due strati, si forma, per ossidazione del *bond coat*, uno strato chiamato *thermally grown oxide* (TGO) costituito da α-Al_2O_3. Il cedimento delle TBC può essere dovuto sia a sollecitazioni termiche cicliche indotte dall'accensione e spegnimento delle turbine, che provocano la nucleazione e la crescita di cricche, sia alla degradazione chimica. Quando le turbine a gas operano in ambienti polverosi, possono ingerire polveri di silicati, che poi formano depositi fusi a base di miscele di CaO-MgO-Al_2O_3-SiO_2 (CMAS) sulla superficie dei componenti delle parti calde. Problemi di natura chimica e meccanica sono associati all'infiltrazione della CMAS all'interno del rivestimento YSZ, causando la delaminazione di quest'ultimo.

Il presente lavoro è incentrato sullo studio di sistemi TBC con una maggiore resistenza chimica ai depositi di CMAS.

La prima parte di questa tesi studia l'infiltrazione e il meccanismo di reazione tra la CMAS e i rivestimenti 8YSZ con diverse microstrutture: porose ottenute tramite *atmospheric plasma spraying (APS)* utilizzando materie prime a standard e ad elevata purezza*; dense-vertically cracked (DVC) APS*; microstrutture colonnari ottenute tramite *suspension plasma spraying (SPS)*. È stato riscontrato che la CMAS attacca la YSZ dissolvendo i suoi bordi grano e che l'utilizzo di un materiale a bassa purezza accelera la dissoluzione.

L’intensità dell’attacco dipende dalle diverse microstrutture e dalla purezza chimica dei rivestimenti. Confrontando le microstrutture, è stato osservato che la combinazione dell’alta porosità e la presenza di grani di dimensioni fini, porta ad un severo attacco chimico. Per ogni microstruttura sono state fatte le seguenti considerazioni:

Nel **rivestimento APS-poroso**, le regioni a grana fine prodotte da particelle YSZ fuse sono state attaccate in maniera più severa rispetto a quelle a grana grossa.

Il **rivestimento SPS colonnare** mostra la degradazione più severa. La CMAS è penetrata lungo gli spazi inter-colonnari, è infiltrata all’interno dell’abbondante porosità intra-colonnare, e ha corroso i bordi grano dell’8YSZ. I rivestimenti SPS presentano una microstruttura con grani più fini rispetto ai rivestimenti APS. L’integrità meccanica del rivestimento è compromessa in quanto, dopo attacco corrosivo, i grani risultano essere separati tra di loro.

Il **rivestimento DVC-APS**, più denso degli altri rivestimenti, non offre un facile accesso alla CMAS fusa. In questo caso la degradazione procede in maniera più lenta rispetto ad altre microstrutture. Il problema principale per il campione DVC-APS è, tuttavia, la penetrazione su larga scala di CMAS nelle crepe di segmentazione. Poiché la CMAS solidifica durante il raffreddamento, provoca “cold shock”, compromettendo la conformità del rivestimento.

Confrontando la purezza chimica delle materie prime, è stato riscontrato che un materiale a bassa purezza accelera la dissoluzione da parte del CMAS fuso. Secondo letteratura, le impurità tendono a concentrarsi principalmente lungo i bordi dei grani, esattamente dove la CMAS inizia a dissolvere la YSZ. Questo spiega perché la presenza di impurità può favorire la dissoluzione da parte del CMAS.

Nella seconda parte di questo lavoro, dopo aver identificato la microstruttura DVC come la più promettente in termini di resistenza a corrosione da CMAS, sono stati effettuati test su tre rivestimenti composti da materiali potenzialmente interessanti per il loro comportamento a contatto con CMAS: ZrO_2 drogata con Gd/Yb/Y, Gd_2ZrO_7 e ZrO_2 con 55% in peso di Y_2O_3. Tutti sono stati prodotti con una microstruttura DVC e depositati sullo stesso tipo di bond coat. Rivestimenti 8YSZ porosi e DVC sono stati utilizzati come termine di confronto. Inoltre, sono stati testati sei sistemi a doppio strato, in cui la 8YSZ con microstruttura porosa o DVC è stata impiegata come strato inferiore ad uno strato DVC di Gd/Yb/Y, Gd_2ZrO_7 e ZrO_2 con 55% in

peso di Y_2O_3. Questi sistemi sono stati sottoposti a test di corrosione CMAS e test di ciclaggio termico (TCF).

I rivestimenti multistrato hanno mostrato una durata a TCF più lunga rispetto ai rivestimenti monostrato. D'altra parte, i test CMAS hanno rivelato che i nuovi materiali hanno una migliore resistenza alla corrosione. Il DVC Gd_2ZrO_7, ha mostrato un'eccellente resistenza alla corrosione CMAS dovuta alla formazione di uno strato solido di Gd-apatite all'interfaccia con CMAS fusa che blocca l'ulteriore reazione e rallentata la penetrazione di CMAS. La combinazione di uno strato superiore di Gd_2ZrO_7 con uno strato inferiore poroso 8YSZ comporta una maggiore resistenza a TCF. Sebbene il sistema a doppio strato non raggiunga la stessa resistenza TCF del puro YSZ, la combinazione tra una ragionevole durata a TCF e un'eccellente resistenza CMAS lo rende una buona scelta per le turbine che operano in condizioni ambientali ostili.

Aim of the thesis

The topic of this research was to examine the degradation mechanisms of thermal barrier coatings (TBCs) applied to the surface of metallic components in the hottest parts of gas turbine engines. These coatings with an adequate cooling system allow to operate in turbines at temperatures as high as 1500 °C or even higher. Their main roles are to reduce the surface temperatures of the underlying superalloy components and protect them from high temperature oxidation and hot corrosion. With the increasing of inlet temperatures (above 1200 °C) for an ever-higher efficiency of the gas turbines, issues such as corrosion by siliceous debris called CMAS (acronym relating to the various oxides constituents: CaO, MgO, Al_2O_3, SiO_2) have become significant. In particular, CMAS debris melt at the operating temperatures of gas turbines and it can infiltrate into the ceramic coating leading to its damage. In this context, this thesis was carried out in order to better understand how the microstructure, material and architecture of TBCs can affect the CMAS corrosion resistance of TBCs. Preliminarily, the influence of microstructure on CMAS corrosion, keeping 8YSZ coating chemical composition as a constant, was studied. Ceramic coatings with three different microstructures were investigated:

1. Porous microstructure obtained by atmospheric plasma spray (APS);
2. dense vertically cracked (DVC) microstructure obtained by atmospheric plasma spray (APS);
3. columnar microstructure deposited by suspension plasma spray (SPS).

Once established the DVC microstructure as the most promising for improved resistance to CMAS corrosion, tests were carried out on advanced materials which can be a valid alternative to 8YSZ. Above 1200 °C, 8YSZ has an insufficient phase stability, thus three novel coating materials with potentially improved durability in contact with molten CMAS: Gd/Yb/Y co-doped ZrO_2, Gd_2ZrO_7 and ZrO_2-55 wt.%Y_2O_3, were tested. Lastly, multi-layered coatings where 8YSZ with either porous or DVC microstructure was employed as a bottom layer under a DVC top layer of either Gd/Yb/Y co-doped ZrO_2, Gd_2ZrO_7 or ZrO_2-55 wt.%Y_2O_3 were also carried out to assess their thermomechanical resistance and the CMAS infiltration behavior.

This thesis is structured as follow:

- In chapter 1, a literature review is given to introduce the state of the art of thermal barrier coatings and the spraying techniques used to obtain these coatings;
- in chapter 2, the materials tested, the thermal spray processes involved and the characterization methods are introduced;
- in chapters 3 and 4, results are discussed based on varying TBC's microstructure; material composition and architecture.

1 Introduction

The chapter includes an overview on operating principle of gas turbines with a focus on blades which are the components to be protected, and on the state of the art of thermal barrier coatings. A detailed description of the deposition processes of TBCs is reported. In addition, degradation mechanisms of TBCs and new advanced ceramic material as alternative candidates to 8YSZ are illustrated.

1.1 Gas turbines engines

The global gas turbine market size was valued at USD 20.38 billion in 2020 and is expected to grow at a compound annual growth rate (CAGR) of 6.8% from 2021 to 2028 [1]. Gas turbines are generally used for aeronautical propulsion and power generation and their main components consist of a compressor; a combustor; a turbine (Figure 1).

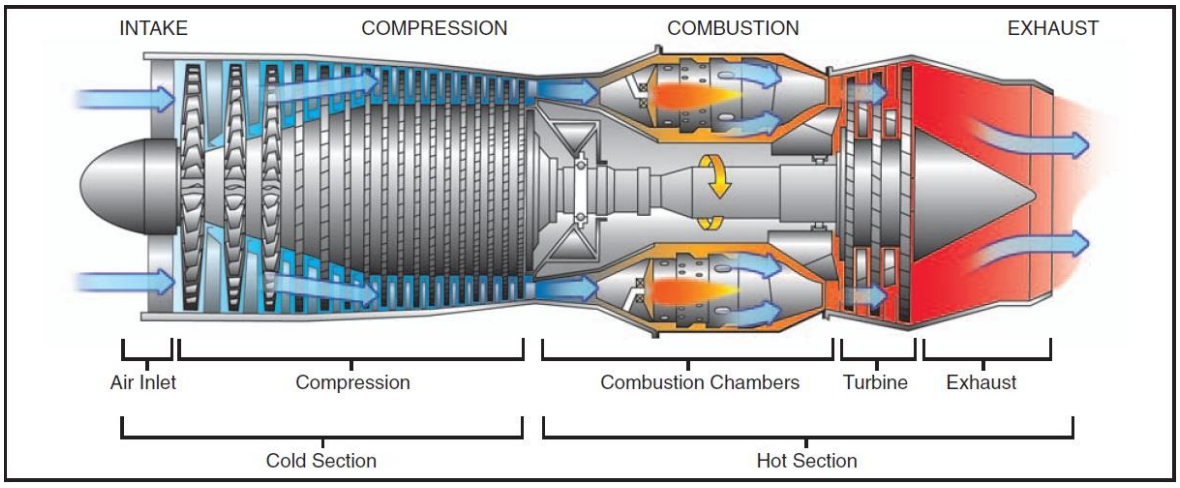

Figure 1 Gas turbine configuration [2]

The ideal Brayton cycle (Figure 2A) describes all the operations of these engines and it consists of the following four processes (Figure 2B) [3]:

1. The air is inlet in the compressor module and it's compressed (adiabatic process, from 1 to 2);
2. The fuel is introduced and the mixture air/fuel is ignited in the combustor chamber (isobaric heating process, from 2 to 3);

3. The hot gases produced expand through the turbine (isentropic process, from 3 to 4). The turbine section consists in a shaft with a series of rotating blades that are driven by high-pressure hot gases. That turbine's shaft continues to rotate and drive the compressor until the whole gas turbine is kept in rotation.
4. The isobaric cooling process (from 4 to 1): the hot air is cooled by atmosphere.

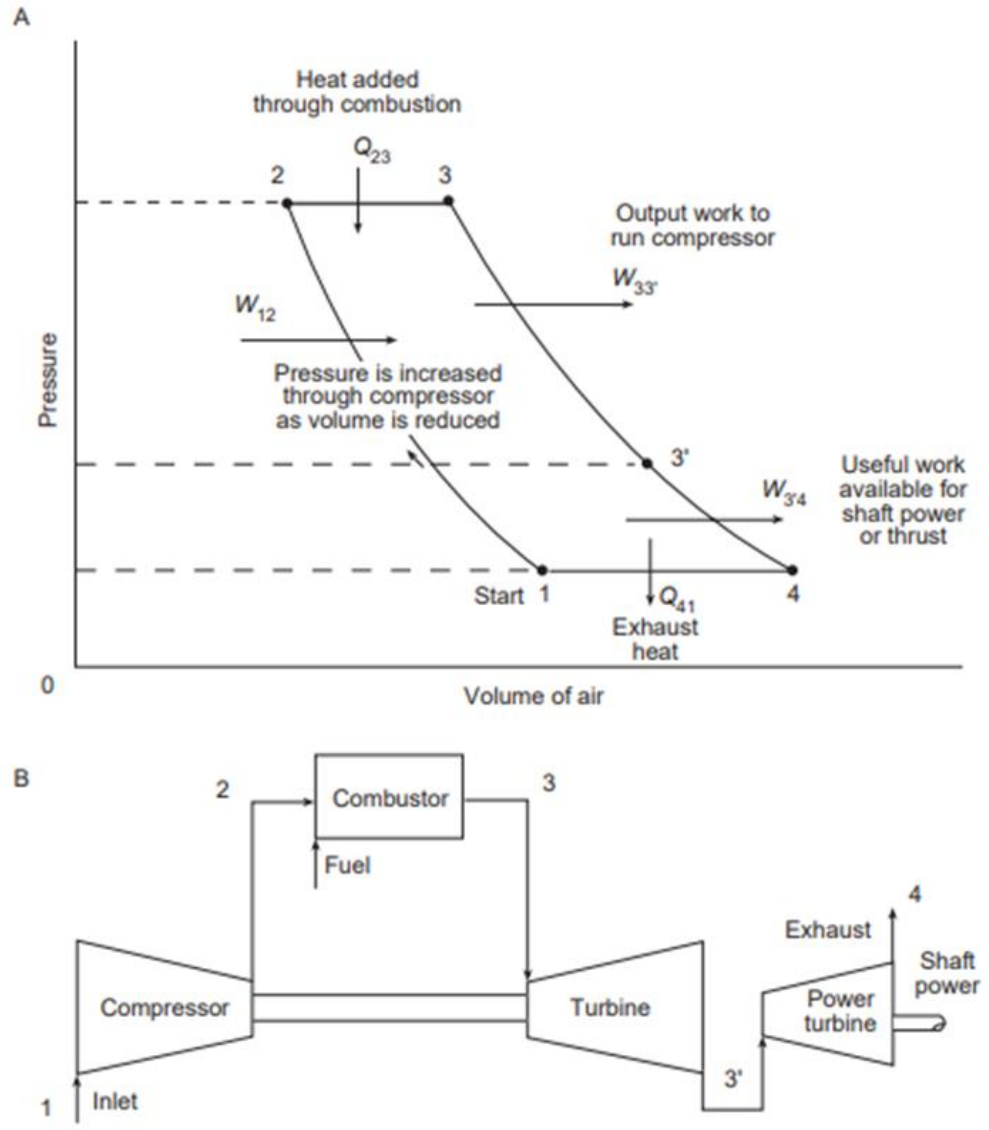

Figure 2 A) Brayton cycle pressure-volume diagram; B) Scheme of a gas turbine showing relative points from Bryton cycle diagram [3]

The ideal Brayton cycle thermal efficiency, η_B is expressed by Eq. 1 [3]:

$$\eta_B = 1 - \frac{T_4}{T_3} = 1 - \frac{1}{r^{\frac{(k-1)}{k}}} \qquad \textit{Eq. 1}$$

where the absolute temperatures T_3 and T_4 correspond to points 3 and 4 in Figure 2, k is the ratio of specific heats for the ideal gas, and r is the compressor pressure ratio.

As shown in the Eq. 1 the overall efficiency of the gas turbine primarily depends on the overall pressure ratio (OPR) of the compressor and secondary on the inlet gas temperature (TIT) [4]. For the proper functioning of the gas turbine, the pressure inlet has to be higher than that at the exit. In order to reach a higher compressor pressure ratio and higher fire temperatures to increase the final performances of gas turbines, many studies were carried out in the last 30 years. From year 1940 to 2010, an increasing of compressor pressure ratio from 7:1 to as high as 45:1 and firing temperatures from 760 to 1482 ºC was obtained and consequently an increase of gas turbine thermal efficiency from about 15% to over 45% was registered [5]. If on one hand the increasing of the inlet gas temperature leads to more efficient engines, on the other hand it can be the cause of the low durability of the blades located in the hottest sections.

1.1.1 Gas turbines blades

Gas turbines blades are subjected to high stresses such as tensile stresses induced by centrifugal forces and bending stresses caused by gas dynamic forces. During gas turbine operations, different failures could occur (Figure 3). Carter summarized the failure modes as follow [6]:

1. **mechanical damage:** the ingestion of large amount of air which may contains extraneous particles can cause damage through either erosion or impact. In aeronautical field, high-strength stainless steel alloys are used to withstand the debris injection, known as *foreign object damage* (FOD). These solid objects can cause nicking and bending, primarily, of the compressor blades, leading to their mechanical degradation. Besides, the debris impact can initiate the fatigue failure because of the continuous rotation of the blades;

2. **high temperature damage:** it develops when foreign objects, after passing through the compressor, reach the hottest sections of the gas turbines attacking the blades. Corrosion by these contaminants, at high temperatures, can be a major problem;
3. **high temperature exposure:** damage mechanisms that occur at high temperatures are creep or fatigue and high temperature corrosion. To overcome these critical issues, the most common material used for turbine blade manufacture are nickel – based super-alloys capable to resist at high temperatures and high stresses;
4. **creep failures:** the environment of a gas turbine is distinguished not only by high temperatures but also by high pressure. These two conditions could lead to the creep of the blades which manifests itself with the stretching and elongation of the blade;
5. **fatigue failures:** normally, turbine blades are designed to avoid *high cycle fatigue* (HCF), being able to endure many stress cycles. The problem mainly occurs when FOD penetrates into the gas turbine. FOD and a very high cycling rate as a consequence of rotation speed and higher blade passing frequencies, leads to the fatigue failure of the blade. The main reason of the low durability of the gas turbine components is the *low cycle fatigue* (LCF) imposed by starting and stopping in operation. The disk/blade combination is subjected to loadings due to self-weight during the engine shutdown while during the operation, at high temperatures, is subjected to loadings from centrifugal forces. The transition between these two stages induces significant thermal stresses;
6. **corrosion failures:** the intake air can also contain sodium and chlorine, or others atmospheric contaminants depending on where the gas turbines are placed. Moreover, they are continuously exposed to a strongly oxidising conditions and to fuel contaminants such as sulphur or vanadium. To reduce the corrosion of the nickel super-alloy, many protective coatings were employed. In particular, metallic coatings based on chromium and aluminium provides protection against oxidation.

Figure 3 Hot corrosion damage of turbine blades [7]

To reduce the surface temperatures and consequently to limit the phenomena cited above, internal cooling systems were designed. Indeed, the high temperatures required (> 1400 °C) for an improving of the thermal efficiency have led to a continuous research for the optimization of cooling techniques. Gas turbine blades are cooled internally and externally to ensure lower surface temperatures and lower temperature gradients during the operation [8]. Temperatures can be even higher than the melting point of metallic components of the gas turbine. In this regard, the combination of innovative cooling schemes and the use of protective refractory-oxide ceramic coatings called thermal barrier coatings (TBCs) becomes essential, making the gas turbine more durable [9].

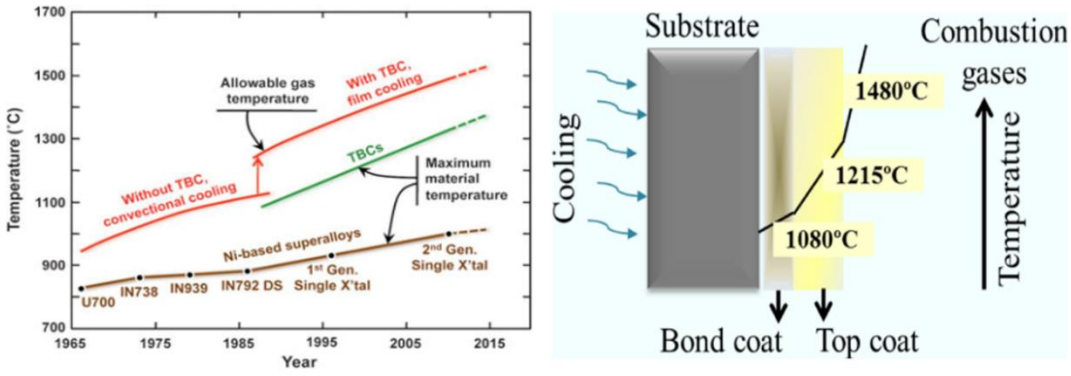

Figure 4 a) progression of the operating temperatures of Ni-based superalloy and thermal barrier coatings; b) variation in the combustion gas temperature by the application of TBCs to a substrate [10]

1.2 TBCs system

Protective coatings for the hot section components of industrial gas turbines consist of at least two deposited layers (metallic bond coating and ceramic top coating), as shown in Figure 5, and an inner layer formed between the two mentioned coatings, if the component and the protective coatings are exposed to a high temperature oxidizing atmosphere:

1. Metallic bond coating
2. Thermally grown oxide (TGO)
3. Ceramic top coating

Each layer has its own function and the whole system contributes to provide protection of the hottest gas turbine components. In this paragraph, the different properties of each layers will be discussed. A preliminary chapter on the properties of the protected superalloy component is included as well.

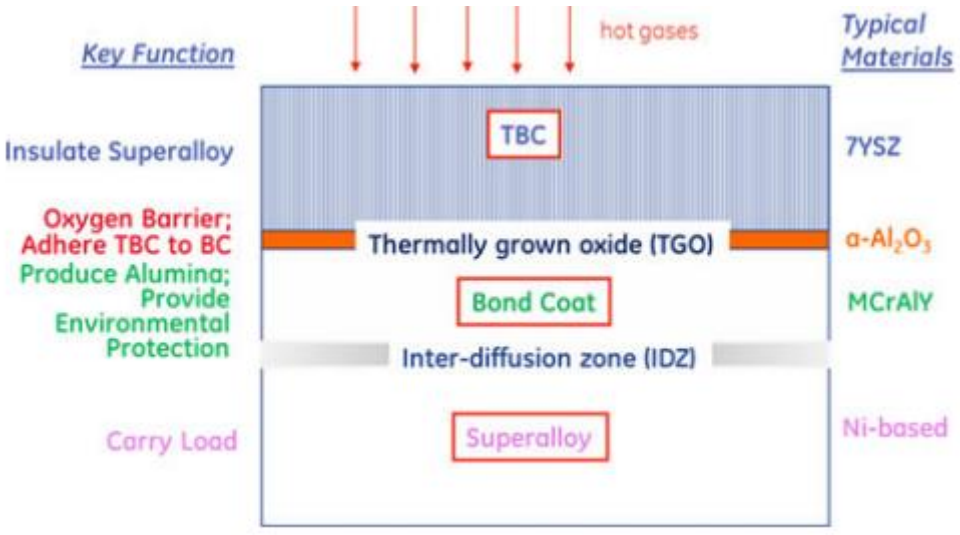

Figure 5 Schematic of TBC system showing each layer, its material and applications [11]

1.2.1 Substrate alloys

As mentioned previously, the material used for the gas turbines' components must satisfy some requirements such as high melting point, strength (tensile strength, creep strength, fatigue strength) ductility and toughness. Figure 6 illustrates the temperature capability of classes of

alloys and shows how Ni and Co based alloys, among all, maintain strength at higher temperatures [12].

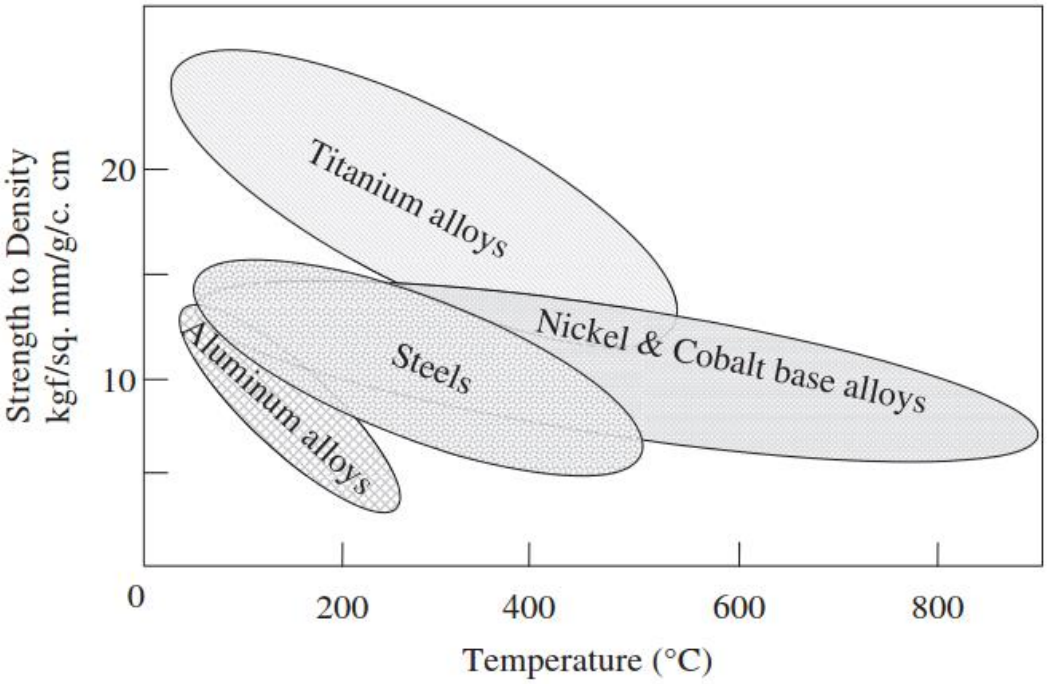

Figure 6 Temperature capability of classes of alloys [12]

Super alloys with Ni and Co, are produced by different strengthening mechanisms [12,13]:

- *Strengthening of the austenitic γ phase by solid solution:* the gamma phase, γ, with a face-centred cubic crystal structure which is the matrix phase of the alloy, contains concentrations of elements such as Co, Cr, Mo, Ru, and Re in Ni based alloys and Ni, Cr, Mo, W, Nb, Ta in Co based alloys. These substituting solute atoms have different size compared to the matrix and can create stress fields that impede dislocation motion. The increase of the strength occurs because of the dislocation movement is slowed down. This mechanism operates both in Ni and Co based superalloys.
- *Coherent fcc γ and bct γ' precipitates (Figure 7):* the gamma prime precipitate, denoted γ', are precipitates of the ordered intermetallic compound of composition Ni_3Al which is coherent with the γ-matrix. This is the primary mechanism for strengthening the Ni based superalloys. In addition, strengthening can be provided by carbide precipitates.

- *Precipitation of Carbides*: MC carbides due to the combination of Carbon, often present at concentrations up to 0.2 wt.%, and reactive elements such as titanium, tantalum and hafnium [13]. During processing or service, these can decompose to other species, such as $M_{23}C_6$ and M_6C, which prefer to reside on the γ-grain boundaries. Carbides within grains impede dislocation motion, increasing the strength, and carbides located at grain boundaries reduce grain boundary sliding.

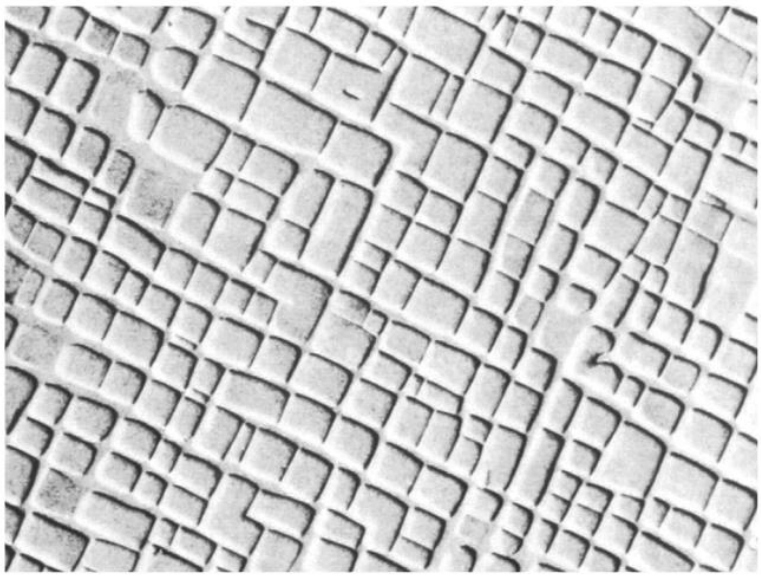

Figure 7 SEM micrograph of Gamma prime precipitates in a gamma matrix [12]

1.2.2 Bond coat and thermally grown oxide

Metallic coatings provide protection against oxidation and corrosion of the Ni-based super alloy turbine components. Depending on the elemental constituents of the coatings, it's possible to obtain different benefits. The Figure 8 reports the function and the effects of the elemental constituents of the metallic coatings. The bond coat is often made of MCrAlY alloys, where M is often referred to Ni, Co or a combination of both. Other types of bond coat, such as NiAl and PtAl bond coat can be deposited with diffusion aluminizing or chemical-vapor deposition in conjunction with electroplating. NiCoCrAlY bond coat consists of two phases mixture of the β-NiAl phase and the solid-solution of γ-Ni. The latter, can increase the ductility and thermal fatigue strength, while the Al of the β-NiAl phase is essential to form an adherent α-Al_2O_3-based oxide scale (*thermally grown oxide, TGO*) during the exposure to high temperatures [13].

The oxide growth is driven by two diffusion mechanisms: inward diffusion of oxygen along grain boundaries and outward diffusion of aluminium along the already formed alumina particles towards the top coat - TGO interface. Alumina is the most stable oxide and has a lower formation energy than the other elements present within the bond coat. During a prolonged exposure at high temperatures, alumina grows and becomes a continuous and dense layer which initially acts as a protective layer, but exceeded a certain thickness threshold, it starts to crack or spalls off. This is mainly due to thermo-mechanical stresses generated by the mismatch in coefficients thermal expansion (CTEs) between the different layers in TBCs. Both phenomena of cracking within alumina layer and depletion of aluminium content in the bond coat, lead to the formation of mixed metal oxides (CSN) which can cause the rapid failure of the TBC system [14].

Elemental Constituent	Beneficial Aspects	Detrimental Aspects
Ni	Major constituent of substrate alloy. Provides strength.	Prone to destructive interaction with sulfur.
Co	Major constituent of substrate alloy. Provides microstructural stability and strength.	Prone to destructive interaction with sulfur.
Al	Constituent of substrate alloy. Major contributor to providing strength. Contributes to oxidation resistance.	Large concentration lowers melting point.
Cr	Constituent of substrate alloy. Contributes to oxidation resistance to 1500°F (816°C). Reduces Al requirement for formation of alumina scale. Imparts resistance to hot corrosion.	Lowers creep strength.
Ta	Enhances hot corrosion and oxidation resistance. Improves strength.	
Si	Enhances oxidation and type II hot corrosion resistance.	Large concentration leads to formation of brittle phases.
Hf, Y, Y_2O_3, oxides of other reactive elements	Improves adherence of alumina and chromia scales.	Large amounts are detrimental.
Pt	Improves oxidation and hot corrosion resistance.	

Figure 8 Function and effects of the elemental constituents of the metallic coatings used as bond coat [12]

1.2.3 Ceramic top coat

The main function of a ceramic top coat is to provide thermal insulation to the underlying metallic substrate. In this regard, this layer has to satisfy certain requirement: 1) low thermal conductivity, (2) high melting point and (3) phase stability. The material that meets these requirements is zirconia due to its low thermal conductivity, relatively high CTE and adequate toughness [10]. Zirconia has a monoclinic crystal structure at room temperature and undergoes phase transformations to tetragonal (at 1197 °C) and cubic (at 2300 °C) at increasing temperatures with a melting point of about 2700 °C [14].

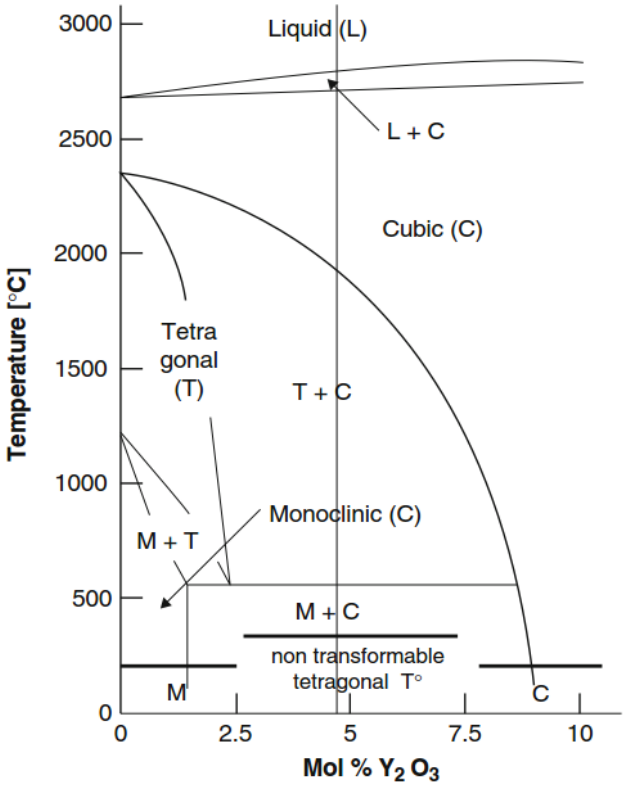

Figure 9 Phase diagram of zirconia –yttria system [12]

However, the state of the art of TBCs is zirconia stabilized with yttria (Y_2O_3), generally called YSZ. The optimum yttria stabilizer content is around 7 wt.% and it was determinated by high temperature rig test (Figure 10) at the National Aeronautics and Space Administration (NASA) [12]. By inserting the ~ 7% by weight of yttria within zirconia, it's possible to form a metastable 'non-transformable' tetragonal t' phase when the ceramic is quenched. In this way, the

martensitic transformation from tetragonal to monoclinic zirconia that occurs after cooling is avoided. The tetragonal-monoclinic transition is accompanied by 4% volume change which can lead to the delamination of the TBC. For a content of yttrium higher than 10 wt.%, the low-temperature phase is cubic (C). The cubic phase is also a non-desired phase because it has a lower fracture toughness (~ 1 MPa·√m) compared with t' phase [15]. However, several studies show that a further method to reduce the thermal conductivity is increasing the yttria content in zirconia (Figure 11) [16].

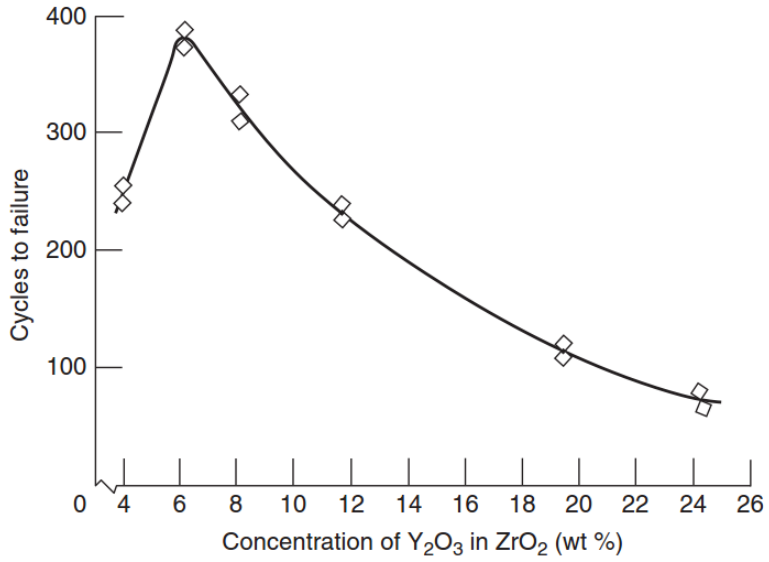

Figure 10 TBCs composition selection based on durability [12]

The choice, for these types of applications, falls on YSZ mainly because it has a low thermal conductivity at elevated temperature [2.3 W/mK at 1000 °C for a fully dense material] [17]. The low value of thermal conductivity is due to its high concentration of point defects (oxygen vacancies and substitutional solute atoms), which scatter heat-conducting phonons (lattice waves). A further strategy to reduce the thermal conductivity is by introducing porosity within the coatings. An effective reduction of the thermal conductivity, in the range of 0.86 -1 W/mK was measured for porous coatings obtained by atmospheric plasma spraying deposition (APS) [18] deposition process, that will be illustrated in section 1.3.

Moreover, another fundamental property of YSZ is the high thermal expansion coefficient (CTE) (11×10^{-6} K^{-1} at 293-1273 K) compatible to that of the underlying metal bond coating

(13-15 × 10^{-6} K^{-1} at 293-1273 K) [19,20]. The similar CTE allows to alleviate stresses generated by the thermal mismatch. As mentioned, YSZ has so many advantages (e.g. low thermal conductivity, good CTE matching with the bond coating and high fracture toughness) but at temperatures above 1200 °C, it shows insufficient phase stability. Above 1200 °C, the transformation of YSZ from t' phase to the equilibrium tetragonal and cubic (t and c) phases is accelerated [21]. The disintegration of the coating can rapidly occur because the tetragonal phase transforms to the monoclinic (m) phase [21]. In this context, many studies were carried out in order to identify new classes of materials which could be valid alternative to the YSZ (Paragraph 1.5).

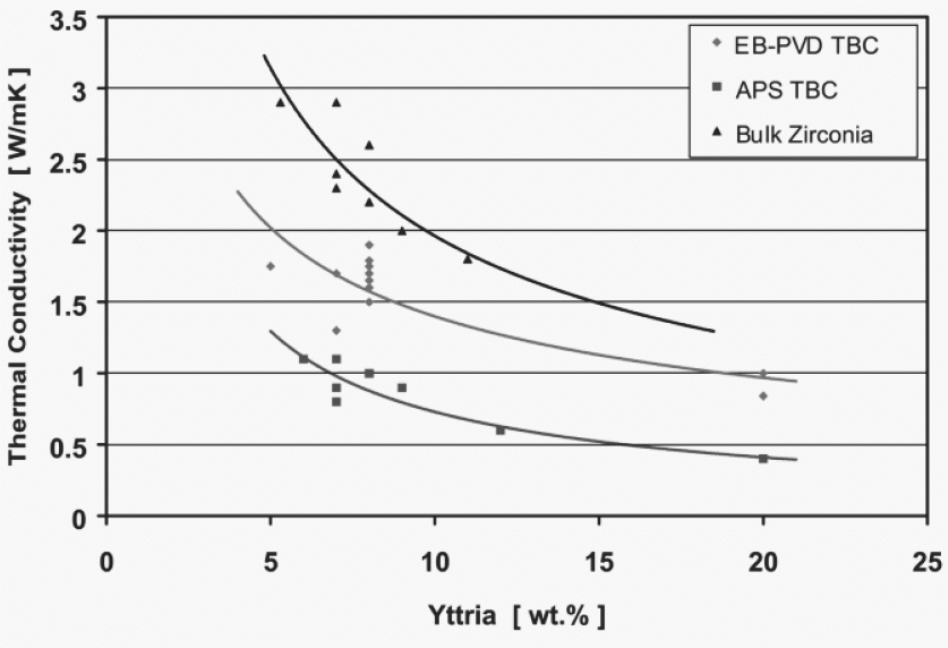

Figure 11 Thermal conductivities of zirconia bulk and zirconia TBCs as a function of the yttria content [16].

1.3 Deposition processes of ceramic Top Coats

1.3.1 Electron Beam-Physical Vapour deposition (EB-PVD)

In the Electron Beam-Physical Vapour deposition (EB-PVD), an electron beam is formed by heating a conductive filament at temperatures higher than 2000 °C. Electrons are accelerated by means of an electric field and focused by electromagnetic lenses on the coating materials ingots in a crucible kept in a vacuum environment. The kinetic energy of the incoming electrons is transformed into heat impacting on the ingots, melting and evaporating them. The evaporated material deposits on the surface of substrates [22]. The EB-PVD equipment is more complex and expensive compared to atmospheric plasma spraying (APS) or suspension plasma spraying equipment (Figure 12).

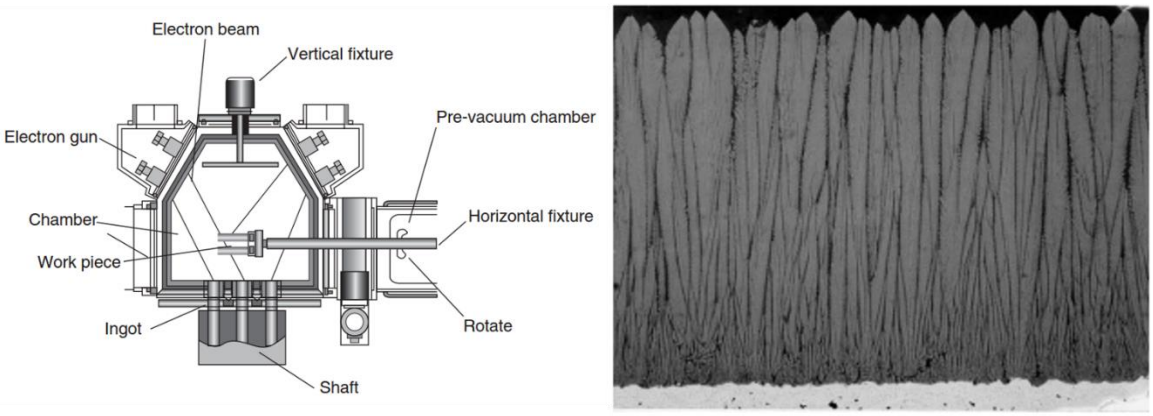

Figure 12 a) schematic representation of EB-PVD system [22]; b) columnar microstructure of TBC deposited by EB-PVD [16]

The deposited coating is characterized by a columnar microstructure. Single crystalline columns of fine diameter (< 2-3 µm) start to grow on the substrate, achieving a diameter at the coating tip up to 10-20 µm. The columns are interconnected via inter-columnar gaps that can be large from few nanometres to 1 µm [23]. Open porosity originates from the voids present between nano-sized secondary columns, so called feather-arms, growing at the column edges [24]. These features gaps are generated from vapour phase condensation and macroscopic shadowing caused by the curved columns tips, due the rotation of part during deposition [25]. Closed porosity is created within the primary columns in form of finer elongated channel-like

pores (i.e. intra-columnar porosity) as a consequence of the interruption of the vapour deposition during rotation [23].

The presence of these columns imparts strain tolerance to the TBC system, when it is subjected to thermal stresses [25]. The type and distribuition of pores within the coating is also important for determinating the thermal conductivity of the coating.

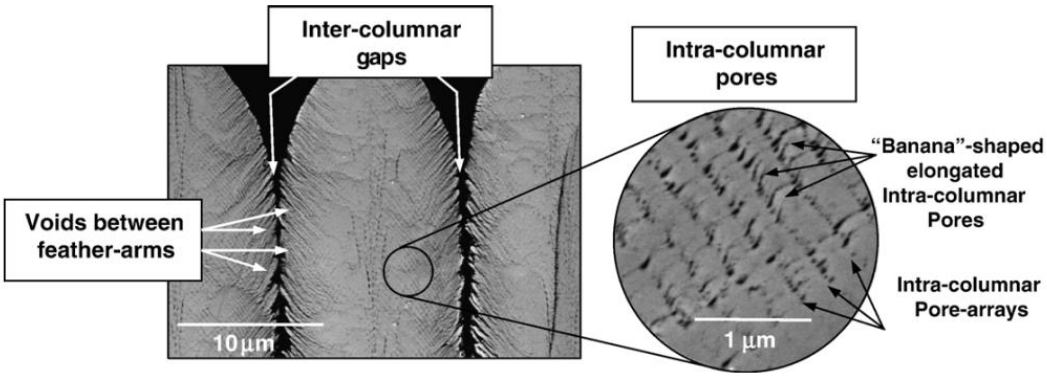

Figure 13 Type and distribution of the pores in TBCs obtained by EB-PVD [23]

1.3.2 Atmospheric plasma spraying (APS)

When plasma spray process operates in ambient atmospheres is called atmospheric (or air) plasma spraying (APS) processes [12]. The plasma jet is produced using plasma torches, consisting of a cathode and an anode which are settled along a common axis. A schematic configuration of a plasma torch is reported in Figure 14.

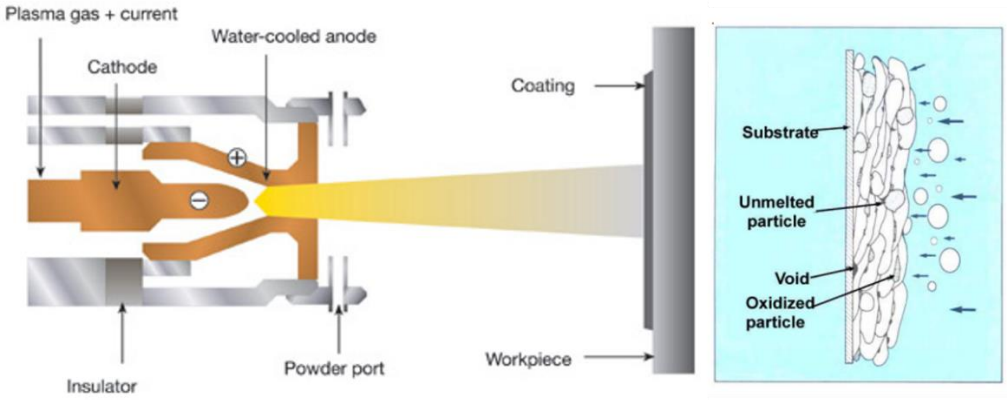

Figure 14 Schematic configuration of APS process and final microstructure obtained [26]

The raw materials in the form of powder are radial/axial injected into the plasma jet which is generated by a plasma gun. The plasma torches work with Ar, Ar-H_2, Ar-He, Ar-He-H_2, N_2 and N_2-H_2 mixtures. The temperatures of the plasma are above 8000 K and up to 14000 K, and particles velocities between 500 and 2800 m/s at the nozzle exit [26]. The particles acquire thermal energy and momentum from the plasma and they undergo melting, followed by impact and rapid solidification. The deposited coating is the result of an assemblage of a lamellar structure consisting of "splats", cracks, pores and unmelted particles [25]. APS deposition process is optimal to deposit the ceramic top coating of TBCs, while it is used to deposit MCrAlY bond coating when production costs are a major driving force, since metallic coatings deposited by APS contains many oxides. The powders' particles size is typically between 10 and 100 μm. Larger and denser particles tend not to melt completely, while finer particles don't penetrate in the plasma and tend to cross the colder periphery, resulting in not-adequate heating in flight. Particles size around 40 μm is preferred (i.e. a size distribution peaked at 40 micron), for example, when agglomerated and sintered feedstock are used. The morphology of the powders affects good flow ability and melting during the process. The most common manufacturing routes of ceramic top coating powder feedstock are: fused and crushed; agglomerated and spherodized; and agglomerated and sintered (Figure 15) [27].

- The fused and crushed powders are obtained by fusing the raw oxides in a furnace followed by a crushing step. After heating and cooling, the formed blocks are crushed in ball mills to reduce the size of agglomerated by impact. Particles obtained are angular and blocky and sometimes, the particle size distribution is excessively fine for the thermal spray process (below 5 μm) [28].
- A technique based on a plasma fusion method is employed for manufacturing Hollow - oxide Spherical Powders (HOSP) [29]. The HOSP process involves the spray drying (agglomeration) process. With the latter, it's possible to obtain porous particles. The production of these powders includes the following stages: 1) heating of the spray dried particles by a hot plasma environment order to melt the outer layers of material. During this stage, the gas contained in the pores of particles expands and partially leaves the material in the filtration regime; 2) retaining of the gas in the particle as the particle further melts, and the formation of an internal gas cavity and a liquid spherical shell; 3) quenching of obtained hollow droplets, resulting in the formation of hollow microspheres. The advantage

of using these particles morphologies consists in a more uniform melting behaviour during the spray process.

- The most versatile and used manufacturing process is agglomeration and sintering [30]. For the production of agglomerated and sintered powders the following steps are employed: 1) powder agglomeration by spray drying process [31]. Particles are dispersed in a suspension (often water based), called slurry. This slurry is pumped through a nozzle to aerate and create a spray of the slurry. The droplets, exposed to a flowing stream of hot source (air or inert gas like nitrogen), rapidly dry in flight before their impact onto the drying chamber walls; 2) After agglomeration, the solid dried particles are consolidated by liquid state sintering or by solid state sintering [32].

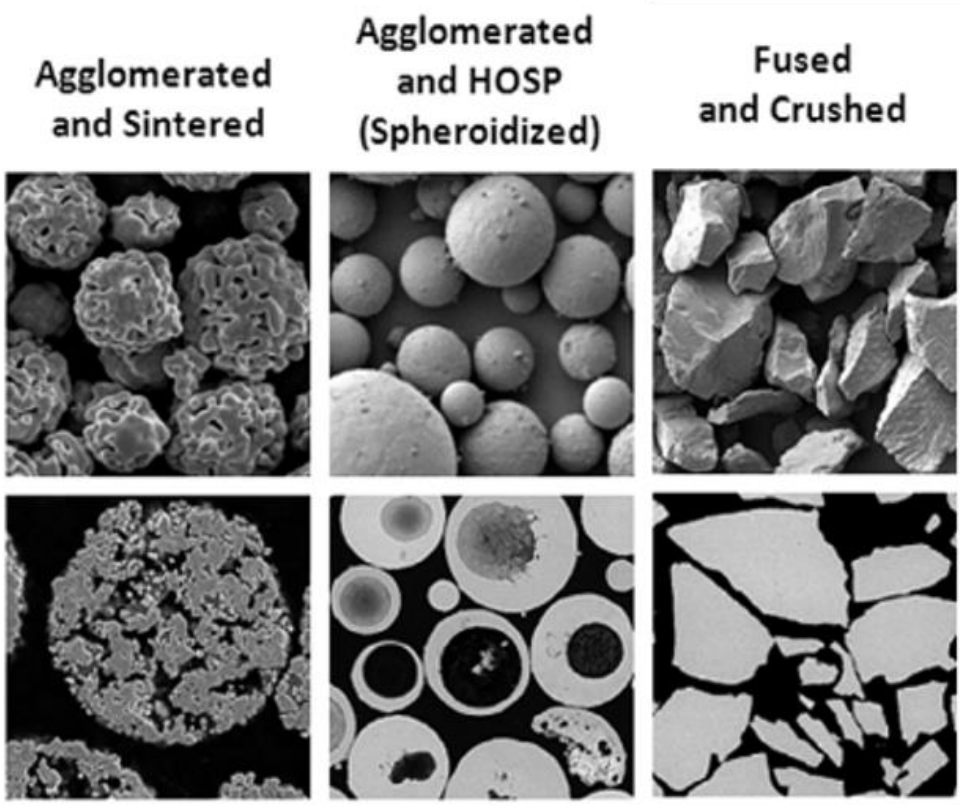

Figure 15 Three types of powder morphologies widely used in thermal spray process [28]

Important parameters are also the angle of spray that is usually kept between 75 and 90 degrees and the distance between the nozzle and the substrate to obtain high quality coatings. The lamellae transformation process, that happens when particles hit the substrate, is the basis of

coating build up and involves two major processes: deformation and solidification. It is influenced by:

- particles velocity, size and phase content;
- particle material proprieties in liquid state;
- ability of wetting the substrate by liquid particles;
- temperature of the substrate;
- substrate roughness.

All these parameters strongly affect coating adhesion/cohesion and microstructure [33].
Two morphologies can be observed for splats: pancake and flower. Pancake splats are formed at the impact of particles with low thermal and/or kinetic energy, while flower splats are associated with high-energy impact [28]. The temperature parameter at impact is of fundamental importance for coating's adhesion, along with surface roughness. The mechanical anchorage of the first splats hitting the substrate, is the most common adhesion mechanism: once the particles splatted on the substrate irregularities, during their solidification they get attached because of liquid shrinkage, as shown in Figure 16.

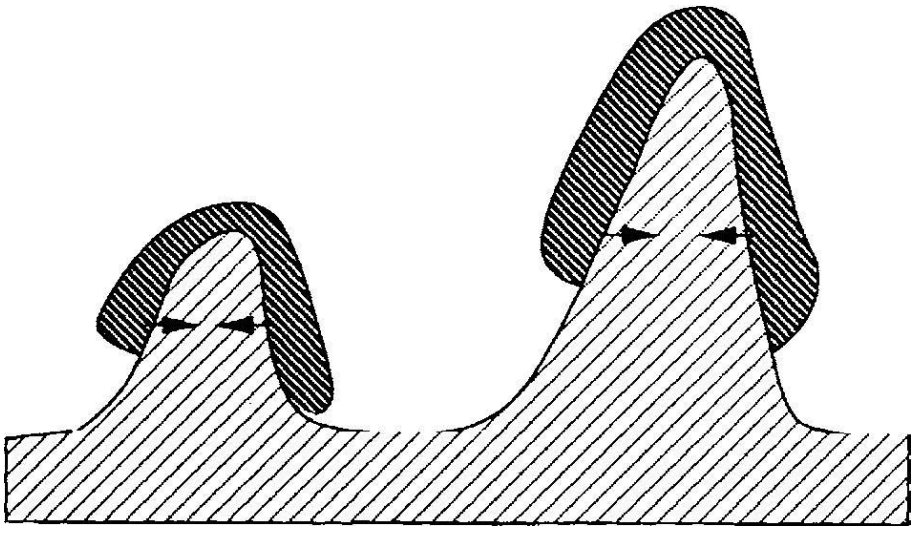

Figure 16 Mechanical anchorage of splats to irregularities of the substrate surface [33]

In TBCs, when particles of zirconia are deposited onto the metallic bond coating, two sources of stresses occur: 1) contraction of the particles because of the quenching from the molten state

to solid splats at substrate temperature and 2) stress due to the differential thermal contraction of zirconia relative to the underlying substrate.

Varying processes parameters, it's possible to obtain different microstructures (Figure 17): 1) conventional porous microstructure and 2) highly dense microstructure with periodically spaced segmentation cracks perpendicular to the substrate/coating interface, generally called Dense Vertically Cracked (DVC) microstructure [18,34].

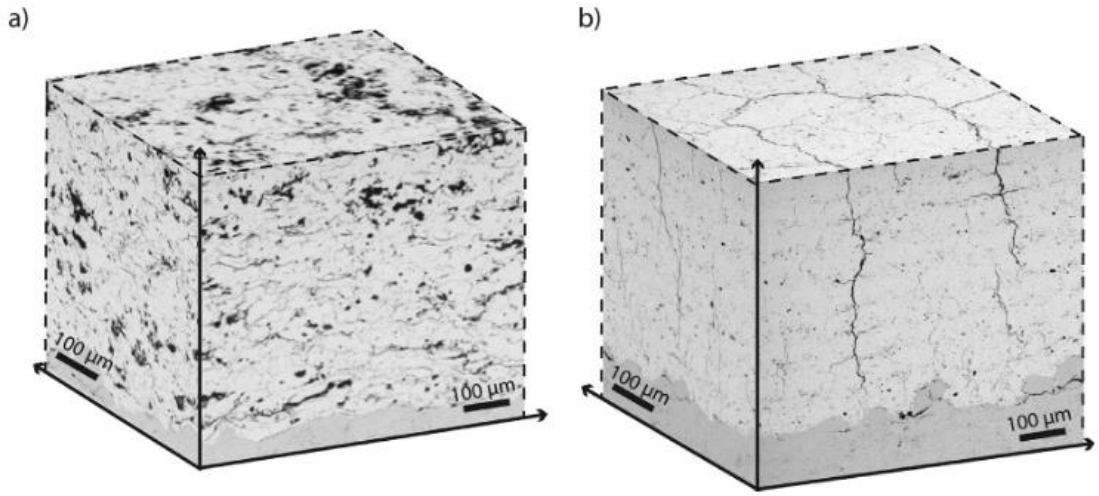

Figure 17 a) Porous APS microstructure; b) dense vertically cracked microstructure [18]

DVC coatings are characterized by macrocracks perpendicular to the bond coating/top coating interface through the whole coating thickness. The process of obtaining these type of microstructures was studied by Taylor [34]. Chen et al. reported that the driving force for the vertical cracks formation is in-plane tensile stresses which can be generated by: 1) the thermal expansion mismatch between ceramic top coat and metallic bond coating/substrate and 2) the rapid cooling of the molten droplets impacted on the substrate [35]. As already mentioned, the thermal expansion coefficient of the metallic bond coating/substrate is larger than that of 8YSZ coating, resulting in in-plane tensile stresses at the interface. As well, during the successive passes of the plasma torch, molten droplets solidify quickly on the substrate generating in-plane tensile stresses. This mechanism is favourite using a set of deposition parameters able to produce a high-enthalpy plasma. In this way, it's possible to obtain higher deposition temperatures, higher coatings densities and higher particle temperatures that result in higher

tensile stresses. These stresses promote the formation of the vertical cracks. DVC coatings were designed to impart greater thermocyclic durability to the TBC. The enhancement of in-plane strain tolerance and the high fracture toughness allow to withstand at larger thermal stress without failure [27].

Moreover, DVC coatings result to be more resistant to sintering during the thermal exposure because the areas between the macro-cracks are already dense [18,36,37]. The DVC 8YSZ has a thermal conductivity value of 1.31-1.50 W/mK, while that of the porous 8YSZ is in the range from 0.66W/mK to 0.93W/mK over the temperature range of 200-1200 °C [35].

1.3.3 Suspension plasma spraying (SPS)

One limitation of atmospheric plasma spray process is the inability to obtain thin (less than 10 μm) and nanostructured coatings with microstructure features 1-100 nm in size, because of the inability to use feed powders finer than 5 - 10 μm [12]. To overcome this problem, one possible key is to spray the coating material using a liquid carrier instead of gas by different techniques [38]. One technique consists of using a precursor solution of the material injected and it is called Solution Precursor Plasma Spraying (SPPS). The other technique consists of dispersing nanometric and submicrometric particles in a suspension where the solvent is ethanol, water, etc. This process is called Suspension Plasma Spraying (SPS) [12,39,40]. A schematic representation of SPS technique is reported in Figure 18. In the latter process, very fine particles suspended in a liquid phase become large droplets which have enough mass and momentum for penetrating into the hot regions of plasma jet. SPS process is more complex than APS one. Indeed, an important issue is the solid content in suspension which affect the viscosity of the liquid feedstock and consequently the droplet formation on the plasma jet. Moreover, the amount of the solid particles in suspension droplets has a strong influence on the porosity and morphology of the final coating. The choice of the solvent (distillate water, ethanol, methanol, etc…) depends on the surface tension and vaporization of the liquid phase in plasma jet [40]. The solid phase has to be homogenously distributed in the solvent, trying to avoid sedimentation and agglomeration of the fine powder particles. In this regard, dispersant agents are added to suspension. Moreover, for spraying a stable suspension is required. A suspension is stable when the zeta potential is more than + 30 mV or is less than - 30 mV [40].

Ganvir et al. pointed out the steps involved in the SPS process [41]:

- Injection of the suspension;
- Atomization of the suspension;
- Evaporation of solvent from the suspension droplets;
- Agglomeration;
- Melting of the solute particles;
- Deposition on the substrate.

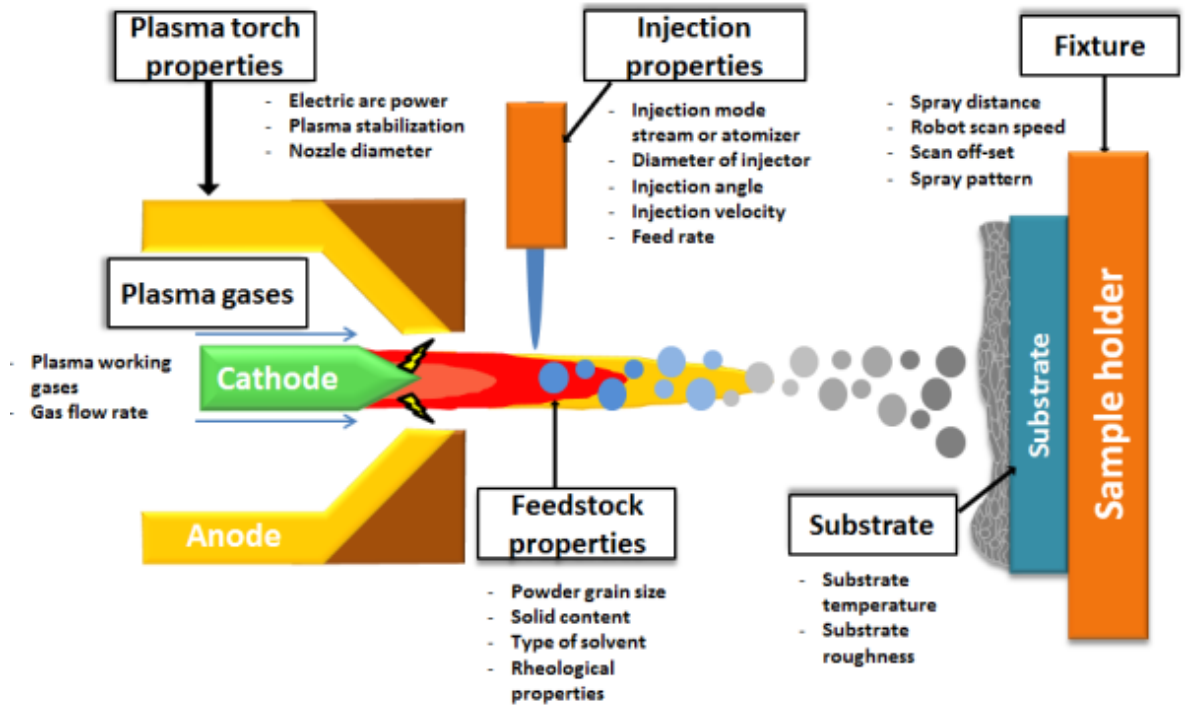

Figure 18 Illustrative description of suspension plasma spray process [42]

The potential of this technique is the possibility to obtain coating with a columnar microstructure analogous to that of EB-PVD coatings at a lower cost [43].

Splats have smaller size (diameters from 0.2-6 μm and a thickness of 20-300 nm) compared to typical APS splats having thicknesses of about 2-5 μm. These types of coatings often exhibit a columnar structure with high inter-columnar gap density and intra-columnar fine porosity (Figure 19). In this case, too, different microstructures (porous, columnar and DVC) can be

achieved. In addition to the type of solvent or particles sizes, injection mode and the roughness of the substrate can play an important role [42].

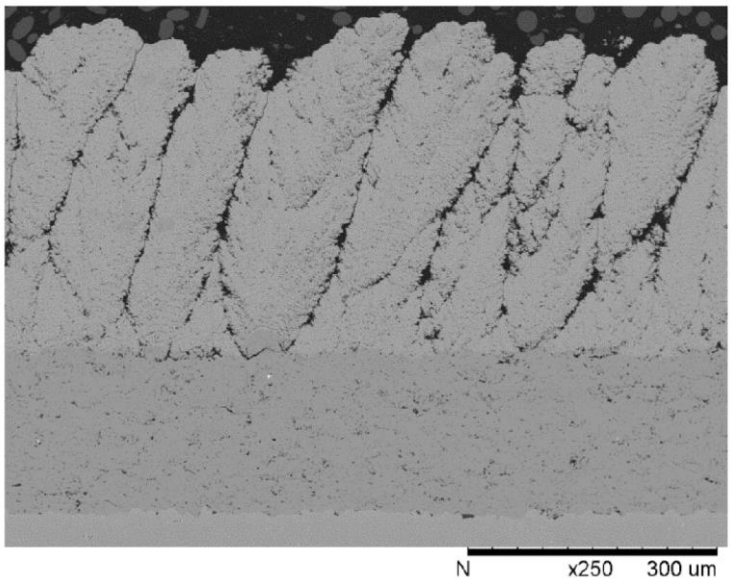

Figure 19 Columnar-like microstructure obtained by SPS process [44]

As already mentioned, thermal conductivity of YSZ coating strongly depends on the microstructures. The thermal conductivity of SPS coatings (columnar microstructure) is in the range of 0.3-1.6 W/mK, while that of EB-PVD and APS coatings is 1.5-2.0 W/mK and 0.8-1.7 W/mK, respectively [9,45]. The low value of thermal conductivity which characterizes SPS coatings is due to the presence of a large amount of sub-micron pores, which are even difficult to quantify by HR-SEM images.

1.3.4 Plasma spray - physical vapour deposition (PS-PVD)

The PS-PVD is a novel thermal spray technique based on conventional methods of TBC deposition by low pressure plasma spraying. The pressure within the working chamber is between 50 and 200 Pa. The low pressure allows to achieve a plasma plume length over 2 m and a diameter of 200-400 mm [46]. The PS-PVD technology is a hybrid method. It is a cost-effective plasma-spraying technique, enabling the evaporation of the coating material. Powders are injected into a plasma plume and then heated until their melting. The high temperature and the high plasma stream velocity (above 2000 m/s) allows the easily evaporation of the feedstock

powders [47]. Besides, a hot and supersonic gas stream permits to coat components with complex geometry. To ensure the evaporation of the injected powders, PS-PVD requires the use of powders with a particles size below 25 µm [48]. Also in this case, it's possible to obtain both splat-like structure and columnar microstructure (Figure 20). The latter can be produced setting a low powder feeding rate, large spray distance and suitable gases. Moreover, to facilitate the formation of a columnar microstructure, it's necessary a pre-heated substrate at a temperature in the range from 900 to 1100 °C [46].

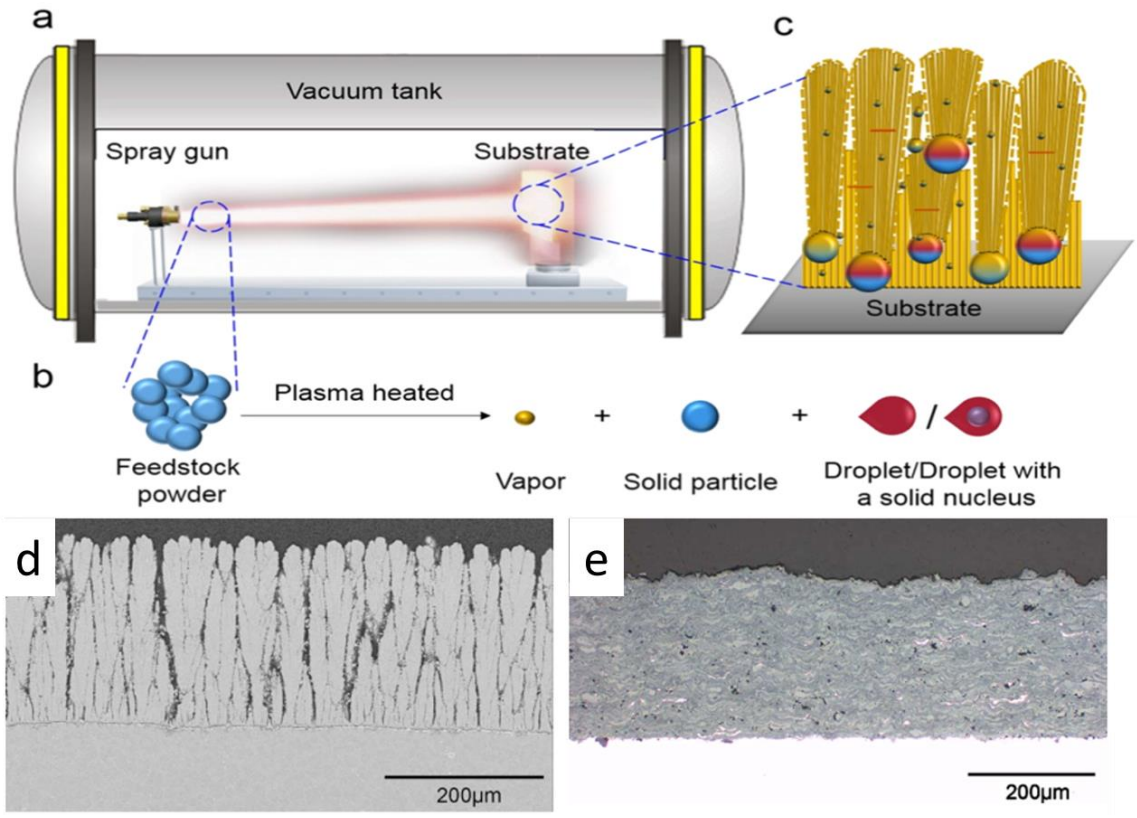

Figure 20 Schematic representation of PS-PVD process; Columnar and splat-like microstructure obtained by PS-PVD [48]

As pointed out by Mauer et al. the coating microstructure depends on the nature of the particles that impact on the substrate [49]. In the case of PS-PVD spraying technique, the deposits are formed predominantly from clusters and/or vaporized atomic species. The coating growth is a consequence of the following mechanisms [49]:

- Shadowing. This phenomenon occurs when the deposits are clusters and it consists of the interaction between the roughness of the growing surface and the angular directions of the impacting particles. After the adhesion of the clusters, the surface becomes rough and the shadowing phenomenon intensifies as the coating grows. The final microstructure consists of columns with domed tops separated by voids (Figure 20d) The internal structures of the columns look feather-like consisting of fine fibers.
- Adsorption, nucleation, and growth. It occurs when the deposit is mainly made up vaporized atomic species. These are adsorbed and initial nuclei are formed on the substrate surface. The coating may grow either in layers or more island-like. The further growth is determined by surface diffusion. Phenomena of surface diffusion and shadowing can be overlapped, leading to the formation of coarse columns. Here, the voids between the columns begin to fill and the column tips become faceted as surface recrystallization begins.

1.4 Thermal barrier coatings degradation modes

As already mentioned in Section 1.1, there are several failure modes by which blades and thermal barrier coatings degrade during their use. Specifically, in this paragraph, TBCs degradation modes are discussed.

1.4.1 Erosion damage

A possible failure mode of TBCs, widely studied in literature, is the damage by erosive phenomena. The repeated impact of solid particles on the ceramic top coats can cause its structural damage. When protective coatings are eroded away, the metallic substrate is directly exposed to high temperature, accelerating its oxidation and other degradation processes. The chemical nature of the abrasive particles depends on the environment in which the turbine is located. The effects of the erosion on the TBCs depends on the coatings' microstructure, porous or columnar; the hardness, velocity and flux of particles; particles size and the angle of impingement. In this regard, it was found that particles smaller than 10 μm don't possess a sufficient kinetic energy to erode blades [50] and that maximum erosion occurs in ceramic coatings when the eroding particles impinges at 90° [12].

Several studies have reported erosion behavior of atmospheric plasma sprayed coatings and electron-beam physical vapour deposited coatings [51]. Nichols et al. studied the different erosion mechanisms that occur in microstructures obtained by these two techniques. He demonstrated that EB-PVD coatings with a columnar microstructure, are more resistant to erosion than porous APS coatings [52]. The two different erosion mechanisms are illustrated in Figure 21.

Erosion of APS ceramic involves relatively low energy to fracture the boundary splat. Thus, with a small amount of eroding particles, a large amount of ceramic material is removed. On the contrary, EB-PVD coatings have strong columns with weak vertical column boundaries. New cracks have to be created within the columns at the expense of large energy.

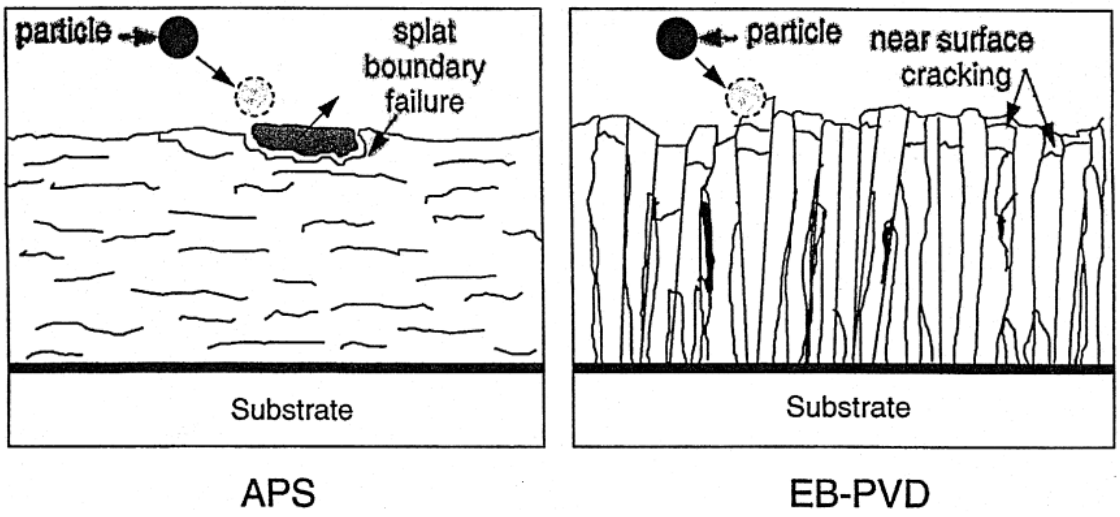

Figure 21 Schematic illustration of the erosion modes of an APS and EB-PVD TBC [52]

In detail, for APS coatings, different types of solid particles erosion were observed [53]:

- Primary scars on the erosion surface (low erosion rate).
- Cracks around the impact area on the coating surface due to repeated impacts (moderate erosion rate).
- Tunnel formation on the surface. The kinetic energy transferred from particles to the ceramic top coat is high enough to connect pre-existing pores (high erosion rate).

While, for EB-PVD coatings, Wellman and Nicholls described three possible modes [54]:

- Near surface cracking: small particles impact on surface with low speed and cracks start to propagate within 20 μm of the columns. Cracks paralleled to the surface are caused by tensile stresses promoted by the elastic waves propagating along each single column.
- Compaction damage: many impacts of particles with a higher momentum (speed or mass) lead to a densification of the first 20 μm of TBCs caused by a plastic deformation. In this case cracks can initiate due to the stress concentration induced by consecutive impacts.
- Foreign object damage: when particles possess high momentum (high speed), most of kinetic energy is absorbed by plastic deformation and densification bending.

1.4.2 Thermocyclically induced degradation

This is the predominant nature of failure mode controlling TBC life. It involves simultaneous imposition of cyclic thermal and mechanical strains (or stresses). Levi et al. explained that the driving force for thermomechanical failure is mainly based on the release of the elastic strain energy stored in the coating [55]. The source of this elastic energy is the thermal expansion mismatch between the TBC and the metallic substrate.

Tensile stresses induced by an isothermal cooling of the coating relative to the substrate, strongly depend on the coating CTE, while the cooling of the substrate generates stress due to the thermal expansion mismatch (Eq. 2) [55]:

$$\sigma\,(y) = \frac{E_c}{1-\upsilon_c}\,(-\Delta\alpha_C \Delta T_{sub} + \left(\frac{y}{h_C}\right)\alpha_C \Delta T_{\frac{sur}{sub}}) \qquad \textit{Eq. 2}$$

where y is the through-thickness coordinate measured from the interface; E_c is the Young's modulus; υ_c is the Poisson's ratio; α_c is the coefficient of thermal expansion and h_c is the thickness of the coating.

The elastic energy per area (U) in the coating, associated to this stress was reported by Levi and followed the (Eq. 3):

$$\mathrm{U} = \frac{E_c h_C (1+\upsilon_c)}{2(1-\upsilon_c)}\left\{(\Delta\alpha_C \Delta T_{sub})^2 - (\Delta\alpha_C \Delta T_{sub})\left(\alpha_C \Delta T_{\frac{sur}{sub}}\right) + \frac{1}{3}\left(\alpha_C \Delta T_{\frac{sur}{sub}}\right)^2\right\} \qquad \textit{Eq. 3}$$

Delamination of the coating occurs when the elastic energy reaches the value of the critical energy release rate [56].

Viswanathan et al. conducted thermal cycling tests on multilayer TBC systems, identifying a general trend of the TCF response, based on elastic energy formulation [56]. He found a correspondence between failure location of the coatings and the energy calculated at the failure location (U_{fail}). Low values of U_{fail} are associated to a premature cohesive failure (failure within

the coating) (Figure 22a), while high values of U_{fail} correspond to a tardive adhesive failure (failure at the interface TGO-TBC) (Figure 22e).

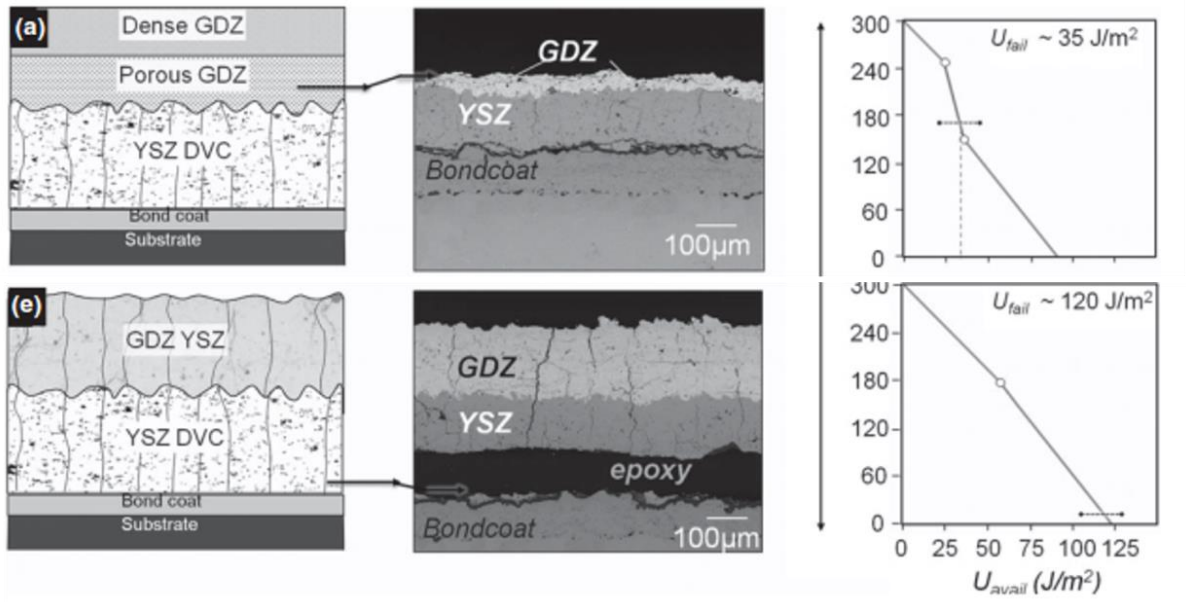

Figure 22 a) premature cohesive failure; e) tardive adhesive failure [56]

An increasing of TCF durability was noted, moving the failure location from within the coating (cohesive) to the interface (adhesive) [56]. This phenomenon corresponds to an increasing of U_{fail} for more durable coatings. Moreover, another important parameter to take in account, is the toughness of the coating. The higher is the toughness of the coating at failure location, the greater is the durability. In general, it was noted that dense coatings have a higher toughness than porous one [57].

Another effect of the prolonged exposure to thermal cycling, is the growth of the TGO and that stress and strain from growth of the TGO can lead to the failure of TBC. The damage to the TBC system induced by the growth of the oxide layer follows an evolution due to the overlap of different phenomena (Figure 23) [58]:

I) Due to the growth of the oxide layer in the TGO, significant compressive stresses arise especially during the cooling down. In order to accommodate these stresses, the compressed oxide layer tends to increase its length through out-of-planes displacements. This mechanism can occur by buckling phenomena of the TGO and

by visco-plastic deformation of the bond coat. These shifts produce tensile stresses normal to the interfaces which cause the detachment of the TBC.

II) When defects are present around the TGO, tensions are induced normal to the TGO/bond coat. This lead to the nucleation and propagation of cracks at the TGO-top coat interface and to a subsequent TBC delamination.

III) The TBC has a sufficient stiffness to resist a localized buckling (SSB – Small Scale Buckling) of the TGO. Instead, there is a possible failure when the detachment area is sufficiently large (of the order of a few millimetres). The durability of TBC depends on the time/cycles it takes to develop this separation.

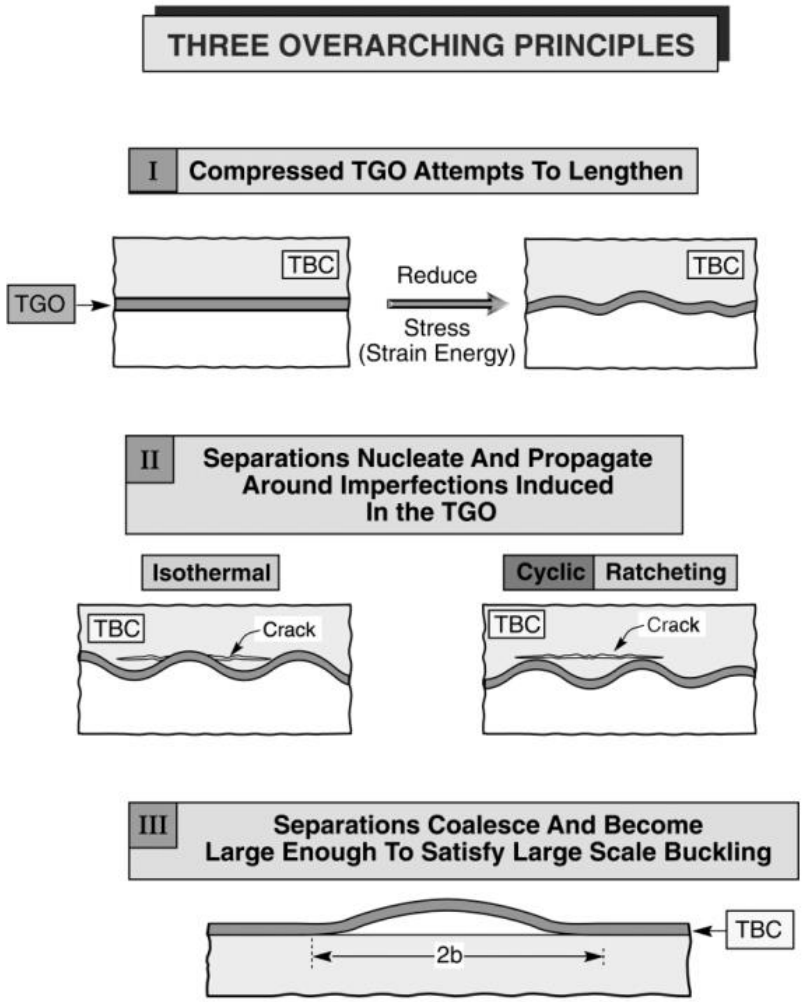

Figure 23 Scheme of three overarching principles for TBC failure [58]

The oxidation kinetics of TGO was reported by Dong et al. and follows the parabolic law (Eq. 4) [59]:

$$\delta = k_p \times t^{\frac{1}{2}} \qquad \textit{Eq. 4}$$

where δ is the TGO thickness, t is the oxidation time and K_p is the parabolic rate constant. The state of stresses induced by the TGO growth was investigated by many authors [58–63]. It was studied that in a rough bond coat/top coat interface, tensile and compressive stresses coexist at the peaks and at the valleys, respectively [64]. With the increasing of the TGO thickness, the nature of the stresses in YSZ coating changes from compression to tension. Stresses generated by this mechanism are able to propagate fatigue cracks at the interface bond coat/top coat, causing the failure of the TBC system.

The growth of TGO reduces the adhesion between YSZ and bond coat [61,65,66]. Dong et al. showed an increasing of TGO thickness after a thermal exposure at 1080° C for different durations [59]. Figure 24 shows the evolution of TGO thickness in YSZ APS coatings. It was observed that when TGO thickness is greater than the 5-6 µm threshold, the thermal cyclic lifetime decreases rapidly. Moreover, it was observed that the cracking modes depend on the TGO thickness. When the TGO thickness is less than 5 µm, the cracking occurs within the YSZ (cohesive failure), while TGO thickness is larger than 6.5 µm, the cracks propagate at the interface TGO/bond coat. These considerations mean that the TCF lifetime depends on the out-of-plane stress induced by combined effects of TGO growth and thermal coefficient mismatch. Moreover, as pointed out by Madhwal et al., the depletion of Al in the bond coat can be a further cause of the coating spallation. When Al content is totally depleted, oxide such as Chromia can form. TGO growth accompanied by oxidation of heavier elements such as Cr can be the cause of the failure of the coating [66].

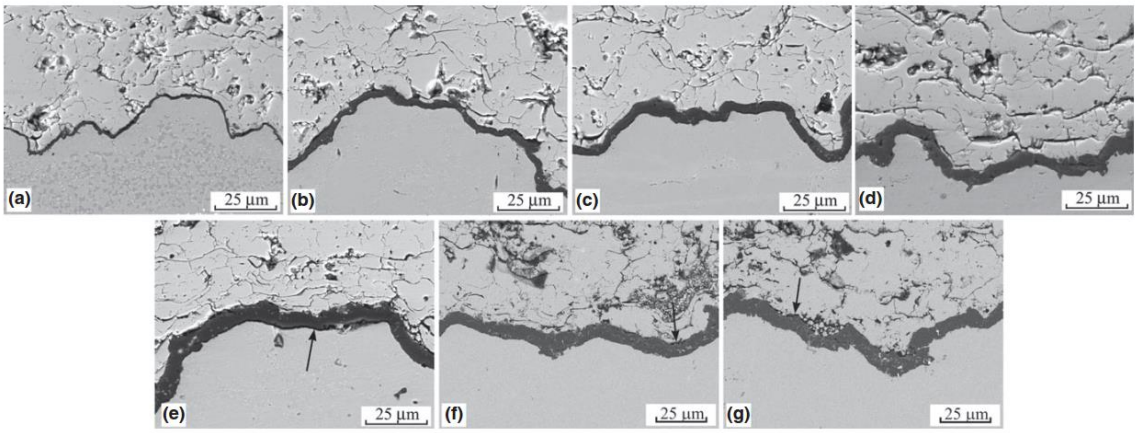

Figure 24 Evolution of TGO thickness after thermal exposure at 1080 °C for 20 h (b), 50 h (c), 105 h (d), 225 h (e), 300 h (f), and 350 h (g); (a) 1.3 µm, (b) 2.7 µm, (c) 3.9 µm, (d) 5.0 µm, (e) 6.5 µm, (f) 7.0 µm, and (g) 7.7 µm [59]

For the evaluation of the thermal resistance of TBCs, two main types of thermal cycling tests are usually employed [67,68]: thermal cycling test (TCF) and burner rig test (BRT).

- In thermal cycling test (TCF), samples are thermally cycled by moving in and out of a furnace. The samples while out of the furnace undergo a forced cooling usually down to room temperature. In this test, the heating rates and the temperature gradients in the samples are lower compared to the burner rig test. Moreover, the high-temperature dwell time is longer than BRT test [68].
- In a burner rig test, a flame is used for heating the coated samples (Figure 25) . The gas temperature reached is around 1350-1750 °C [67]. In order to apply a thermal gradient during heating, the samples are cooled on the uncoated side by compressed air [67].

Thermal cycling degradation is a very critical issue. In this context, EB-PVD, PS-PVD and SPS coatings, characterized by a columnar microstructure, exhibit a higher strain tolerance when exposed to thermal cycling, compared to porous APS coatings [69–73]. The column gaps within the coatings significantly reduce the stress level by opening during the thermal exposure [74].

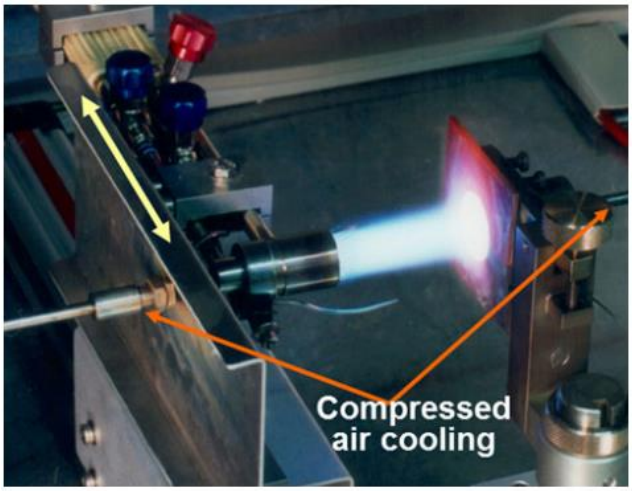

Figure 25 Photograph of the burner rig used for thermal cycling tests on TBCs [75]

1.4.3 Sintering and shrinkage

Another TBC failure mechanism strictly associated to thermal exposure is the sintering of the top coat [76]. Sintering is defined as a process by which ceramic/metallic powders are transformed into dense solids at temperature lower than the melting point. Sintering effects can lead to significant changes on microstructures of top coats, such as the healing of cracks, decrease of porosity and growth of grain size [77,78].

Chernuschi et al. confirmed that sintering takes place in two stages [79]:

- Stage one: it involves the healing of microcracks within the coating at temperatures as low as 900 °C. This stage is active at very short time (<10 h).
- Stage two: it consists of modification of pore shape and shrinkage over longer time periods. This occurs at temperatures around 1200-1300 °C.

These phenomena cause the decrease of strain tolerance and the increase of thermal conductivity. Specifically, sintering induces the increase of Young's modulus and hardness of the ceramic layer. These changes of microstructure and mechanical properties, result in in – plane tensile stresses which lead to the shrinkage at the surface of the top coats and consequently to the cracks propagation within the coating [21].

1.4.4 Infiltration by environment deposits based on calcium magnesium aluminosilicate (CMAS)

When gas turbines operate in dusty environments, they can ingest silicate powders (sand, volcano ash), which then form molten deposits based on CaO-MgO-Al_2O_3-SiO_2 (CMAS) mixtures on the surface of hot-section components. This has been shown to occur e.g. in combustion chambers, transition ducts, and first-stage blades and vanes [80–83]. The presence of these deposits has become a significant issue with the increasing of temperatures (above 1200 °C) at which the gas turbines operate. CMAS accumulates non-uniformly on engine components. Molten silicate particles can therefore stick to hot surfaces and build up a deposit. The amount and the state of deposit depends on the local temperature of the part. For example, on cooler areas of the blade, in correspondence of the cooling air passages, the sand accumulates as a porous deposit [81]. When the local temperature increases, the sand deposit starts to glaze. In the hottest sections, the sand melts, and after cooling, it forms a homogenous amorphous CMAS layer [80,81]. The amorphous deposit consists of a glassy matrix with numerous large pores and second phase precipitates. The porosity within the glassy deposit is known as *frothing* and the causes are the following [81,84]:

1. The thermal decomposition of sand carbonates forms CO_2 gas bubbles via the possible reactions:

$$CaCO_3 \rightarrow CaO + CO_2$$
$$CaMg(CO_3)_2 \rightarrow MgO + CaO + 2CO_2$$

2. The difference in the solubility of gas in the CMAS at high temperature.

The second phase precipitates can be due to un-melted sand or re-crystallization products from the cooling.

The melting point of the silicate-based mixtures is related to their composition, but most values in literature are in the range from 1150-1250 °C [81,85–87]. In this range, CMAS can completely or partially melt and tends to adhere to ceramic top coat. Oxide ceramic surfaces are highly wettable by molten CMAS, because of their chemical affinity [88,89]. Slowly, the molten liquid wets the YSZ TBC and by capillary action infiltrate the open voids in the microstructure [12]. Levi et al. pointed out that chemical and mechanical issues can be associated to CMAS infiltration into a YSZ coating [55]:

- *The mechanical issue.* CMAS attacks TBCs primarily via cold shock degradation mechanism [82,90,91]. It consists of the filling of the voids by molten CMAS followed by solidification during cooling. As consequence, the ceramic top coat becomes stiffer and it loses its elastic compliance and becomes prone to spalling off during thermal cycling (Figure 26) [92]. The elastic modulus of TBC in plane strain condition increases from around 20 to about 200 GPa, contributing to the increase in stored elastic strain energy of the TBC. This stored energy provides the driving force for TBC cracking and delamination [89,93]. The cold shock occurs at high cooling rates [90]. As the delamination takes place near to the surface instead of at the interface with the bond coat, then the spallation is probably due to "cold shock". Cumulative cracks promoted by engine cycles lead to final spallation of TBCs [86]. Lower cooling rates will be dominated by compression in the coating. In this case delamination mainly occurs closer to the interface to the bond coat interface [90,91].

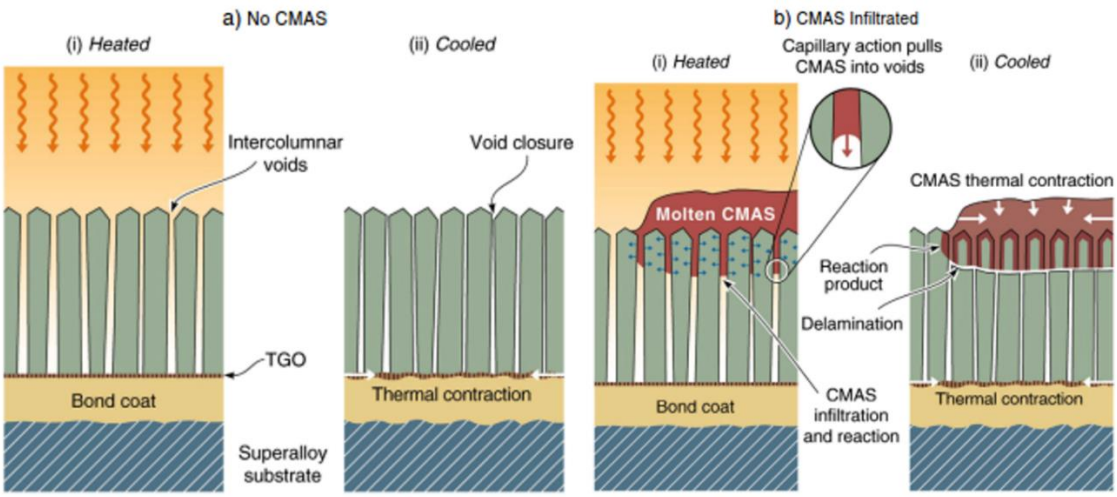

Figure 26 Molten CMAS penetration through a surface heated coating [92]

The buckling mechanism that occurs after CMAS infiltration during prolonged thermal exposure was pointed out by Shan et al. [94]. He explained that at relatively "low" temperature (~764 °C), CMAS becomes soft reaching the melting point at ~ 1233 °C. At this point, CMAS starts to penetrate into pre-existing cracks and pores, driven by the capillary force. As a consequence, CMAS separates inter- and intra-splat boundaries, leading to an increase of the volume of the coating. However, the top coat is physically

constrained by the substrate, thus its volume expansion introduces a compressive stress. Once the interface between top coat and TGO is damaged, the CMAS-penetrated coating starts buckling, leading to relaxation of the compressive stress [94].

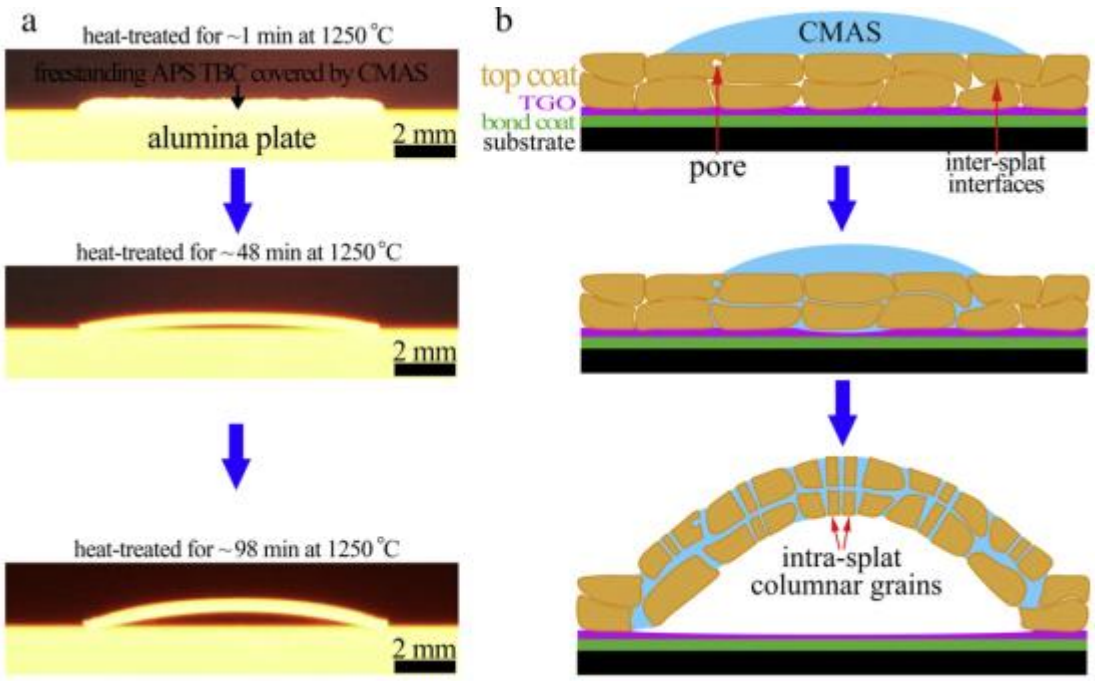

Figure 27 a) Prolonged thermal exposure to CMAS melt that leads to buckling phenomenon; b) Schematic of the mechanism leading to buckling of the APS TBC after CMAS attack [94]

- On the other hand, *the chemical interaction* between CMAS and YSZ top coat can lead to its degradation. The first study concerning the chemical attack was carried out by Scott et al. [95]. He evaluated the CMAS corrosion of APS 8 wt.% YSZ using natural CMAS formers. The experiment was conducted for 120 h at temperatures ranging from 1300-1600 °C. It was found that CMAS dissolved yttria and its depletion led to the conversion of tetragonal phase to monoclinic phase in the YSZ coating. It was also observed that zirconia depleted of yttria can subsequently re-precipitate in form of very fine ZrO_2 grains. The transformation from zirconia tetragonal phase into monoclinic phase during cooling is accompanied by a large volume change (4 -5 vol.%), which can further trigger delamination cracking [80,86,96,97]. The dissolution-precipitation mechanism was investigated by many authors [80,98,99]. When the corrosion is particularly severe, the grain texture loses its cohesion and is converted into globular

grains of mainly monoclinic zirconia [98,100]. These features were mainly highlighted in contact to CMAS melt. Nieto and Kramer also observed twinning characteristics of the martensitic tetragonal to monoclinic transformation in correspondence of the globular particles [98,100,101].

CMAS infiltration behaviour strongly depends on the ceramic top coat microstructure. Delamination of APS and EB-PVD TBCs under CMAS attack was investigated by many authors [80,91,93,102–104]. In porous coatings obtained by APS process, the presence of interlamellar and inter-splat porosity, facilitate the penetration of molten CMAS. However, these features have a smaller size than intercolumnar channels in EB-PVD TBCs, thus CMAS attack is less severe for APS TBCs [105]. The CMAS corrosion behaviour of columnar PS-PVD TBCs was studied by Rezanka et al. [106]. He observed the same infiltration mechanism reported by other authors in tests on EB-PVD systems.

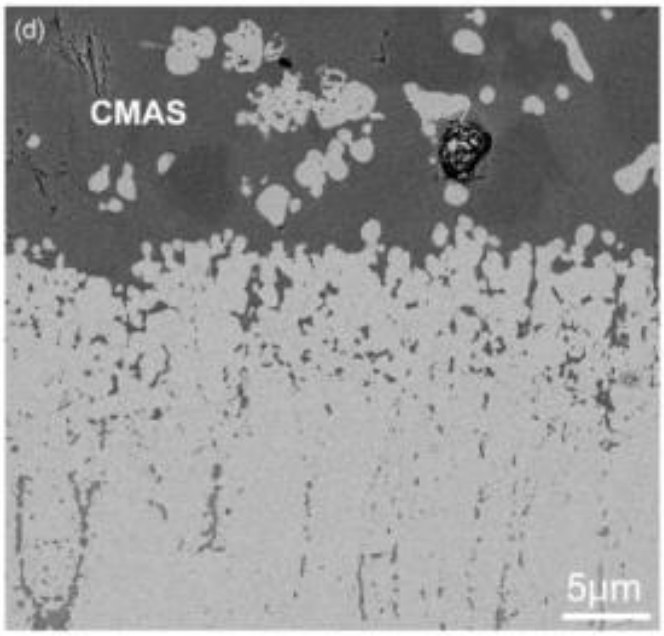

Figure 28 Globular grains observed at the interface between CMAS and YSZ coating [98]

Different degrees of porosity can affect the CMAS behaviour. Li et al studied the CMAS corrosion of YSZ TBCs with different microstructures: low density YSZ (~ 15% porosity); DVC YSZ (~ 8% porosity) and D-gun YSZ (~ 6% porosity). He concluded that a denser coating demonstrates a higher potential to resist the CMAS attack for a longer time than a more porous

coating [107]. Experiments on DVC and porous coatings were also conducted by Gildersleeve et al. [89]. Specifically, in the cited work, two CMAS corrosion methods were performed: CMAS isothermal test at 1200 °C and a CMAS test using a gradient testing rig (e.g. burner rig test). In the latter case, through the injection of CMAS into the flame of the burner rig (see Section 1.4.2), it's possible to simultaneously evaluate the coating resistance under thermal gradient cycling conditions and CMAS attack. Results of the isothermal test revealed that the location at which delamination occurs and the degree of failure are comparatively the same between DVC and porous YSZ, but the ways of infiltration can be different [89]. The infiltration pathway by capillary action, through the vertical cracks of DVC coatings, results to be similar to that of EB-PVD coatings. Very frequently, in DVC coatings, the branching of the vertical cracks can occur. Sometimes these branching cracks can extend up to horizontal cracks in correspondence of the interface between coating deposition passes. These so-called "inter-pass boundaries" (IPBs) when filled by CMAS melt, can be the causes of the onset of cracks propagation after CMAS solidification. Differently, when a thermal gradient is present, the infiltration depth of CMAS melt can be a function of the coating architecture/microstructure and the surface temperature. In a DVC TBC the thermal gradient is reduced because of its higher thermal conductivity than that of the porous TBC. For this reason, in the porous coatings the infiltration depth was lesser than that of DVC ones. It was also highlighted that in the case of a porous coating, there was a CMAS build-up on the surface, while in DVC coatings the penetration of CMAS was limited to the vertical cracks. In this latter case Gildersleeve et al. noted an evident difference between isothermal and gradient test (Figure 29) [89]. Indeed, the penetration of CMAS into IPBs was much less due to the presence of a thermal gradient and as well the short duration of this test compared to the isothermal test. Thus, the complete spallation of the coating doesn't occur.

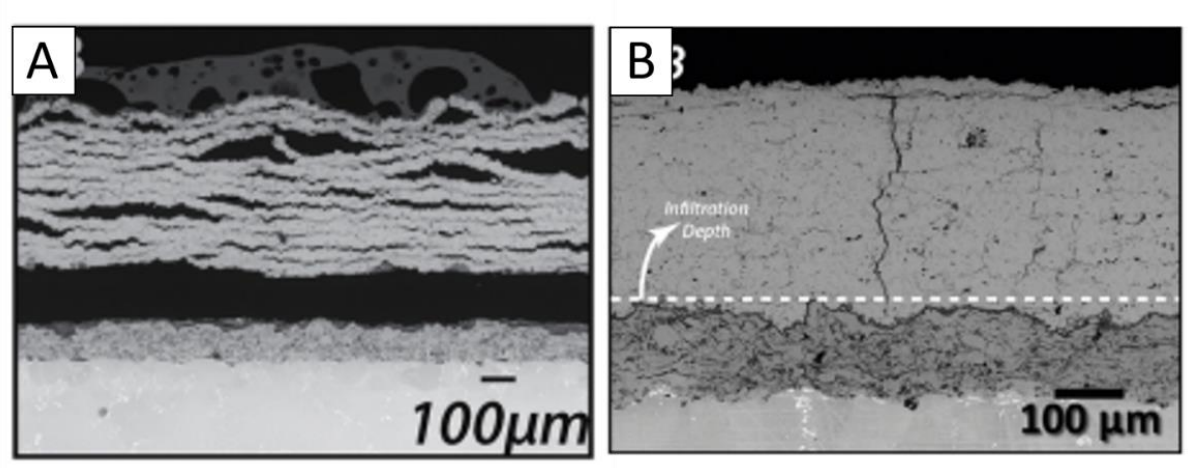

Figure 29 DVC coatings subjected to an isothermal test (A) and to a gradient test (B) [89]

High-temperature reactivity of CMAS corrosion can be approximately evaluated with optical basicity (OB) theory [105,108,109]. Following the approach by Krause et al. [109], the optical basicity of an oxide can be a predictor of its tendency to react with CMAS. Optical basicity describes the amount of electrons available for transfer to other compounds, extending the classical Lewis acid-base definition to non-aqueous systems [110]. In particular, for oxides, it describes the amount of negative charge available on the oxygen anions and, therefore, the ability of O^{2-} to donate electrons, which depends on the type of cations. Normally, in the free state, the O^{2-} has the maximum aptitude to donate electrons. When O^{2-} is bound to other cations, the ability to transfer a negative charge can be limited. Cations with high charge density, like Si^{4+} (high charge/radius ratio) draw electrons away from oxygen, thus the oxide acts as an acid (low optical basicity). Cations with lower charge density allow oxygen to donate electrons to other available cations, thus the corresponding oxide has a basic behaviour and a correspondingly high optical basicity [105]. The term "optical" derives from the fact that this parameter is typically inferred from UV spectroscopic measurements of the energy gap between the outer electron shells of cations to identify their true valence [110].

Referring to CMAS corrosion processes, the greater the difference in optical basicity between a compound and CMAS, the greater the reactivity between them, hence the tendency to form compounds, which might develop into protective layers that block further interactions. By contrast, a compound whose optical basicity is close to that of CMAS would probably dissolve easily without developing any reaction product. The optical basicity (Λ) of a compound or

mixture consisting of several binary oxides is defined as $\Lambda = \sum_i X_i \Lambda_i$, where X_i and Λ_i are the mole fraction of the *i*-th constituent of the compound and its optical basicity, respectively [109]. In Table 1 and in Table 2 the values of optical basicity of various TBCs and some oxides that will be useful to evaluate the reactivity between all TBCs studied in this thesis and CMAS are reported.

Table 1 Calculated optical basicities of various TBC materials [109]

TBCs	EBCs	Ref.	CN Zr^{4+} or Al^{3+}	Λ
$Gd_2Zr_2O_7$ (P)	–	12,26,27	6	1.16
$Nd_2Zr_2O_7$ (P)	–	30,55	6	1.17
$La_2Zr_2O_7$ (P)	–	30	6	1.16
$2ZrO_2{\cdot}Y_2O_3$ (F)	–	26,70	7	0.99
$Yb_2Zr_2O_7$ (F)	–	26,30	7	0.96
7YSZ	–	9,26	8	0.87
–	$Gd_4Al_2O_9$	62	4	0.99
–	$Y_4Al_2O_9$	62	4	0.87
–	$GdAlO_3$	62	6	0.79
–	$LaAlO_3$	62	6	0.79
–	Y_2SiO_5	61,63	–	0.79
–	Yb_2SiO_5	66	–	0.76
–	$YAlO_3$	60	6	0.70
–	$Y_2Si_2O_7$	63,64	–	0.70
–	$Yb_2Si_2O_7$	64,66	–	0.68
–	$Sc_2Si_2O_7$	64	–	0.66

(F), Fluorite; (P), Pyrochlore.

Table 2 Optical basicities of some oxides [109]

Oxide	Λ
K_2O	1.40
Nd_2O_3	1.19
Gd_2O_3	1.18
La_2O_3	1.18
Na_2O	1.15
TiO_2	1.00
Fe_2O_3	1.04
CaO	1.00
MnO	1.00
Y_2O_3	1.00
Yb_2O_3	0.94
Sc_2O_3	0.89
ZrO_2[†]	0.86
MgO	0.78
Al_2O_3[‡]	0.60
SiO_2	0.48

1.5 New advanced ceramic top coats

As already mentioned, above 1200 °C, the ingestion of sand/ash deposits can be a significant issue. In this regard, over the last 20 years, other strategies to mitigate the corrosion by these glassy deposits were carried out. Several papers have been focused on the CMAS corrosion of a number of ceramic chemistries which could be valid alternative to YSZ coatings. The research of new advanced ceramic top coat was primarily made based on their lower thermal conductivity (Figure 30) and higher resistance to sintering than standard YSZ [111]. Bakan et al. have reported four different ceramic material groups widely studied [74]:

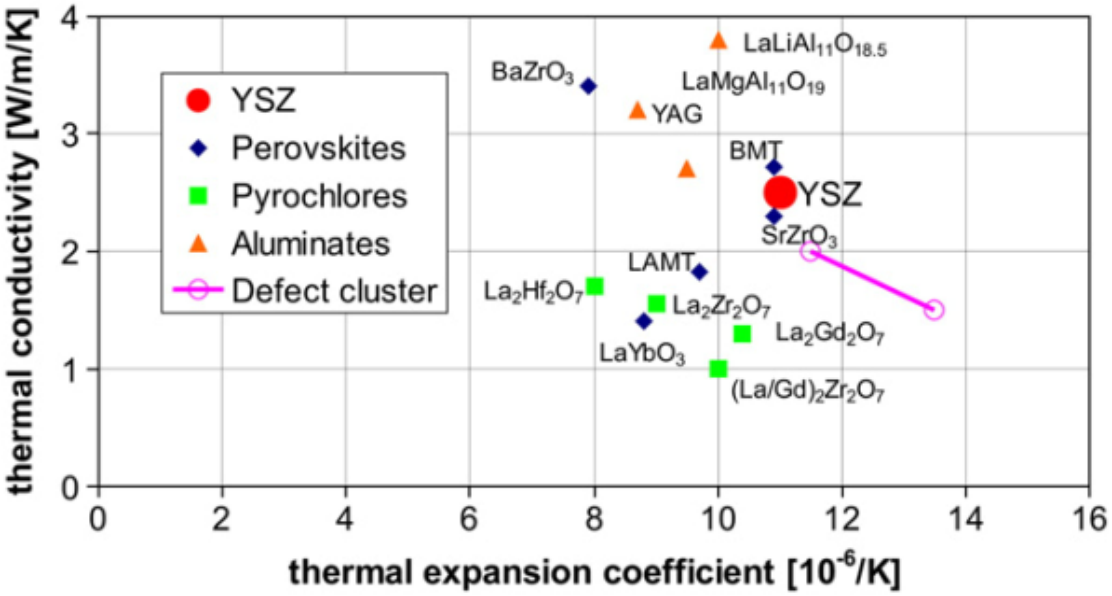

Figure 30 Thermal conductivity and thermal expansion coefficients of dense, new thermal barrier coatings [112]

Zirconia doped with different rare-earth (RE) cations (defect cluster TBCs): the incorporation of oxides of the different RE cations within zirconia allows to effectively reduce the thermal conductivity of the material. Zhu et al. demonstrated that zirconia doped with 5.5 mol.% Y_2O_3 - 2.25 mol.% Gd_2O_3 - 2.25 mol.% Yb_2O_3 has a thermal conductivity of 1.7 W/mK compared to the 2.5 W/mK of ZrO_2 - 4.5 mol.% Y_2O_3 system [113]. These coatings have produced similar thermal cycling performances to that of YSZ TBCs, but it was also observed that increasing the level of dopants within zirconia, there is a reduction of thermal conductivity

compared to 7-8 wt.% YSZ [112,114]. The CMAS corrosion behaviour of defect cluster coatings is little investigated. In a recent study focused on the CMAS corrosion of YbYSZ compared to YSZ [115], it was noted that the addition of Yb_2O_3 to zirconia slows down the transition from tetragonal to monoclinic phase. After a longer exposure to CMAS, the zirconia monoclinic phase was detected in YbYSZ, differently to YSZ [115]. The dissolution and reprecipitation during the CMAS attack of YbYSZ occur, but a low amount of RE: Zr in CMAS in YbYSZ was found. This was attributable to the lower diffusion rate of Yb^{3+} during the CMAS attack, due to its larger atomic mass and larger ionic radius compared to Y^{3+}. This mechanism reduces the degradation of grains and inhibits the CMAS penetration.

Perovskites: these materials with a structure ABO_3 can be considered promising candidates because of their high melting point ($SrZrO_3$; 2650 °C, $Ba(Mg_{1/3}Ta_{2/3})O_3$; 3100 °C); high CTE and a thermal conductivity lower than 2.2 W/mK. However, some limitations were also found for this class of materials. For example, $SrZrO_3$ presents a phase transformation from orthorhombic to pseudo-tetragonal phase at 740 °C which is accompanied by a volume change of 0.14%. These coatings can be very effective protective coating if used in double layer system, acting as top coat on YSZ bottom layer or doped with other materials (Gd_2O_3 or Yb_2O_3). Singularly, they don't exhibit good corrosion resistance [115], but if furtherly coated with a pyrochlore coating (eg: $La_2Zr_2O_7$-$SrZrO_3$), they can prevent the failure by molten CMAS [116].

Hexaaluminates: among this class of materials, particular attention is given to lanthanum magnesium hexaaluminate ($LaMgAl_{11}O_{19}$, LMA) with a magnetoplumbite-type structure. This material is characterized by a low thermal conductivity (0.8-2.6 W/mK), high fracture toughness (~ 3.59 $MPa \cdot m^{1/2}$), high CTE (9-11 × 10^{-6} K^{-1}, 200-1200 °C), excellent sintering resistance and outstanding thermal stability up to 1600 °C. Zeng et al. discussed the reaction mechanism between CMAS and LMA. He showed that CMAS completely infiltrated into LMA coating, leading to the formation of $CaAl_2Si_2O_8$ and $MgAl_2O_4$ in the outer layer (area in contact with molten CMAS), and with the further penetration and reaction with CMAS, the formation of $Ca_3La_6(SiO_4)_6$ [117]. The formation of these reaction products doesn't provide an effective protection against CMAS.

Pyrochlores: this group of materials exhibits a lot of advantages for applications where the service temperature is above 1300 °C. Pyrochlores with a structure $A_2B_2O_7$ can be promising candidates, especially for they CMAS corrosion resistance. Rare – earth zirconates ($Ln_2Zr_2O_7$)

coatings, where Ln is any or combination of La, Gd, Sm, Nd, Eu, and Yb were widely investigated. These materials, thanks to the high concentration of intrinsic oxygen vacancies, high-level cation substitution (versus YSZ), and large atomic mass difference between zirconia and large lanthanides, which increases the phonon scattering strength of the point defects, exhibit low thermal conductivity [118]. Values of thermal conductivities vary from 1.2 and 2.2 W/mK, while CTEs of the dense pyrochlores were reported between 9.1 and 12.2×10^{-6} K^{-1} at 1000 °C [43]. In general, CTEs of the pyrochlores are close to that of the standard 8YSZ (10×10^{-6} K^{-1}) [74]. Another important benefit of $Ln_2Zr_2O_7$ is their high-temperature phase stability. The temperature at which pyrochlores are subjected to an order - disorder transition from defect fluorite structure (F) to pyrochlore structure (P) depends on the type and the size of the former (Ln: La, Nd, Sm, Eu, Gd). For example, $Nd_2Zr_2O_7$ has a higher stability temperature (2310 °C) compared to $Gd_2Zr_2O_7$ (GZO) (1550 °C), because Nd has a higher Ln cation size (ionic radius) [74]. It was also observed that for GZO coatings, in contrast to YSZ, the transition from defect fluorite to ordered pyrochlore structure during gradual cooling is not accompanied by any volumetric expansion [119].

Studies on GZO as alternative to YSZ have revealed some limitations when it is used as a single layer [43]:

1. GZO has a lower CTE (8.1-12.2 × 10^{-6} K^{-1} at 200-1000 °C) than nickel superalloy substrate (16×10^{-6} K^{-1}). This can induce higher thermal stresses from thermal expansion mismatch [43];
2. lower fracture toughness (0.8 MPa·$m^{1/2}$) than that of standard YSZ (2.6 MPa·$m^{1/2}$) This can be the cause of the early onset of crack propagation, even at low-stress levels [43];
3. GZO tends to react with TGO at high temperatures (1100-1200 °C) (Figure 31), forming an undesired porous layer of $GdAlO_3$ perovskite [120].

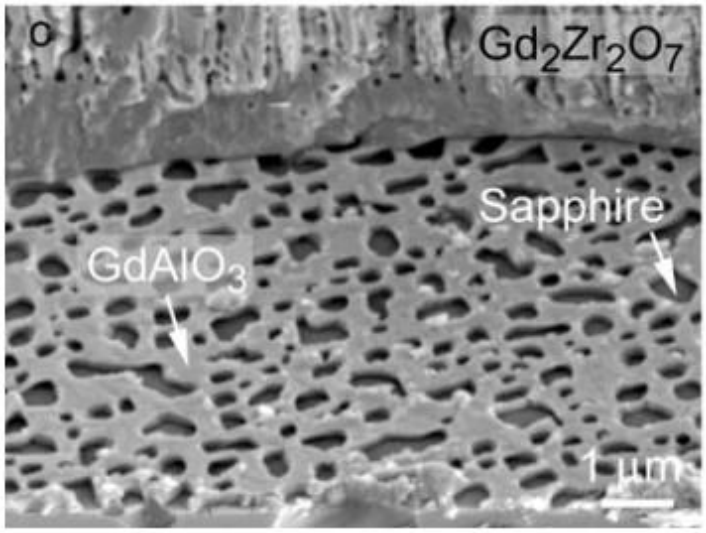

Figure 31 Porous layer due to the reaction between $Gd_2Zr_2O_7$ and TGO [120]

Thermal cycling performances of pyrochlores can be enhanced doping them with other stabilizers such as Dy. The addition of 60 mol.% within GZO imparts a fracture toughness of 1.82 $MPa \cdot m^{1/2}$ [121]. Another strategy is the reduction of the RE_2O_3 content. Schmitt et al. showed that by reducing the $GdO_{1.5}$ content from 50 mol.% to 15.66 mol.%, an increase of fracture toughness of 1.25 $MPa \cdot m^{1/2}$ was achieved [122]. On the contrary, the use of GZO coating can be effective as protection against CMAS infiltration. In several studies was reported the mechanism of dissolution and re-precipitation of GZO. As discussed by Wang et al., the main reaction products, observed after the CMAS attack, are apatite phase $Ca_2Gd_8(SiO_4)_6O_2$ and a zirconium-enriched cubic fluorite phase depleted in gadolinium $Zr_2Gd_{2-x}O_7$. In particular, the excellent CMAS resistance was given by the precipitation of the high-stable apatite phase which seals the microstructure avoiding further CMAS penetration [123].

For these reasons, GZO coatings result to be more performant when used as double layer. Indeed, the use of multilayer systems consisting of a high fracture toughness YSZ bottom layer and a CMAS resistant GZO as top coat can overcome all drawbacks of GZO coatings used as single layer [56].

1.6 Multilayer systems

Manufacture of multilayer topcoats is a recent approach to resolve the issue of phase transformation of zirconia in YSZ TBCs. In the last decade, layered architectures have been produced to improve the durability of TBCs in harsh environments [43]. Some authors experimented advanced material ($La_2Ce_2O_7$, $La_2Zr_2O_7$, $Gd_2Zr_2O_7$, $Nd_2Zr_2O_7$, $La_2Hf_2O_7$, etc.) as top coats of a transition YSZ layer because they possess low thermal conductivity and chemical phase stability at high temperatures [124–126]. On the other hand, these materials employed as single layer possess a low thermal cycling resistance. For this reason, it has become necessary to apply a high toughness YSZ interlayer which improves the TBC durability.

A relevant study on CeO_2/ZrO_2 bilayer system was carried out by Wilden et al. [127]. He showed an effective improvement of thermal capability up to 1400 °C.

Mensah et al. studied bilayer systems consisting of 25 wt.% $Gd_2Zr_2O_7$(GZO)/YSZ, 50 wt.% GZO/YSZ, and 75 wt.% GZO/YSZ for improving the thermal cycling resistance [128]. Further improvements of thermal resistance were obtained by modifying the microstructure of GZO. Porous-GZO/YSZ demonstrated longer thermal cycling durability than dense-GZO/YSZ coatings [129]. Once demonstrated the effective potentialities of GZO/YSZ bilayer systems, Viswanathan et al. investigated three layered TBCs consisting of a top dense vertically cracked GZO layer applied on the top of bilayer YSZ system (Figure 32) [56]. He introduced a dense, high toughness YSZ layer on the metallic bond coat to avoid the rapid delamination of the TBC. This layer was followed by a thick porous YSZ layer with a low elastic modulus and low thermal conductivity. The top coat consisting of a dense GZO layer was designed to mitigate the CMAS corrosion and to resist to solid particles erosion [56].

GZO/YSZ SPS TBCs exhibited higher thermal cycling life and lower thermal conductivity compared to YSZ single layer [45,130].

Wang et al. studied the CMAS corrosion resistance of bilayer $La_2Zr_2O_7$(LZ)/YSZ obtained by APS process [131] . He pointed out that the top coat was very effective against CMAS attack because of the formation apatite phase $Ca_{2\cdot67}La_{1\cdot33}Zr_{1\cdot33}O_{7\cdot33}$ and fluorite phase ZrO_2 which inhibits penetration of the CMAS into the ceramic coating [131]. In addition, he showed that the residual stresses in bilayer $La_2Zr_2O_7$(LZ)/YSZ after CMAS attack were smaller than those in YSZ and LZ single layers, concluding that the bilayer system was more difficult to peel off under condition of high temperature CMAS corrosion [131].

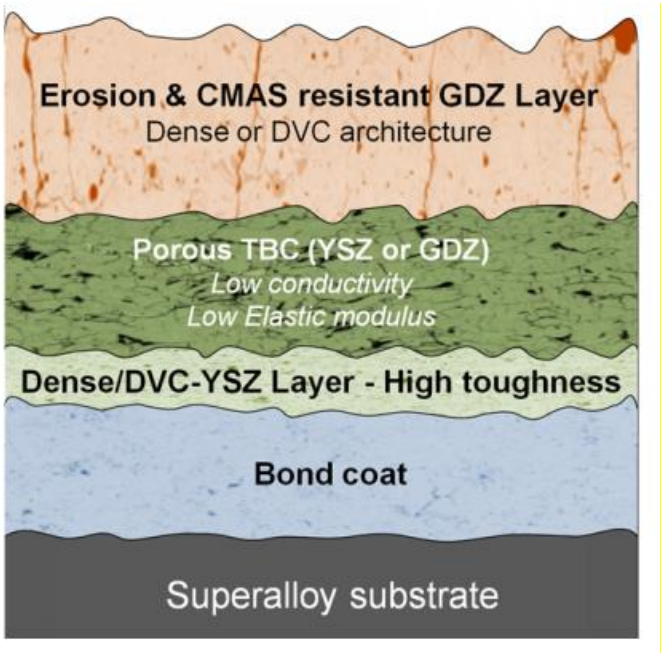

Figure 32 Schematic illustration of multi-layered TBC [56]

Ozgurluk et al. investigated the behaviour of bilayer GZO/YSZ obtained by EB-PVD technique [132]. He showed that the combination of these two layers allows to obtain a performant TBC. The presence of GZO as upper layer slows the penetration of CMAS into the YSZ layer. Moreover, he underlined that crack delamination occurred only in GZO layer because of its low fracture toughness [132].

However, few literature works tackled the topic of CMAS corrosion of multilayer coatings. It is therefore necessary to examine the behaviour of multilayer with different materials as top coats and YSZ as intermediate layers, by examining the various possible combinations among architectures. This is exactly the purpose of the research activity conducted in the last three years.

2 Experimental procedure

This chapter includes all coatings' composition tested during the Ph.D. activity. The thermal spraying processes and the deposition parameters to spray them are reported. A chemical and microstructural characterization of the coatings was preliminary carried out and then CMAS corrosion test and thermal cycling fatigue test were performed in order to explore the coatings performances.

2.1 Spraying Facility

To deposit SPS and porous APS coatings, a *Cascaded arc torch (proprietary equipment – Lincotek Surface Solutions)* was used. Differently to the conventional APS torch, the cascade torch consists of a stack copper rings insulated from each other called *neutrodes*, ending with and anode ring on which the arc attaches. This advanced torch allows to improve the arc stability, as the fluctuation of the arc is restricted to a small portion inside the anode ring [133]. The greater stability of the arc allows a lesser rate of erosion at the arc attachment point, as well as plasma characteristics more constant over time. Compared to a traditional torch, the cascade torch works with lower currents and higher voltages.

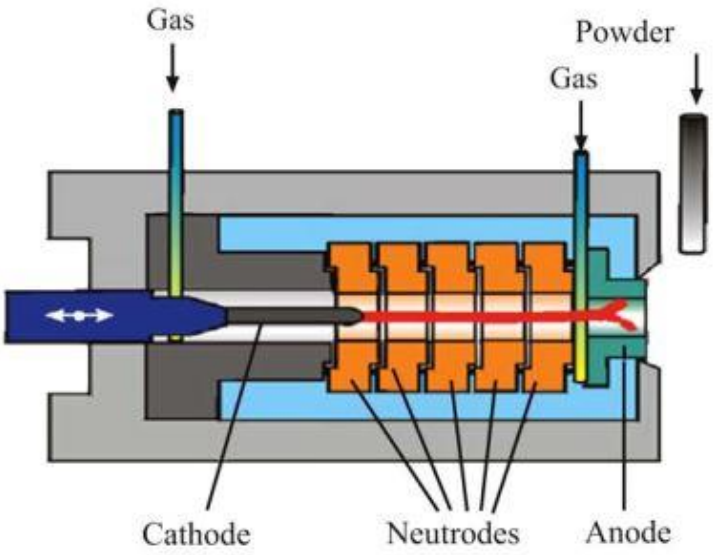

Figure 33 Schematic of a Cascade torch [134]

Plasma-forming gases used for the depositions are a mixture of Ar/H_2. The spray parameters are data proprietary of Lincotek company and they cannot be disclosed because of NDA agreement.

For all depositions the equipment in Figure 34A was used. A suspension feeder with a peristaltic pump was installed (Figure 34B) to deposit the SPS top coat.

Both APS and SPS depositions were carried out in rotation mode. The samples were mechanical mounted on sample holder, rotated by a turntable. The back side of the sample holders was connected to cooling air supply to maintain a desired deposition temperature during spraying. The image of a sample fixed on the sample holder is presented in Figure 34C.

The torch was moved linearly in front of a turntable in which substrates were mounted. The linear torch velocity and the revolution speed of the turntable were adjusted in order to achieve the desired scan speed and pitch distance (measured in mm/rev). In this thesis the vertical movement of the torch with respect to the rotating cylinder is defined as “pass”.

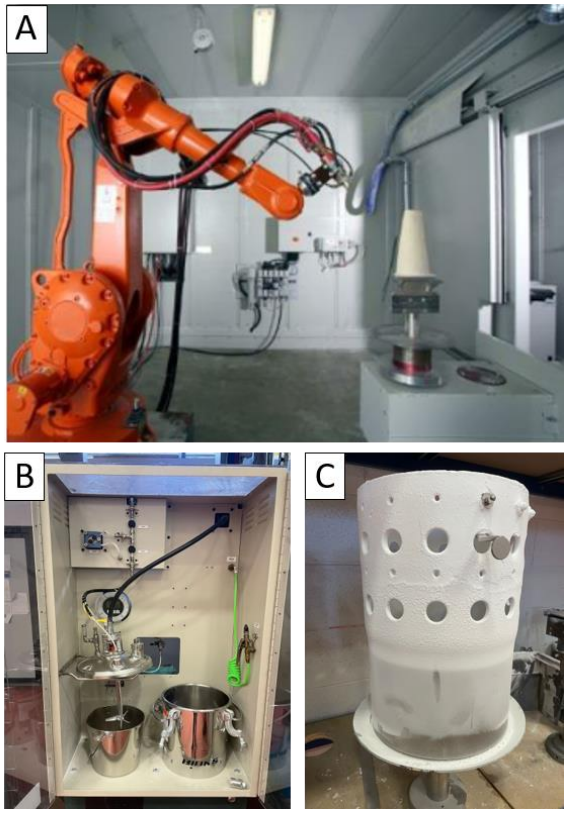

Figure 34 A) photograph of plasma spray equipment; b) peristaltic pump for suspension plasma spraying system; c) samples holder

2.2 Feedstock materials

2.2.1 Part I: influence of microstructure and purity of feedstock powders on CMAS resistance of TBCs

The first part of this thesis concerns the study of four different feedstock materials, all corresponding to the ZrO_2 + 7–8 wt.% Y_2O_3 stoichiometry but characterized by different purity grades (Table 3). In all cases, the substrates were Hastelloy-X discs of 25.4 mm diameter × 3 mm thickness, preliminarily coated with a NiCoCrAlY bond layer by the High Velocity Oxygen-Fuel (HVOF) thermal spray process. The bond coat was vacuum heat-treated at ~ 1100 °C for 2h before depositing the top coat, as is common practice in the manufacturing of TBCs on gas turbine parts, in order to achieve densification, precipitation of the β-NiAl phase, and metallurgical bonding to the substrate. The roughness of the bond coat was R_a > 10 µm. All TBC systems were deposited at Lincotek Surface Solutions (Rubbiano di Solignano, Italy) facility using well consolidated parameters; hence, the samples can be regarded as representative of the state of the art.

Table 3 feedstock materials employed for each deposition process, with chemical composition and particle size distribution (from manufacturers' analysis certificates) [135]

Feedstock type		Standard-purity dry powder (Agglomerated & sintered)	High-purity dry powder (Agglomerated & sintered)	High-purity dry powder (Fused and crushed)	High-purity suspension (25 wt.% solid in ethanol) *
Manufacturer / commercial designation		Höganäs / Amperit 827.007	Höganäs / Amperit 816.893	Höganäs / Amperit 825.001	Treibacher Industrie AG
Deposition process		APS (conventional)	APS (conventional)	APS (DVC coating)	SPS
Chemical composition in oxides (wt.%)	*SiO_2*	0.10	<0.01	<0.1	<0.01
	TiO_2	0.08	<0.01	<0.1	<0.01
	Fe_2O_3	0.01	<0.01	<0.1	0.01
	Al_2O_3	0.10	0.01	<0.1	<0.01
	HfO_2	1.9	1.9	1.9	1.9
	MgO	<0.1	<0.01	/	<0.01
	CaO	0.03	<0.01	/	<0.01
	Y_2O_3	7.4	8.16	7.0	8.0
	ZrO_2	Bal.			
Particle size distribution : d_{10} / d_{50} / d_{90} [µm]		23 / 48 / 85	52 / 69 / 100	19 / 33 / 54	0.26 / 0.60 / 1.32

* The chemical composition and particle size distribution of this feedstock refer to the solid fraction (data from manufacturers' analysis certificates)

2.2.2 Part II: influence of top coat chemistry and TBCs architecture on CMAS corrosion and TCF resistance

In the second part of the thesis, multilayer systems have been design. The first part of the multilayer consisted in depositing a metallic bond coat and then a YSZ coating as interlayer. This strategy allows to improve the thermal cycling durability by providing enhanced toughness and better thermal expansion matching at such critical interface. To overcome the disadvantages of YSZ in contact with CMAS, e.g. the tetragonal-monoclinic transformation in zirconia after exposure to CMAS, alternative materials to YSZ as top coats that can withstand higher temperatures and show a higher CMAS resistance have been used.

Based on the state of the art, different chemical compositions (Table 4) deposited by APS process with dense-vertically cracked (DVC) microstructure were studied. In addition, 6 ceramic bilayers where YSZ (in porous or DVC form) was employed as a bottom layer, below top layers made of the three novel materials (Table 5). All the results were compared to standard 7YSZ coatings deposited by APS with both DVC and lamellar/porous microstructure. All top coats were deposited onto Hastelloy-X discs of 25.4 mm diameter × 3 mm thickness, preliminarily coated with a NiCoCrAlY bond layer by the High Velocity Oxygen-Fuel (HVOF) thermal spray process.

Table 4 list of feedstock materials

Composition	**Manufacturing process**
ZrO_2-7 wt.% Y_2O_3	Agglomerated and sintered
ZrO_2-7 wt.% Y_2O_3	Fused and crushed
$Gd_2Zr_2O_7$	Agglomerated and sintered
ZrO_2-55 wt.% Y_2O_3	Fused and crushed
ZrO_2 -22 wt.% (Gd_2O_3-Yb_2O_3-Y_2O_3)	Agglomerated and sintered

Table 5 list of tested combinations

ID	Bottom layer	Bottom layer Microstructure	Top layer	Top layer Microstructure	TBCs architecture
M1	-	-	7YSZ	porous	Monolayer
M2	-	-	7YSZ	DVC	
M3	-	-	$Gd_2Zr_2O_7$		
M4	-	-	Gd/Yb/Y-ZrO_2		
M5	-	-	ZrO_2-55 wt.% Y_2O_3		
B1	7YSZ	porous	$Gd_2Zr_2O_7$	DVC	Bilayer
B2	7YSZ	porous	Gd/Yb/Y-ZrO_2		
B3	7YSZ	porous	ZrO_2-55 wt.% Y_2O_3		
B4	7YSZ	DVC	$Gd_2Zr_2O_7$		
B5	7YSZ	DVC	Gd/Yb/Y-ZrO_2		
B6	7YSZ	DVC	ZrO_2-55 wt.% Y_2O_3		

2.3 Characterization techniques

2.3.1 Powders characterization

The feedstock powders employed in the second part of the thesis were characterized using:

2.3.1.1 Laser scattering analysis

Laser scattering analysis (Mastersizer 2000 granulometer, Malvern Instruments, Malvern, UK) to measure particle size distribution; a wet dispersion technique (Hydro 2000-S dispersion unit) was used, and ultrasounds were applied to de-agglomeration.

2.3.1.2 Scanning Electron Microscopy

Scanning Electron Microscopy (SEM; Quanta 200 and Nova NanoSEM-450, FEI, Eindhoven, NL) and EDS microanalysis (INCA, Oxford instruments, Oxford, UK, and Quantax-200, Bruker Nano GmbH, Berlin, Germany) were employed to investigate surface morphology and cross-sectional microstructure, operating with a 15 keV electron beam. Cross sectional microstructure was obtained by cold-mounting powders in two component epoxy resin, ground

with SiC papers (up to 2500 mesh), polished with 3 µm diamond slurry and 60 nm-sized colloidal oxide polishing silica suspension silica (OPS), cleaned ultrasonically in acetone.

2.3.2 Coatings characterization

2.3.2.1 Differential thermal analysis (DTA)

The thermal behaviour of the CMAS mixture was studied by differential thermal analysis DTA. This technique measures the difference in temperature ΔT, between the sample and a reference material during heating program [136]. The DTA is able to provide qualitative information on the physico-chemical processes which occur in the sample. Through this analysis it's possible to evaluate the following data:

- the temperature at which the thermal phenomena (phase transition, melting points, crystallization temperatures, and others) occur;
- the nature of the thermal phenomenon (endothermic or esothermic).

In this thesis a DTA: STA 429, Netzsch, Selb, Germany was used. It was set a heating rate of 10 °C/min.

2.3.2.2 CMAS corrosion test

CMAS was produced starting from reagent-grade MgO, $CaCO_3$ and SiO_2 (< 325 mesh, Sigma-Aldrich) and Al_2O_3 (Martoxid MR-70, Martinswerk, Bergheim, Germany), mixed in suitable amounts in order to produce the eventual composition listed in Table 6, and melted at 1250 °C. This composition is similar to that of CMAS mixtures employed in several other literature studies [107,120,137]. It reproduces, in a simplified manner, the actual composition of silicate deposits found in serviced turbines. CMAS powder was mixed with water in 1:2 (powder: water) proportion in weight, and deposited onto half of the surface of the coated discs (0.2 g/cm^2) (Figure 35 - the bottom halves of the two specimens are covered by the CMAS mixtures). The microstructure of the coating portion subjected to CMAS corrosion can thus be directly compared to a coating exposed to high temperature without CMAS. Samples were heat-treated in a muffle furnace in air at 1250 °C for 1 h (Heating rate: 10 °C/min).

Table 6 chemical composition of the synthesized CMAS mixture (wt.%)

Oxide	CaO	MgO	Al_2O_3	SiO_2
Concentration (wt.%)	33	7	12	48

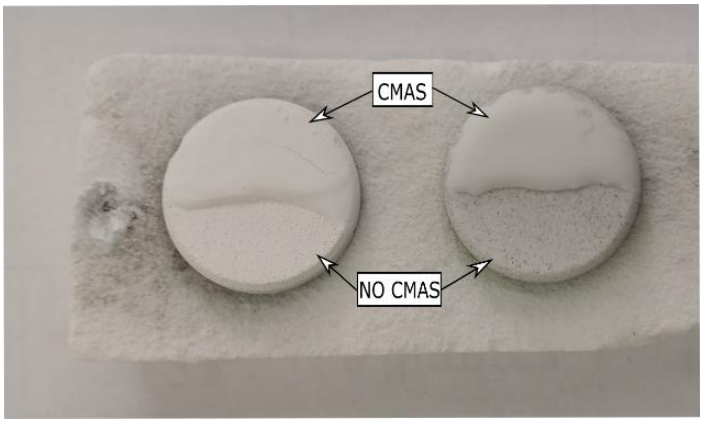

Figure 35 Samples coated with CMAS before the heat treatment at 1250 °C

2.3.2.3 Thermal cycling fatigue (TCF) test

This test allows to evaluate the behaviour of TBCs at high temperatures, simulating the condition of exercise of gas turbines. Thermal contractions induce stresses at the interface between different materials and represent one of the main causes of TBCs failure. A programmable cycling furnace was used for evaluating the thermomechanical resistance of the investigated coating materials and architectures (Figure 36). The furnace consists of two chambers: the first is exposed to atmosphere at room temperature in order to allow cooling; the second chamber is heated by electrical resistances and insulated to limit heat loss during the heating and to maintain stable the temperature of the cycle. The samples are placed on a holder plate, moved by an automated system which allows the movement between the two chambers.

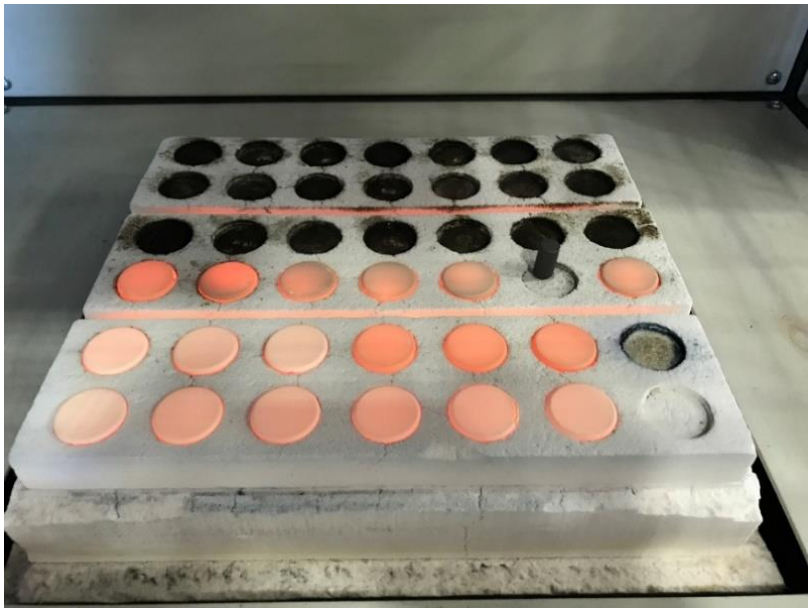

Figure 36 Samples heat treated in the cycling furnace

During the test, samples were heated and cooled. All samples have been subjected to thermal cycles consisting of:

- a rapid heating (150 °C/min) to 1100 °C;
- an isothermal soaking at 1100 °C for 50 minutes;
- a rapid cooling (100 °C/min) from 1100 °C to 100 °C.

The test was stopped when the ~ 20% of area of the ceramic top coats was spalled or in some cases when a predetermined numbers of cycles was reached. For each sample, three thermal cycling test repetitions were performed on as-sprayed top surfaces.

2.3.2.4 Sample preparation for coating characterization

After CMAS attack all samples were observed via SEM in cross-section. For SEM cross-section observation, the following steps were made:

- The sample was embedded in a sample holder. Then a mixture of resin and hardener with a 5:1 ratio was poured on the coated surface and left hardening overnight. This step was necessary to preserve the coating during the cutting step.
- The embedded samples were cut with a cutting machine equipped with abrasive alumina blades in phenolic matrix, with a constant flow of coolant mixture of water and oil. The

cuts were carried out taking care to move the grinding wheel in a way that allows to impose a compressive stress on the coating towards the substrate, in order to reduce the possible delamination.

- The embedded samples have been ground and polished, always keeping in a compressive state the coatings towards the substrate, using a progressively finer sequence of silicon carbide (SiC) abrasive papers (mesh 400, 800, 1000, 2500), and then cloth-polished with a 3 μm diamond suspension and an oxide polishing suspension of 10 nm colloidal silica.

2.3.2.5 Scanning electron microscopy (SEM)

A scanning electron microscope is able to acquire images by scanning the surface of a sample with an electron beam [138].

The primary electron beam is emitted from an "electron gun", which can be based on thermionic emission (tungsten electron gun) or on field emission or both. The electrons are accelerated by an annular anode and focused into a small-diameter beam (10 Å) through suitable electromagnetic lenses. The beam is scanned in a raster patterns over the substrate through a pair of coils placed in the vicinity of the objective lens.

Beam energies typically vary from 1 keV up to 30 keV. Numerous interaction phenomena occur between the electron beam and the sample, all of which could theoretically be exploited for image generation through suitable detectors; usually, three types of interactions are employed in normal SEM instruments.

- Secondary Electrons (SE) are emitted from the topmost layers of the sample as a consequence of inelastic impact of the primary beam with the electrons contained in the outer shells of the atoms in the sample. Due to their low energy, only the secondary electrons produced within a depth of few nanometres below the sample surface can make it out of the sample. The SE therefore return topographical information.
- Back Scattered Electrons (BSE) are primary beam electrons that experienced elastic scattering by the sample atoms. Backscattered electrons are more energetic; hence, they carry information from deeper depths below the sample surface, up to few micrometres. The backscattering intensity depends on the average atomic weight of the area hit by the electron beam; therefore, they primarily convey a compositional, rather than

morphological, information: brighter areas in BSE imaging correspond to areas of larger average atomic weight.

- X-rays can be used to qualitatively identify the elements: this technique is called energy dispersive spectroscopy (EDX). The characteristic x-rays come from an even greater depth respect to SE and BSE, reaching several microns, so it's necessary to correctly interpret the results of the analysis, as they are related to a bigger volume portion

In this thesis, SEM overviews of the samples were obtained using a Quanta-200 apparatus (FEI-ThermoFisher Scientific, Eindhoven, The Netherlands), equipped with an INCA (Oxford Instruments Analytical, High Wycombe, UK) energy-dispersive X-ray (EDX) detector, whilst high-resolution observations were carried out with a Nova NanoSEM 450 (FEI-ThermoFisher Scientific) equipped with a field emission gun (FEG) electron source and a Quantax-200 (Bruker Nano Inc., Madison, WI, USA) EDX detector. Samples were sputter-coated with a thin (≈10 nm) gold layer to provide adequate conductivity.

Some cross-sectional samples for high-resolution imaging were further vibro-polished (VibroMet 2, Buehler, Lake Bluff, IL, USA) for 3 h using a 60 nm-size colloidal silica suspension (MasterPrep, Buehler). By removing any deformed surface layer through vibrating polishing, the electron channelling contrast in backscattered electrons (BSE) imaging mode was maximized to visualize the crystalline grain structure. Observations on these samples were carried out at low e-beam acceleration voltage (3 kV) without surface metallization.

Additional SEM observations and EDX maps were acquired using a Quanta-200 system (FEI – ThermoFisher Scientific) equipped with an INCA (Oxford Instruments Analytical, Oxford, UK) EDX detector, operating at 25 kV with a sputtered Au metallization layer.

The coating thickness was measured using image analysis software (ImageJ – NIH, Bethesda, Maryland, USA) on secondary electron SEM micrographs at 200x magnification. An example of the measurement can be seen in Figure 37. The same software was used to measure the coating porosity on optical micrograph at 500x magnification. Porosity was evaluated as the average of at four measurements on micrographs randomly acquired on the coating cross section.

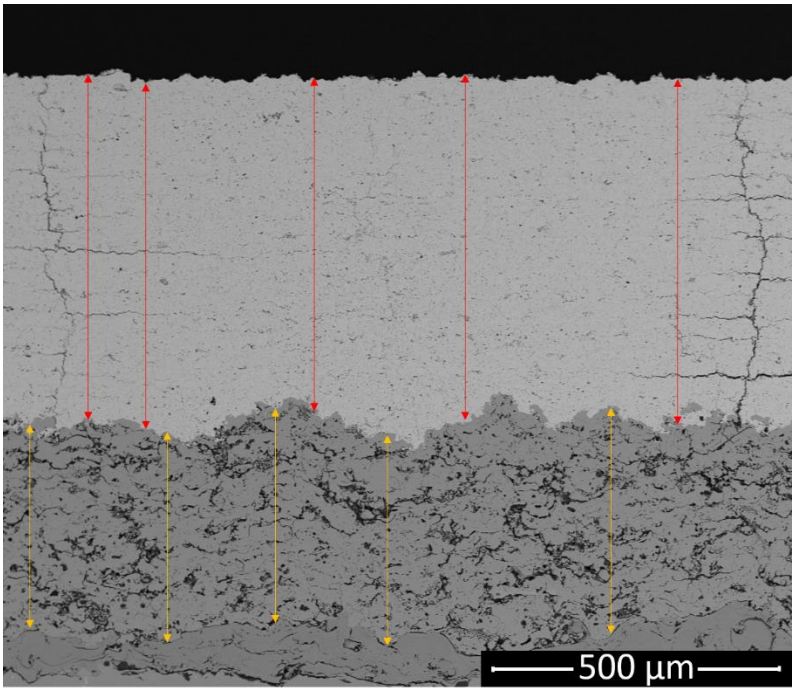

Figure 37 Example of measurement of the coating thickness

2.3.2.6 Electron Backscatter Diffraction

Some samples were employed for electron backscatter diffraction (EBSD) analysis. This technique provides quantitative microstructural information about the crystallographic nature of the materials [139]. It reveals grain size, grain boundary character, grain orientation and phase identity and distribution.

This characterization was carried out using the previously mentioned Nova NanoSEM 450 device, which was equipped with a QC-200 (Bruker) EBSD system featuring an e$^-$Flash1000 detector. Samples, placed at an inclination of 70° with respect to the electron beam axis, were scanned at 15 kV acceleration voltage under low-vacuum (40 Pa) conditions in order to avoid charging drift of their non-conductive surfaces.

2.3.2.7 Raman Spectroscopy

Raman spectroscopy is a spectroscopic technique used to observe vibrational, rotational, and other low-frequency modes of molecules [139]. It is based on inelastic scattering of monochromatic light, usually provided by a laser of visible light. Raman scattering is the consequence of energy absorption or release from the electron exited by the incident photon, which will consequently emit a scattered photon with a different energy and therefore a different

frequency. This wavelength shift (called Raman shift) is related to the specific energy levels of the molecule. It is therefore characteristic of the vibrational modes of the material, which depend on the interatomic forces, on the atomic mass, on bonding distances and angles. The spectrum is generally plotted in terms of wavenumber shift, i.e. of the difference between the incident wavenumber and the scattered wavenumber (the wavenumber being the inverse of the wavelength, typically measured in cm^{-1}). The spectra obtained by this method give information on the nature and structure of the compounds composing the sample. It is particularly useful to study both inorganic and organic materials, including minerals, powders, ceramic and organic coatings. In the present work micro-Raman spectra were acquired using a LabRam (Horiba Jobin-Yvon, Longjumeau, France) spectrometer equipped with a "red" He:Ne laser ($\lambda = 632.81$ nm) and a "green" solid-state laser ($\lambda = 532$ nm), both focused through a 100x objective.

3 Results and Discussion: Part I

Chapters 3 and 4 present the overall results of the present research. Each chapter contains the characterization of both feedstock powders and the corresponding coatings and the results are presented with the aim of highlighting the main differences among the coatings in terms of resistance to CMAS corrosion and thermal cycling. The first part of the thesis, shown in this chapter, is based on the paper "CMAS corrosion of YSZ thermal barrier coatings obtained by different thermal spray processes" published on *Journal of the European Ceramic Society* [135]. It concerns the study of 7YSZ coatings with different microstructures and obtained by different processes (APS porous, APS dense vertically cracked (DVC), SPS columnar-like), also examining the role of the chemical purity of the feedstock [135]. Indeed, little information is available on how the chemical purity of YSZ coatings affects their CMAS corrosion behaviour. Different YSZ feedstock materials (e.g. thermal spray powders) available on the market are indeed characterized by a diverse amount of impurities, including SiO_2, CaO, Al_2O3, Fe_2O_3, etc. [140,141]. Such impurities are known to promote high-temperature sintering of YSZ [141,142], which is an undesirable effect because a sintered TBC is stiffer and therefore has lower thermal cycling resistance [143]. As reviewed by Cao et al. [20], silica-based impurities tend to segregate along grain boundaries, a phenomenon which Helminiak et al. [143] did observe experimentally in APS YSZ coatings. Since CMAS attacks preferentially the grain boundaries of YSZ [82,144], it is reasonable to expect that silica-based impurities along those boundaries can be deleterious. This, however, has not been checked experimentally. In this regard, the purpose of this first part of the thesis is to provide more information regarding this important aspect.

3.1 Characterization of CMAS suspension for CMAS test

A preliminary DTA analysis was performed on the CMAS suspension used for CMAS attack, in order to identify the melting temperature of the mixture. The DTA curve of the CMAS mixture (Figure 38) exhibits a glass transition at Tg ≈ 740 °C. Upon further heating, an exothermic peak corresponding to a crystallization reaction occurs around Tx ≈ 1090 °C, immediately followed by an endothermic melting peak which begins at T < 1200 °C and reaches its maximum at Tm ≈ 1230 °C. It is therefore confirmed that the chosen test conditions (1 h at 1250 °C) are suitable to simulate corrosion by fully melted CMAS. Moreover, the observed Tg and Tm values are consistent with literature data for typical CMAS systems, corroborating the

suitability of the chosen composition as a simplified synthetic analogue to real CMAS-based deposits.

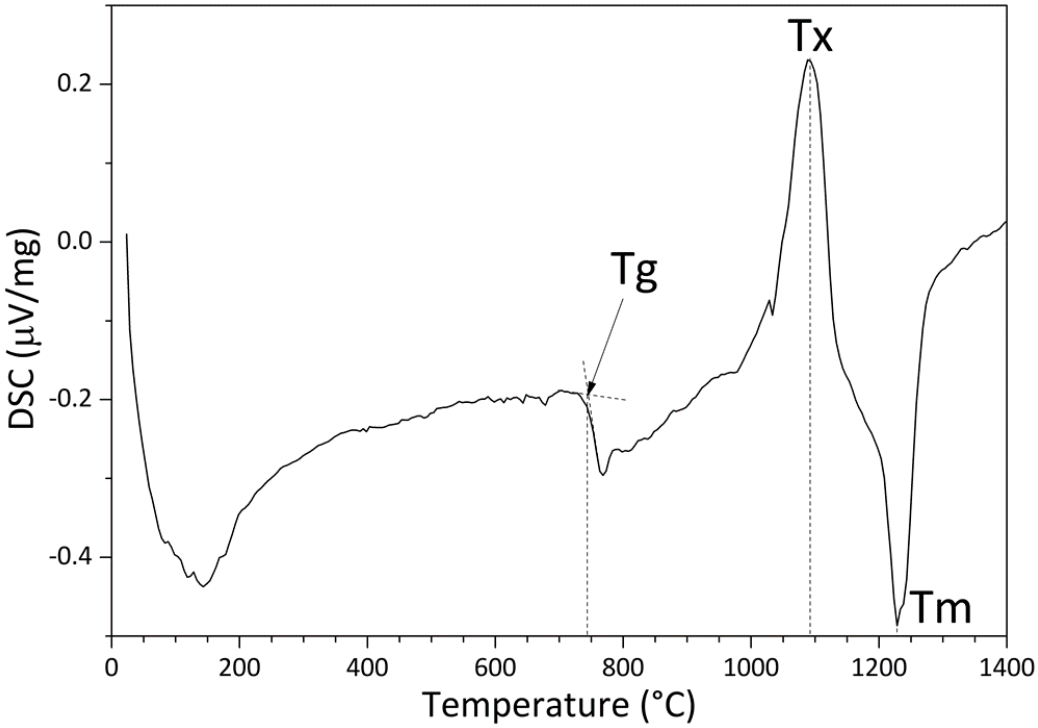

Figure 38 DTA curve of the synthesized CMAS [135]

3.2 CMAS corrosion behaviour of porous and DVC - APS coatings

SEM micrographs of as-sprayed coatings are reported in Figure 39.

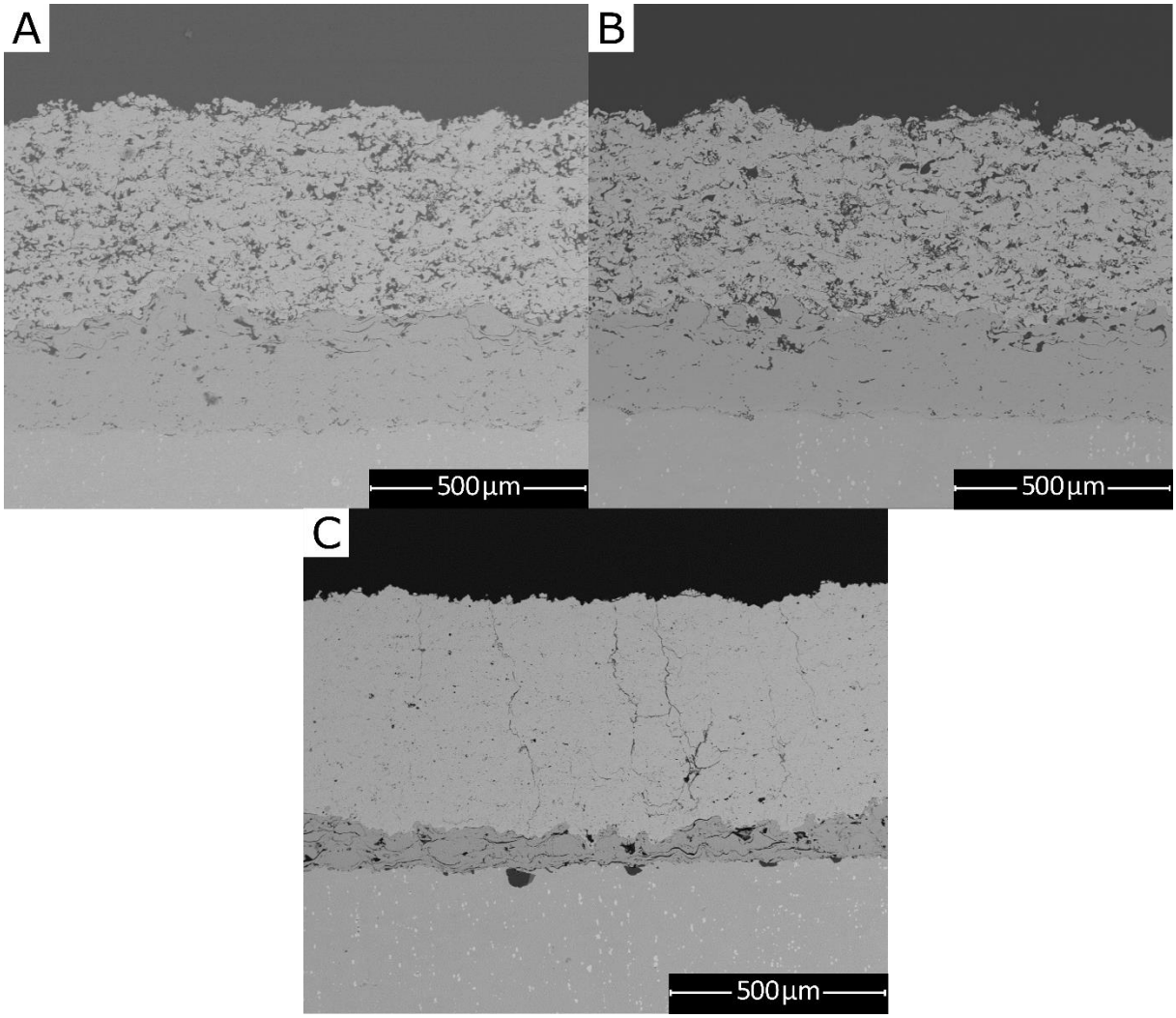

Figure 39 BSE-SEM micrographs of as-sprayed conventional APS TBCs with standard purity (A) and high purity (B), the APS – DVC coating (C)

TBC samples subject to an isothermal test at 1250 °C without CMAS deposit exhibit the typical microstructures resulting from the respective deposition processes (Figure 40). Although standard- and high-purity feedstock powders for conventional APS processing had different particle size distributions (Table 3), adjusted process parameters resulted in coatings with quite similar microstructures and porosity levels (Figure 40 A, B). In this way it is possible to ensure that any variation in the CMAS corrosion response of the two conventional APS coatings is

primarily due to the difference in chemical purity. The porosity and the thickness values of the coatings were measured through image analysis are reported in Table 7.

Table 7 Porosity and thickness values of porous and DVC-APS coatings

Sample	Porosity [%]	Thickness [µm]
Low purity APS coatings	14.2 ± 1.3	442 ± 16
High purity APS coatings	15.1 ± 1.9	391 ± 29
DVC coating	1.1 ± 0.3	582 ± 13

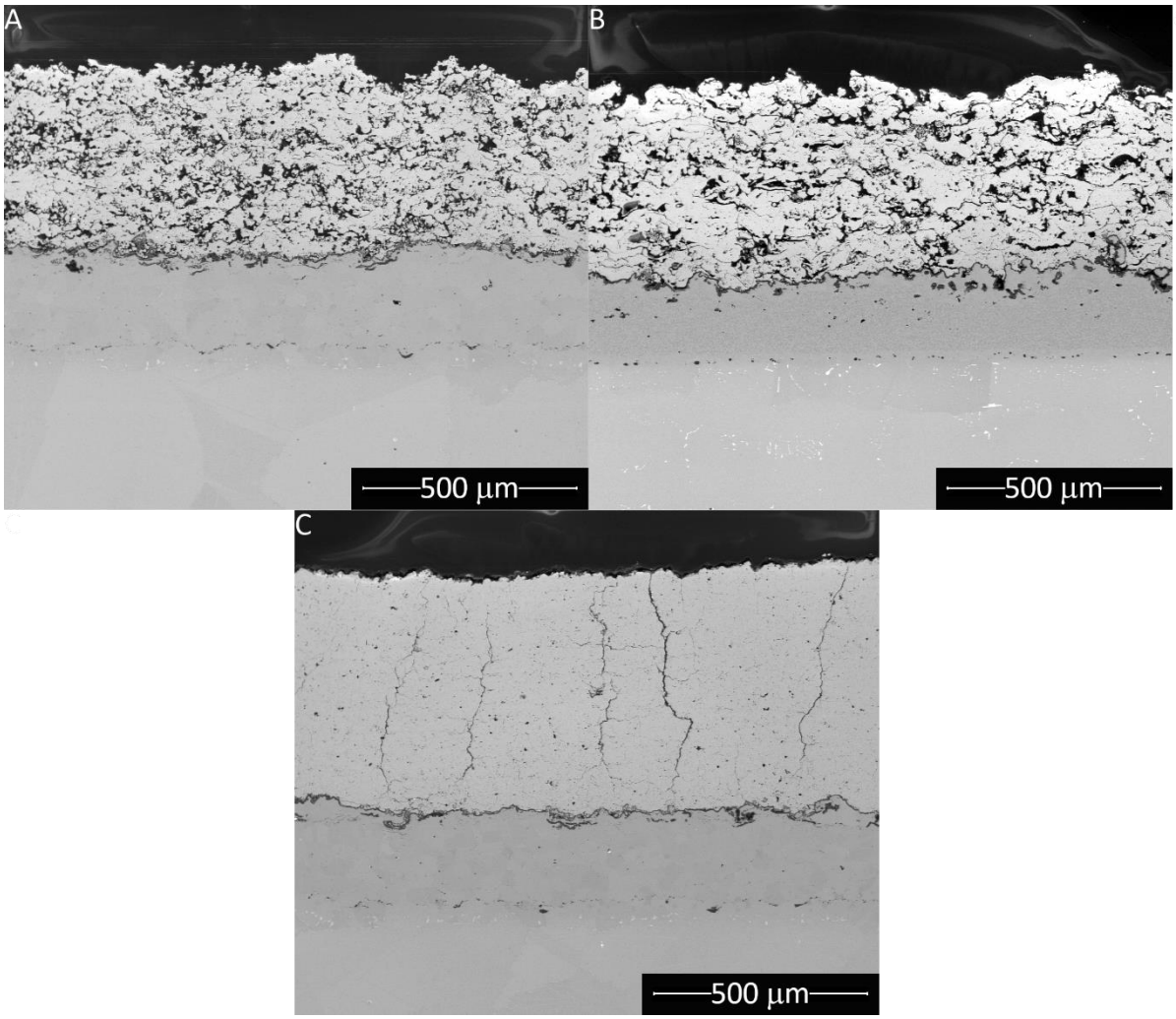

Figure 40 BSE-SEM overviews of conventional APS TBCs with standard purity (A) and high purity (B), the APS-DVC coating (C) after isothermal holding at 1250 °C for 1 h without CMAS [135]

After CMAS attack, some of the YSZ coatings were detached from the bond coat (Figure 41). This work was focused on the chemical interaction between CMAS and the ceramic top coats, thus corrosion along the YSZ/bond coat was not discussed in detail. According to [87,92,97], the CMAS melt infiltrates a YSZ coating in a matter of few minutes during an isothermal test at T > Tm. However, under actual service conditions, a temperature gradient exists across a TBC. CMAS experiences an increase in viscosity with decreasing temperature, until it crystallizes; therefore, its penetration stops somewhere across the thickness of the YSZ layer [89,106,145]. In this regard, it seems clear that an isothermal test can only give information concerning the chemical interaction between CMAS and the YSZ layer, whilst the top coat / bond coat interface is probably more affected than it would be in practice. A burner rig test in which a CMAS suspension is continuously injected into the flame can be the right tool to simulate the actual service situation and to mimic such behaviour [106,145].

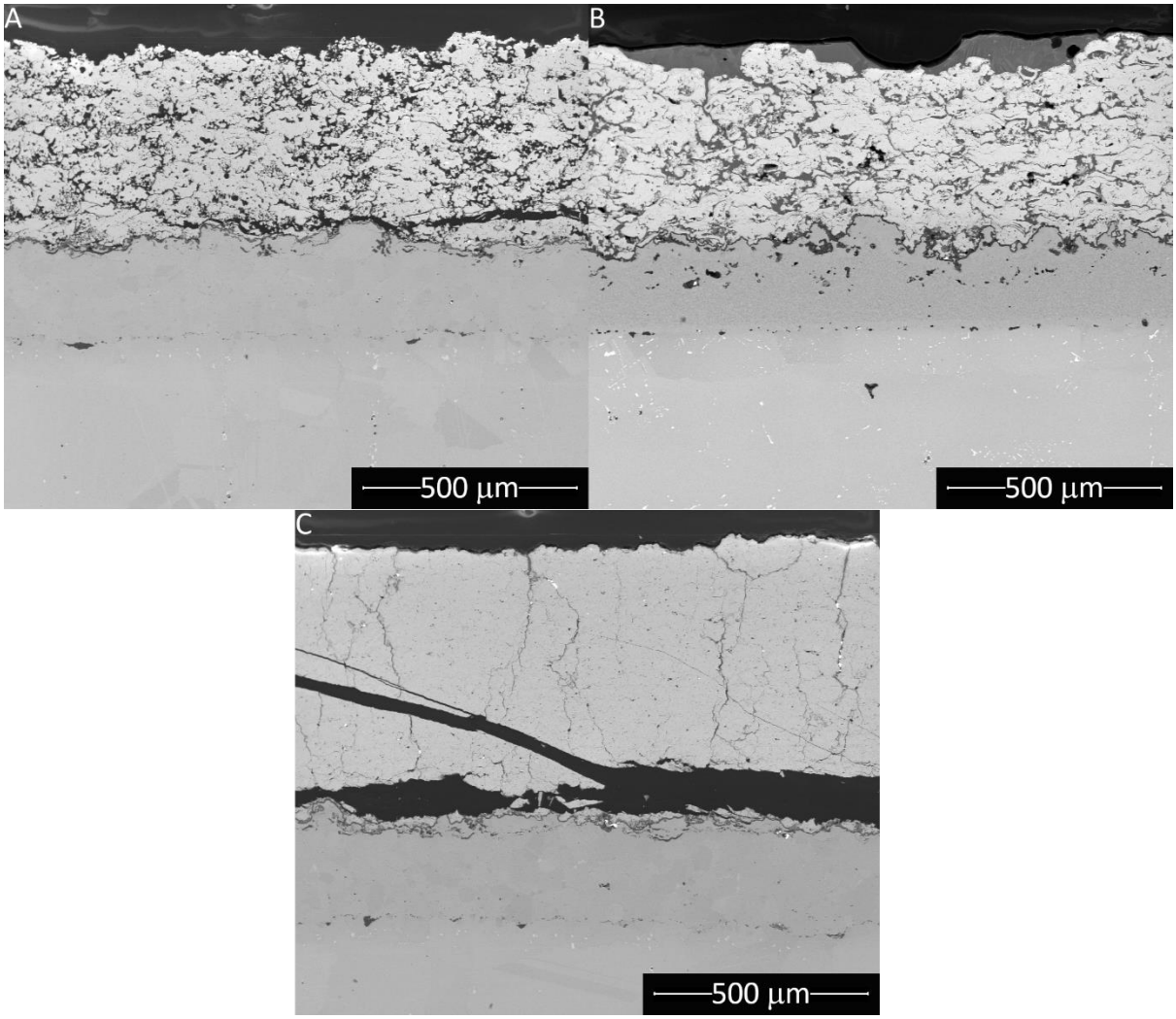

Figure 41 BSE-SEM micrographs of porous APS TBCs with standard purity (A) and high purity (B), the APS-DVC coating (C) after CMAS corrosion at 1250 °C for 1 h [135]

Not considering the interface region, low-magnification overviews of the conventional APS coatings (Figure 41A, B) would look similar to those of samples not infiltrated by CMAS (Figure 40A, B). By contrast, the main feature of the CMAS-corroded DVC sample is severe cracking, a likely consequence of "cold shock". Upon cooling, the CMAS-infiltrated ceramic layer is stiffened, and builds up large stresses, driving cracks parallel to the interface with the substrate. When imaged at high magnification, however, the coatings do reveal evident alterations in microstructure. CMAS attacked the boundaries between crystalline grains and separated them from one another (Figure 42B, D). This is in accordance with the finding by Mack et al. [145]. Before CMAS corrosion, conventional APS coatings (Figure 42A, C) exhibited three types of grain morphologies:

- Coarse equiaxed grains (label 1), which reflect unmelted particles;
- fine equiaxed grains (label 2), which originate from molten particles that solidify in-flight before reaching the substrate;
- fine columnar grains (label 3), which are typical of impact-quenched, molten lamellae.

Every grain type suffered attack by molten CMAS to a different degree. Dissolution took place along the boundaries of the coarser grains, which began to separate one from each other (Figure 42B, D). Fine-grained regions (labels 2 and 3), however, suffered an even more severe attack, because of their larger specific grain boundary area. This is particularly visible in standard purity coatings, where the corrosion proceeded so rapidly that it turned the finer grains into filament or globular structures (see arrows).

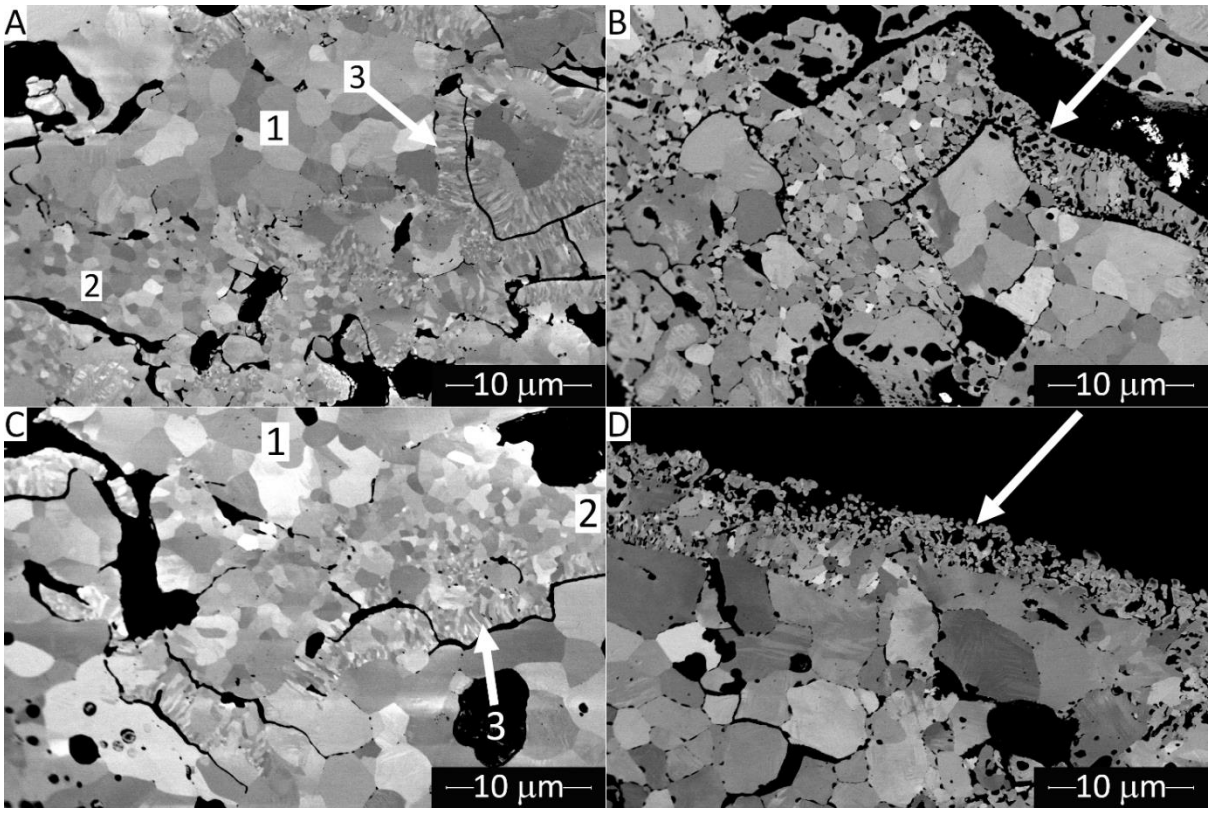

Figure 42 BSE-SEM micrographs of the conventional APS samples with standard purity (A, B) and high purity (C, D), after exposure at 1250 °C for 1 h without (A, C) and with (B, D) CMAS attack [135]

In particular, molten lamellae comprised of fine columnar grains are the most severely degraded type of microstructural feature. Degradation of molten lamellae is the cause of the loss of

structural integrity of the whole coating. Indeed, molten lamellae are the primary source of cohesion in a plasma-sprayed coating, and they basically keep unmolten or re-solidified particles in place. As a result, Figure 43A, C show that pores and defects are enlarged in the conventional, standard-purity APS coating, because the molten splats that were keeping the coating together have been attacked, so that the particles are almost left "afloat" in the CMAS melt. An extreme consequence of this phenomenon over prolonged corrosion times would be a buckling failure of APS TBCs (see Section 1.4.3) [94].

Grain morphology is, however, definitely not the only factor influencing the response of a YSZ TBC to attack by a CMAS melt. Chemical purity is also found to play a significant role, as shown by the comparison between two analogous APS YSZ layers obtained from feedstock powders with distinct impurity contents (Figure 42A, B vs. C, D; Figure 43A, C vs. D, F). The two coatings have quite similar microstructures and porosity levels (Figure 40A, B), including similar pristine grain structure, yet the extent of grain boundary dissolution is quite different. Specifically, the formation of globular/filament structures was mostly confined to the outer surface (near the original free-surface) of the high-purity coating (Figure 42D). A systematic comparison through intermediate- magnification micrographs (Figure 43A-C: standard purity; Figure 43D-F: high-purity) corroborates the idea that the microstructural integrity of the standard-purity coating has been more severely undermined. As molten CMAS penetrates massively into the standard-purity coating, not only through open pores but also through grain boundaries, it visibly separates the splats and the unmolten or re-solidified particles from one another. Globular/filament structures are widespread along all inner pore surfaces (Figure 43A-C: some of them are marked by arrows in panels B and C). Both the separation of splats and the formation of globular/filament structures along inner pore surfaces are less obvious in the high-purity sample (Figure 43D-F).

This means the presence of impurities, albeit in individual amounts ≤ 0.1 wt.% (Table 3), degrades the chemical stability of YSZ perceivably.

A possible explanation of the underlying mechanism is that, as explained at the beginning of this chapter, impurities could segregate at the grain boundaries, enhancing the grain-boundary dissolution rate. Such segregation was hypothesised in [20,143], albeit without direct evidence. Experimental studies on Y_2O_3- [146] as well as CeO_2-stabilized [147] ZrO_2 TBCs did confirm that silicates segregate along grain boundaries upon prolonged exposure at high temperature. They were detected by X-ray photoelectron spectroscopy (XPS) and Auger electron

spectroscopy (AES), and visualized by secondary ion mass spectroscopy (SIMS) imaging. Silicates would be readily dissolved by a silicate melt because of chemical affinity, thus accounting for enhanced grain-boundary dissolution.

Nonetheless, the YSZ coating in [146] was kept at high temperatures for 72 h in order to produce detectable segregation, i.e. much longer than it was done during the present corrosion tests. FEG-SEM (Figure 42A) analyses of uncorroded samples kept for 1 h at the test temperature of 1250 °C, indeed, did not reveal segregations of detectable size. SIMS imaging in [146], by contrast, showed segregations of micrometre size, which would have been readily caught in the present observations.

The role of segregations on the enhanced dissolution of grain boundaries in lower-purity YSZ should therefore be regarded as a hypothesis and such segregations, if any, have extremely small size, up to being undetectable by high-resolution scanning electron microscopy. In any case, using a high-purity YSZ material is preferable for turbines intended for operation in silicate-containing environments, though even pure YSZ is intrinsically reactive towards a CMAS melt. A sintered, pure YSZ bulk is indeed also attacked by a CMAS melt [148], again through grain-boundary dissolution until grains are separated from one another.

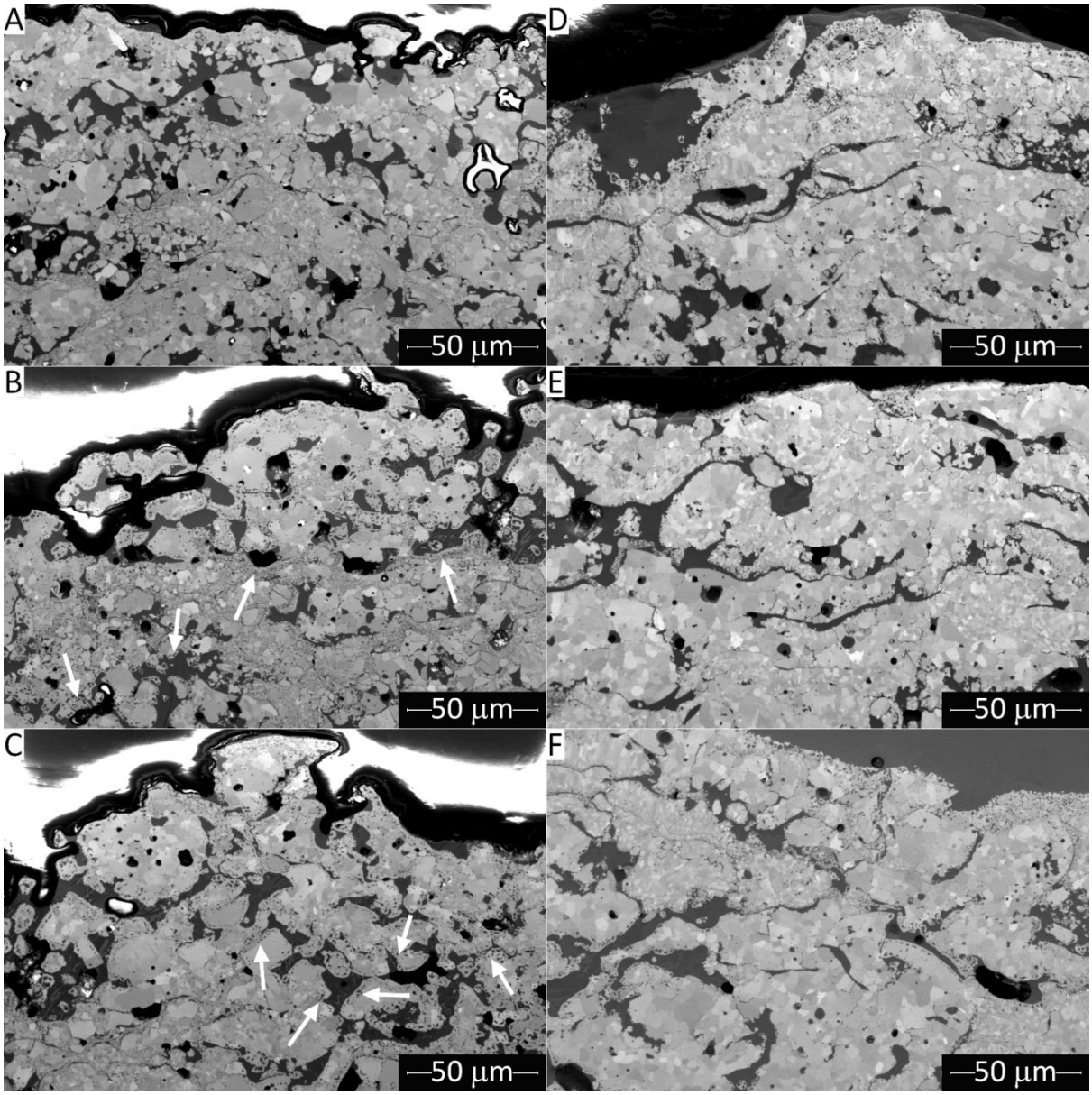

Figure 43 BSE-SEM micrographs showing a comparison between various regions near the surface of the conventional APS samples with standard purity (A-C) and high purity (D-F), after CMAS attack. Arrows in panels B and C indicate some instances of corrosion along inner pore surfaces [135]

Regarding DVC samples, they had to be imaged at greater magnification than the conventional ones (Figure 44) to properly discern their grain structure. Differently from porous APS coatings, they contain a larger fraction of columnar grains (Figure 44E). These columnar grains might be a bit larger (0.9 ± 0.3 µm) than are the corresponding ones in the APS samples (0.4 ± 0.1 µm), because the higher surface temperatures needed to produce a DVC sample might result in higher grain growth rate compared to the heterogeneous nucleation rate. However, most of the DVC

sample is made of these columnar grains, because it mostly consists of molten lamellae. By contrast, as noted previously, only a small fraction of the APS samples consists of molten lamellae with columnar grains, because many unmolten or re-solidified particles develop a coarser, equiaxed grain structure. After CMAS attack, columnar grains in DVC coatings are less separated from one to another than the conventional APS coatings. This is probably due to the presence of dense "islands" which do not offer an easy access to the molten CMAS penetration (Figure 44F). However, some corrosion along the grain boundaries did occur (compare Figure 44F to Figure 44E). Probably, CMAS did not penetrate only through the few pores existing in the "islands", but it also made its own way through the grain boundaries themselves. The large specific surface of the grain boundaries in the DVC sample might have helped this attack in spite of the high density of the "islands".

The most negative effect of CMAS attack onto the DVC coating, in any case, was the penetration of the glass melt inside the segmentation macro-cracks. The main source of compliance of this coating, the segmentation cracks, was thus frustrated by solidification of the infiltrated CMAS during cooling. This led to the build-up of stresses due to thermal expansion mismatch with the substrate and bond coat.

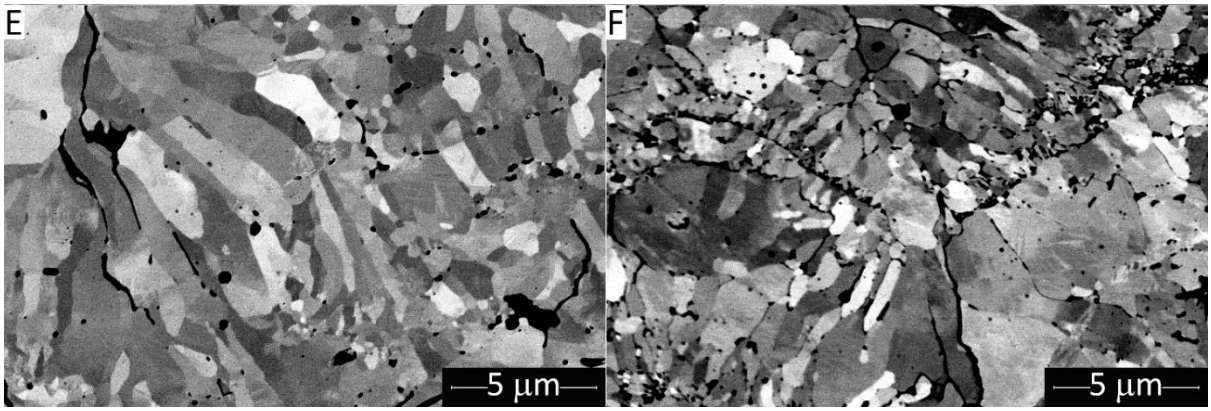

Figure 44. APS-DVC samples after exposure at 1250 °C for 1 h without (E) and with (F) CMAS [135]

In both porous APS and DVC APS coatings, the globular/fibrous structures are interpreted as the product of a dissolution and precipitation process. The CMAS melt dissolved the original YSZ grains starting from their boundary and proceeding toward the interior. When enough ZrO_2 had been dissolved, its local concentration became high enough to cause its precipitation into

these peculiar structures. CMAS remained within the fine pores, as revealed by the detection of EDX peaks belonging to Si, Al, Mg and Ca (e.g. see Spectrum 1 in Figure 45C).

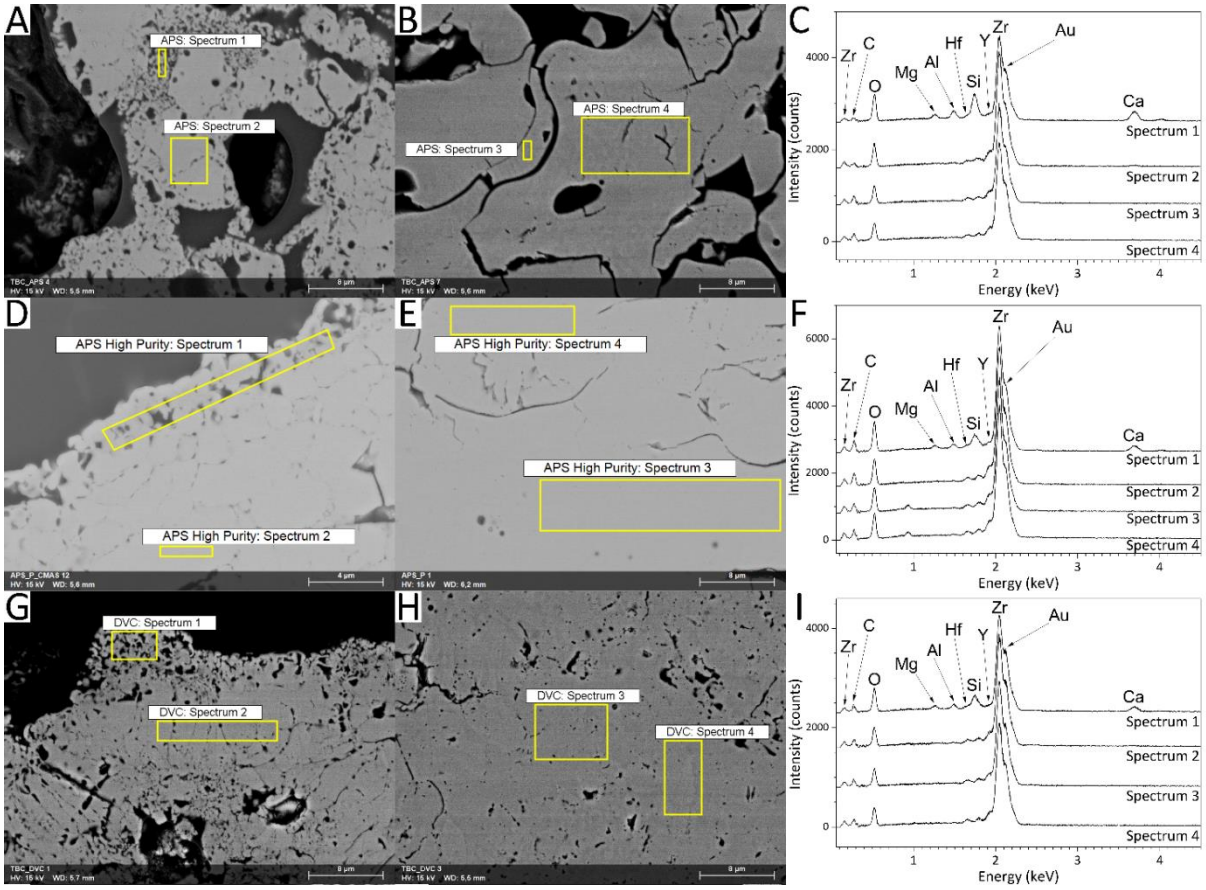

Figure 45 BSE-SEM micrographs (A, B, D, E, G, H) and corresponding EDX spectra (C, F, I) acquired on standard-purity conventional APS (A-C), high-purity conventional APS (D-F) and APS-DVC (G-I), exposed (A, D, G) and not exposed (B, E, H) to the CMAS melt [135]

Quantitative EDX analyses in Table 8 are acquired on different areas of the corroded samples with the same microstructural features (e.g. globular areas such as Spectra 1 in Figure 45A, D, G; internal areas such as Spectra 2 in Figure 45A, D, G; un-corroded areas such as Spectra 3 and 4 in Figure 45B, E, H) in order to provide a sound overview of the distribution of Y_2O_3 concentration relative to ZrO_2 concentration. Quantitative EDX analyses (Table 8) show that globular/filament regions exhibit a relatively low yttria/zirconia mass ratio, often ≤ 6%. This is true for both the porous APS samples (Figure 45A, C: spectrum 1; Figure 45D, F: spectrum 1). As a reference, the pristine coatings (Figure 45B, C: spectra 3, 4; Figure 45E, F: spectra 3, 4) exhibit a Y_2O_3/ZrO_2 mass ratio of approx. 10%. This is slightly in excess of the nominally

expected values (≈ 8-9% as inferred from chemical analyses in Table 3). The discrepancy is probably not much relevant, because it might follow from the limited accuracy of the EDX technique, and from additional quantification errors caused by partial overlapping of the L-lines Y and Zr. On the top surface of the DVC coating (Figure 45G, I), as well as along the segmentation cracks, the more extensive contact with CMAS caused the same dissolution and re-precipitation phenomenon described previously. Yttria-lean porous regions are developed (Figure 45G, I: spectrum 1 and Table 8: spectrum 1), identical to the ones seen in porous APS coatings.

Table 8 Percent ratio between the mass fractions of Y_2O_3 and ZrO_2 as determined by quantitative analyses on the EDX spectra in Figure 45 [135]

Sample	*Spectrum 1 (globular areas)*	*Spectrum 2 (internal areas)*	*Spectrum 3 and spectrum 4 (un-corroded areas)*
Conventional APS, standard purity (Figure 45A-C)	5.3 ± 0.1	10.0 ± 0.2	10.0 ± 0.6
Conventional APS, high purity (Figure 45D-F)	4.4 ± 0.2	11.1 ± 0.4	10.4 ± 0.1
APS – DVC (Figure 45G-I)	3.6 ± 0.1	9.3 ± 0.1	9.5 ± 0.5

The zirconia-yttria phase diagram published by Scott et al. and reported in Figure 9 (Section 1.2.3) shows that a Y_2O_3/ZrO_2 ratio ≤ 5 wt.% is too low to develop non-transformable *t'*-YSZ. Specifically, this composition falls within the stability region of *tetragonal* phase at high temperature, whilst it is expected to convert mostly to *monoclinic* phase at room temperature. Accordingly, micro-Raman spectra acquired on the globular regions contain the characteristic peaks of monoclinic zirconia, with variable intensity (Figure 46). In detail, peaks belonging to monoclinic phase occur in almost all the micro-Raman spectra acquired on outer (area near the original surface) and inner (internal area within the coating) surfaces of the standard-purity, porous APS coating (Figure 46), though most of them possess very low intensity. In Figure 46, only spectrum 5 does not show any *m*-phase signal. In contrast, the monoclinic phase was clearly identified in spectra acquired on the top surface of the high-purity sample (Figure 47: spectra 2 and 4). Other spectra, including those near internal surfaces (Figure 47: spectrum 5), do not show any monoclinic peak and the same is true of the DVC sample. The high-purity and

DVC samples are therefore confirmed to have experienced a lower overall degree of grain-boundary dissolution. The main Raman peak of the cubic phase is overlapped by signal from the monoclinic and tetragonal phases; hence, it is not possible to assess whether any cubic phase exists, although, it is probably in very low amount (if any). Note that at least part of the Raman signal from tetragonal zirconia in these spectra might come from nearby, non-dissolved YSZ regions that retained their original composition. Micro-Raman signal comes from a region at least 2 μm wide, i.e. larger than each individual globular or filament structure.

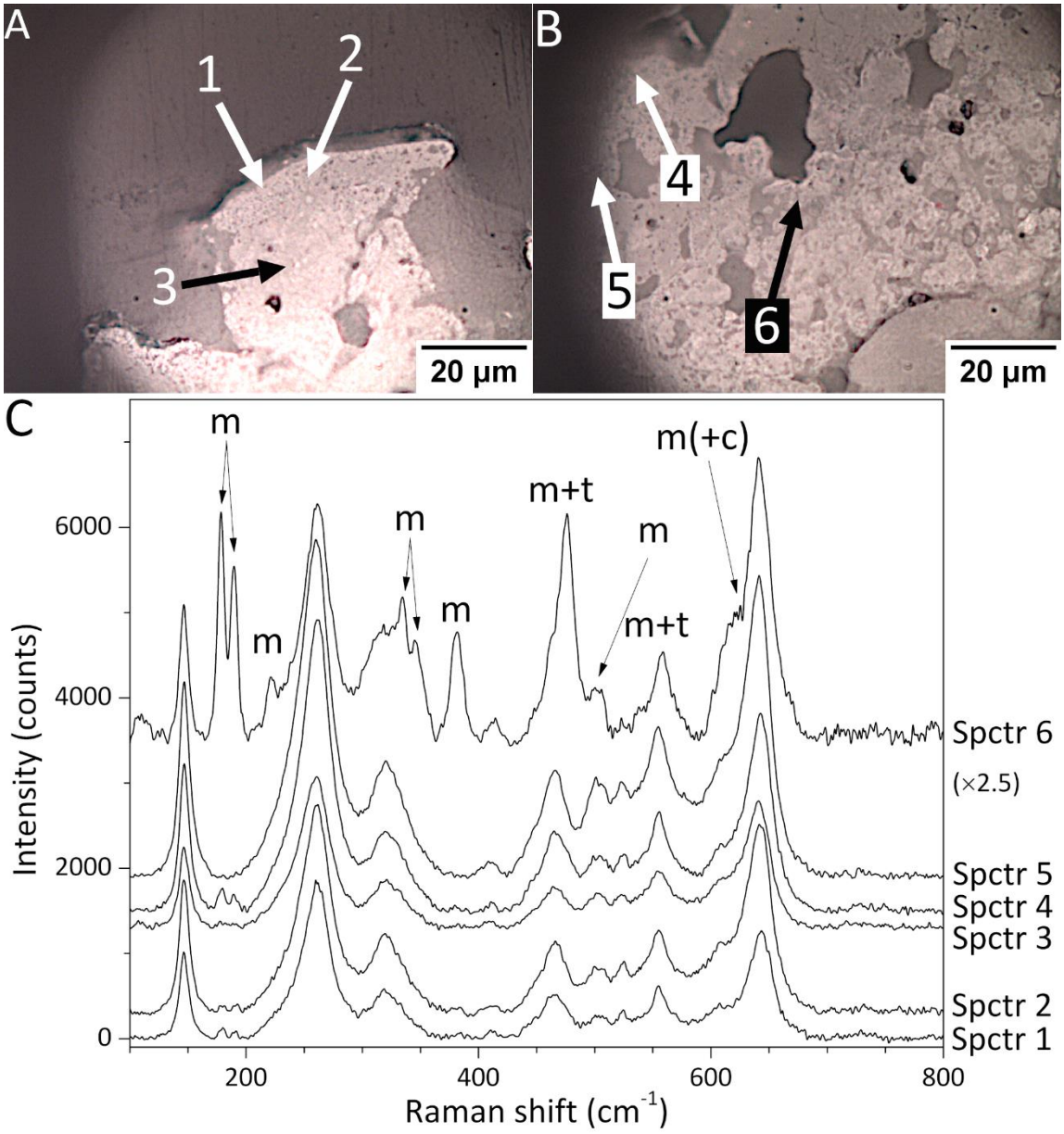

Figure 46 Optical micrographs of the standard-purity, conventional APS coating after CMAS corrosion (A, B), and corresponding micro-Raman spectra (C). Labels m, c, t indicate peaks assigned to monoclinic, cubic and tetragonal zirconia polymorphs, respectively. All unmarked peaks belong exclusively to tetragonal zirconia [135]

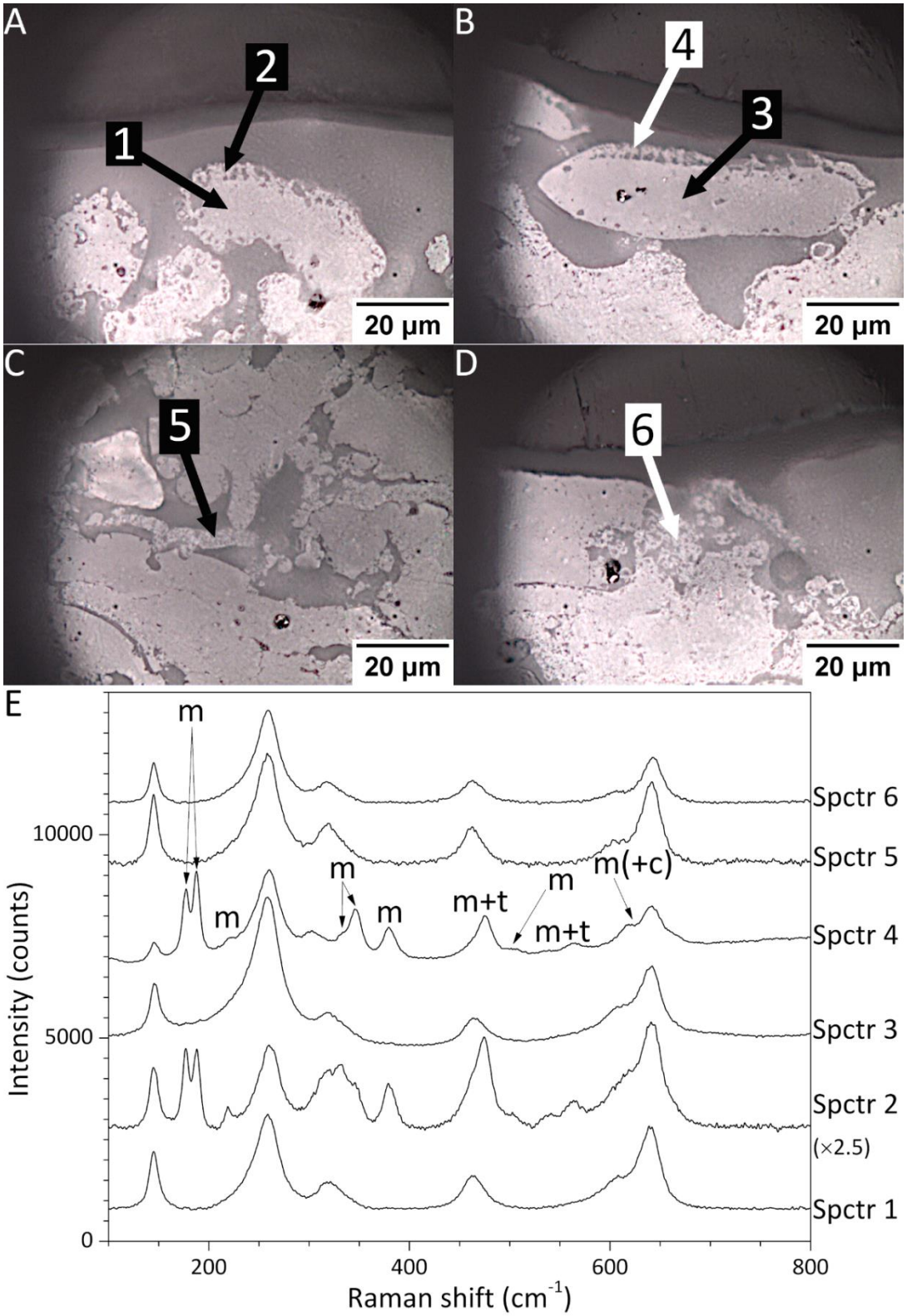

Figure 47 Optical micrographs of the high-purity, conventional APS coating after CMAS corrosion (A-D), and corresponding micro-Raman spectra (E). Labels m, c, t indicate peaks assigned to monoclinic, cubic and tetragonal zirconia polymorphs, respectively. All unmarked peaks belong exclusively to tetragonal zirconia [135]

Through electron channelling contrast, magnified BSE-SEM views of the globular/filament structures reveal numerous “striations” both in porous APS and in DVC samples (Figure 48). These are interpreted as the outcome of a martensitic $t \rightarrow m$ transformation during cooling. Some of the largest globular grains exhibit a martensitic shell (Figure 48A,B - label 1) that surrounds a core with no striations (Figure 48A, B - label 2). The latter probably corresponds to an original *t'*-YSZ grain, so severely attacked along its boundary that it was left “afloat” in the CMAS melt. Yttria-lean zirconia precipitated around its boundary and experienced martensitic transformation upon cooling. Core-shell grains contribute to explaining why Raman signal from the tetragonal phase is still discernible in the porous areas, although the precipitated zirconia is almost entirely monoclinic at room temperature.

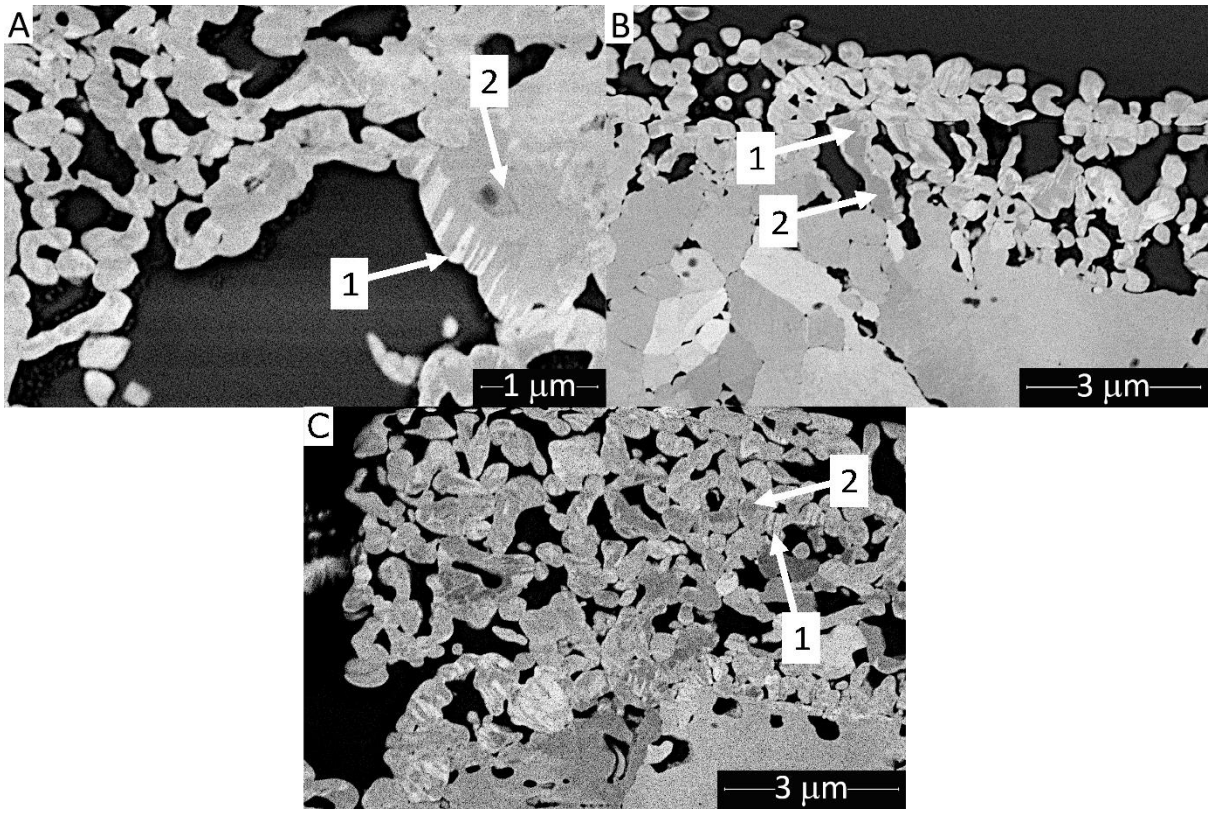

Figure 48 BSE-SEM micrographs showing the detailed grain structure of microporous regions found inside the standard-purity, conventional APS coating (A), on the surface of the high-purity conventional APS coating (B) and the APS-DVC coating (C). Label 1 = martensitic “striations”; label 2 = core [135]

EBSD maps confirm that, after CMAS attack, numerous ring structures (Figure 49A - see red arrows) on the outer surface of the APS coating with standard purity consist entirely of *m*-phase, or of *m*-phase precipitating around some residual *t'* phase (Figure 49A, some of the monoclinic areas are highlighted by circles). The porosity of the surface region was infiltrated by glass: all of these pores, as well as their boundaries with the crystalline zirconia regions, are sources of noise in the EBSD signal. Therefore, scattered pixels identified as *m*-ZrO_2 within the pores are likely just noise. Indeed, pattern quality is poor in those pixels. However, larger *m*-ZrO_2 areas (including the encircled ones) produce good quality patterns and are confidently identified as actual precipitations. A detailed orientation map acquired on a sufficiently large *m*-phase area shows that it consists of two main twin variants with alternate crystallographic orientations (Figure 49B-C). The stereographic projection in Figure 49D indeed shows that most of the striations have only two alternate, specular orientations, which is indicative of the presence of two twin variants. It is thus confirmed that "striations" seen through electron channelling are, in fact, twin martensite variants, which is the typical outcome of a martensitic transformation [111] occurring along a specific habit plane of a pristine *t* grain. All of these observations match with transmission electron microscopy analyses by S. Krämer et al [98]. Taking advantage of the broader field of view of the present SEM micrographs, it can therefore be more confidently concluded that the formation of twin martensite variants during $t \rightarrow m$ transformation is a general feature of precipitated zirconia produced during CMAS attack.

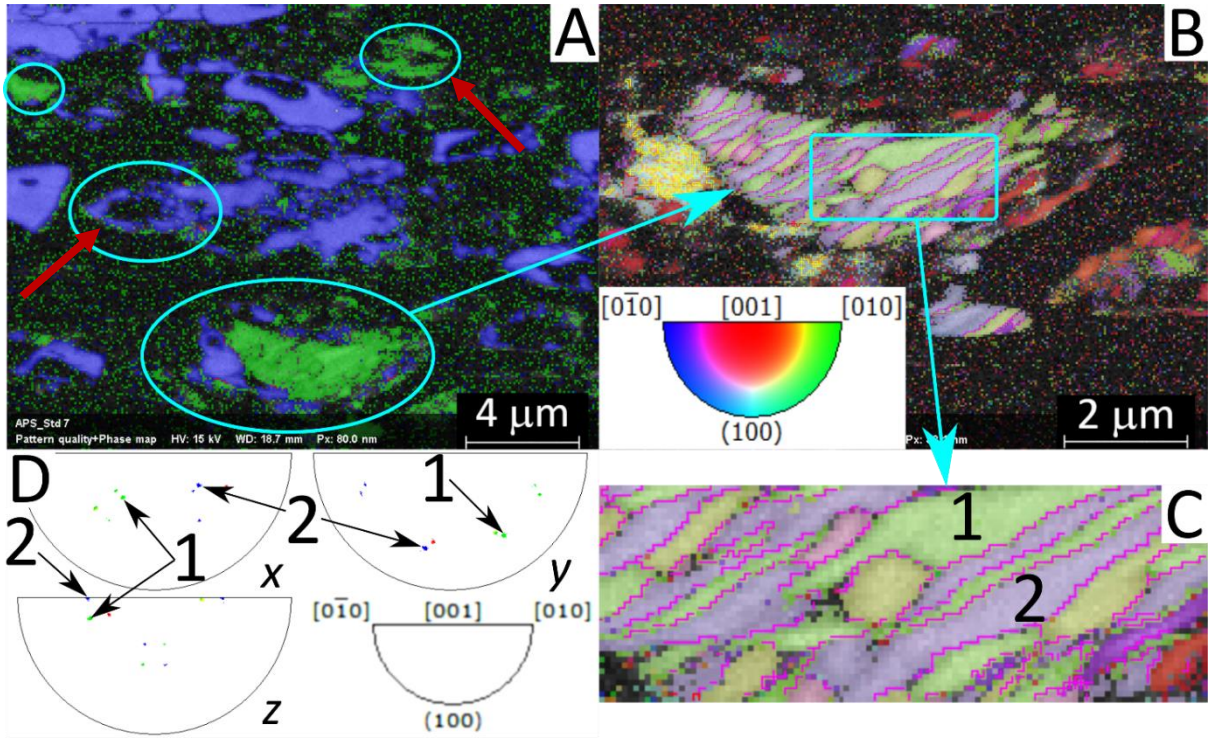

Figure 49 EBSD mapping of the near-surface region in the standard-purity APS coating after CMAS attack. (A) Phase map (blue = t'–YSZ, green = m-ZrO_2); (B) inverse pole figure along the y-direction (IPFY) of a predominantly m-ZrO_2 precipitation, with (C) digital magnification of the same; and (D) stereographic projections showing grain orientations in the zoomed area. Labels 1 and 2 indicate twin martensitic variants with alternate orientations [135]

Below the surface, the corroded sample consists mainly of t'-phase with various degrees of grain-boundary dissolution (Figure 50A, B). Few m-ZrO_2 grains, however, occasionally appear where corrosion was the most severe (see arrows). This is consistent with Raman spectra showing small amounts of monoclinic phase throughout the coating thickness. As a term of comparison, the portion of the sample not exposed to molten CMAS does not show either grain-boundary degradation or m-phase formation (Figure 50C, D). The different grain morphologies (coarse equiaxed, fine equiaxed and fine columnar) identified by electron channelling contrast are also confirmed by EBDS maps (Figure 50C, D).

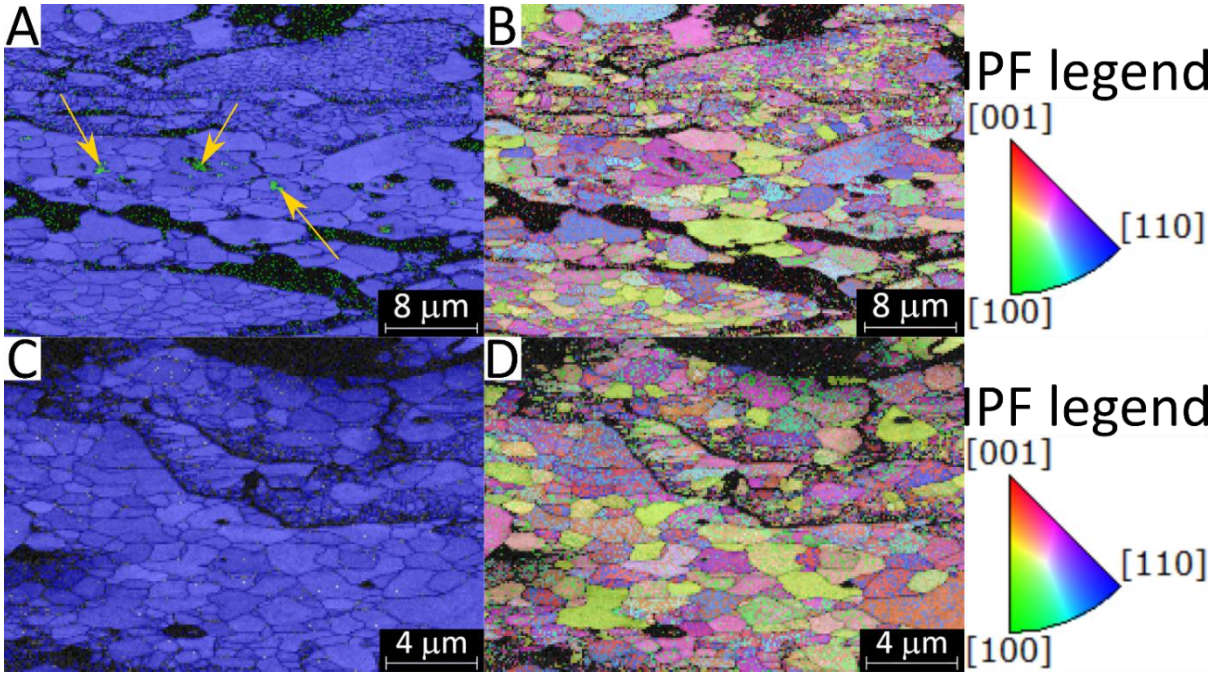

Figure 50 EBSD mapping of a mid-thickness region in the standard-purity APS coating, after isothermal holding with CMAS attack (A, B) and without CMAS (C, D). (A, C) Phase maps (blue = t'–YSZ, green = m-ZrO_2) and (B, D) corresponding inverse pole figures along the x-direction (IPFX) [135]

Precipitations of monoclinic zirconia also occur on the outer surface of the high-purity APS coating, consistent with all previous considerations (Figure 51E, F). Both ring structures (circle) and m-phase shells around t'-cores (arrows) are seen. At a mid-thickness location (Figure 51C, D), to the contrary, very little m-phase appears (arrows), once again consistent with Raman spectroscopy results. Some grain-boundary attack did, nonetheless, occur, as confirmed by comparing to a non-corroded region of the same sample (Figure 51A, B): grains start separating from one another (Figure 51C: circle). Voids appear between distinct grains, together with minor amounts of m-phase as noted above.

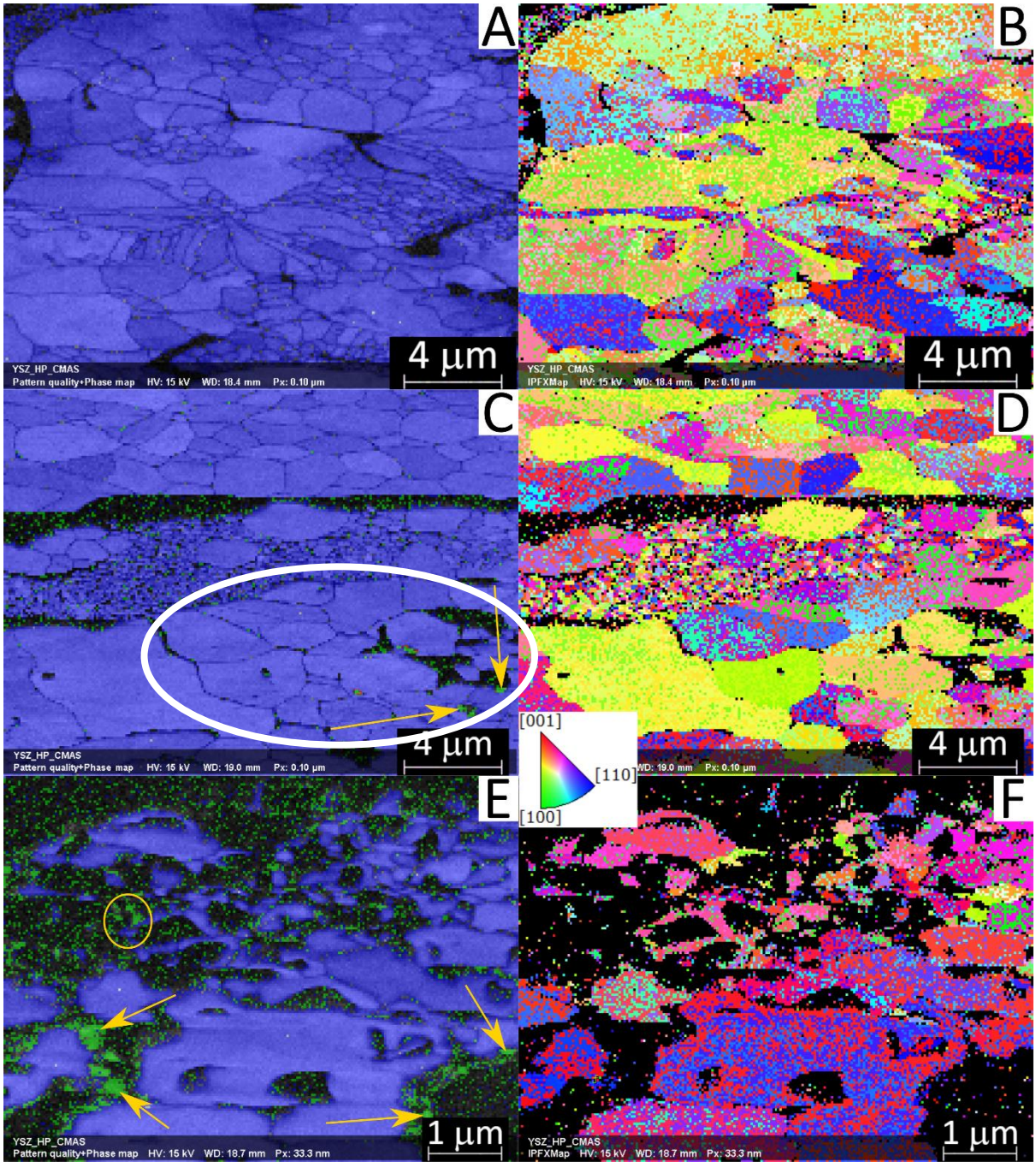

Figure 51 EBSD mapping of the high-purity APS coating after isothermal holding: mid-thickness region without (A, B) and with (C, D) CMAS attack, and near-surface region with CMAS attack (E, F). Phase maps (A, C, E: blue = t'–YSZ, green = m-ZrO_2) and corresponding inverse pole figures along the x-direction (IPFX - B, D, F) [135]

3.3 CMAS corrosion behaviour of the SPS coating

SEM micrographs of as-sprayed SPS coatings acquired at different magnifications are reported in Figure 52.

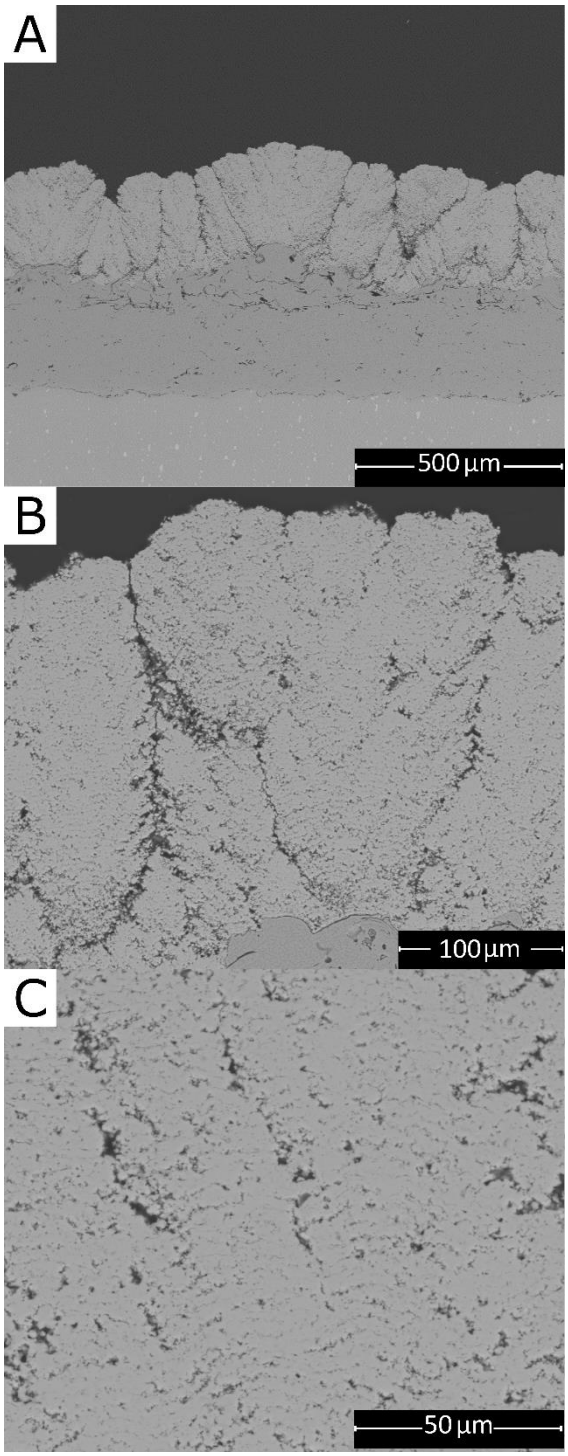

Figure 52 BSE micrographs of as-sprayed SPS coatings acquired at 200x (A); 800x (B); 2000x (C)

The SPS coating with a thickness of 298 ± 10 µm, is the one which shows the largest changes compared to as-sprayed coatings after CMAS exposure (Figure 53B). In this case, the coating structure was compromised by the CMAS attack. As observed in Figure 53B, frothing occurs in the SPS coating during CMAS attack. Although the SPS YSZ layer itself was infiltrated by CMAS, the layer was not affected to the point to cause frothing inside the TBC itself. The frothing was confined to the silicate layer on top of the coating (Figure 53B - see arrows).

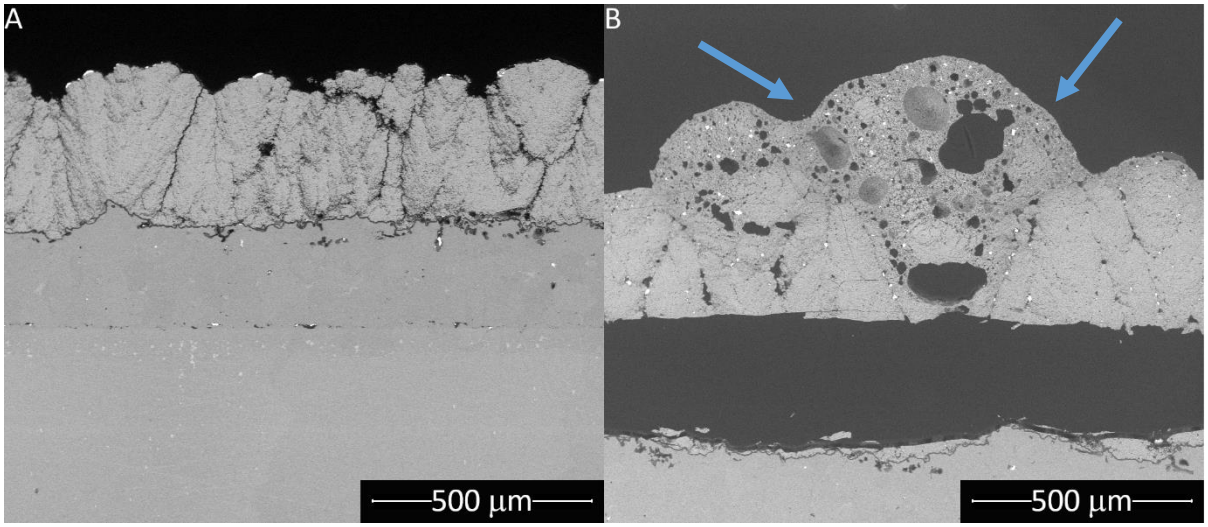

Figure 53 BSE-SEM overviews of the SPS coating after isothermal holding at 1250 °C for 1 h without (A) and with CMAS (B) [135]

There is a significant difference between the columnar SPS and DVC microstructures, although both have columnar architecture.

The molten CMAS penetration into SPS coatings is facilitated because of there are more inter-columnar gaps per unit length than in the DVC coating. The intra-columnar material is also much more porous than the DVC "islands" seen in Figure 42E. The overall porosity measured in the SPS coating is ≈ 25%. SPS coatings are built up by dense but very thin layers separated by fine interlayer porosity (Figure 54A-C: arrows in panel B indicate interlayer porosity). This type of microstructure is due to the particle size used in the SPS process. The suspension contains finer powders than the dry APS powders, as reported in Table 3. Particles were heated and accelerated into the plasma plume, reaching the metallic substrate in the molten state and with high velocity. As result, the coating is built up by very fine lamellae attached so tightly to

one another that they become almost undistinguishable. This produces dense layers. However, interlayer porosity is generated by particles that do not enter the plasma plume. These particles are slower and colder, and they stick loosely on top of each layer without flattening. Within each layer, columnar grains (Figure 54C) are smaller than they are in the DVC "islands" (Figure 42C), which is also consistent with the smaller size of the lamellae. The columnar grains sometimes seem to extend across more than one lamella, possibly reflecting epitaxial growth across a very tight interface.

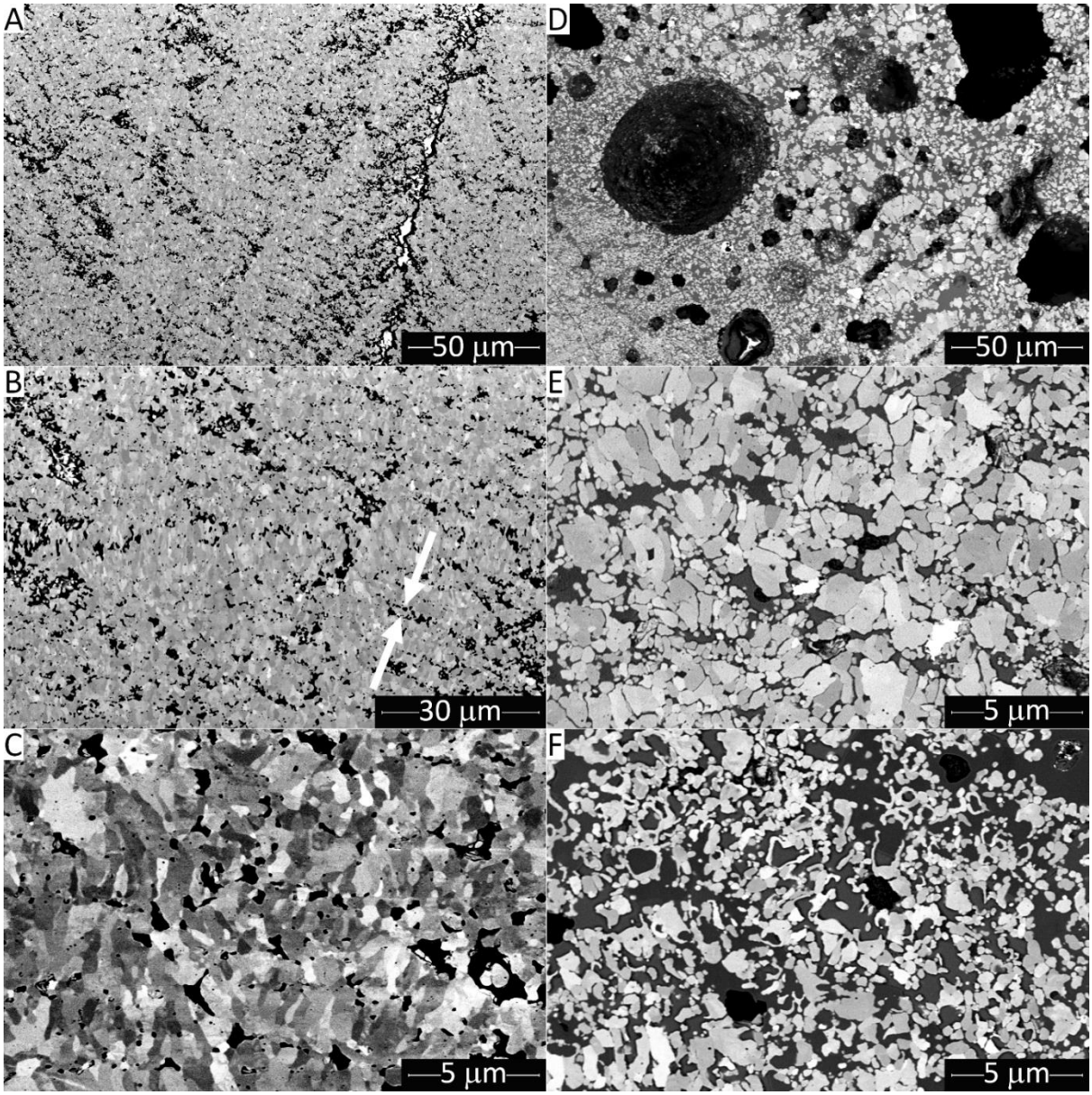

Figure 54 BSE – SEM micrographs of the SPS coatings after exposure at 1250 °C for 1 h without (A-C) and with (D-F) CMAS attack [135]

As described in the Introduction, the widespread intra-columnar porosity of the SPS coatings is usually regarded as an advantageous feature because it allows to obtain a coating with low thermal conductivity and it imparts high strain tolerance. On the contrary, the present result shows that the inter-columnar gaps and intra-columnar porosity are an issue in terms of CMAS resistance because they permit a rapid ingression of molten CMAS into the coating. For this reason, CMAS penetration into the intra-columnar region of SPS coating is easier compared to the DVC islands. The large specific surface area of the boundaries between the particularly fine grains then allows for an extensive attack. As a result, the grains become separated from one another and are free to move in the CMAS melt (Figure 54E).

The mechanical integrity of the coating is completely lost, and viscous flow allows the air pockets formerly contained within the pores of the SPS coating to coalesce and expand. The outcome is frothing as seen in Figure 54D. In the upper part of the coating the corrosive attack is so widespread that YSZ grains go adrift in the viscous glass and dissolve extensively.

Globular and fibrous structures therefore precipitate in large amounts (Figure 54F). Their microstructural details again reveal the martensitic “striations” (Figure 55) described previously, and their fine pores are filled with CMAS, as revealed by the detection of EDX peaks belonging to Si, Al, Mg, and Ca. The quantitative EDX analysis acquired in correspondence of the globular regions exhibit a yttria/zirconia ratio of 3.7 (Table 9), indicating non-stabilized zirconia, similar to the case of APS and DVC coatings, and micro-Raman spectra also reveal that monoclinic zirconia appears in the upper part of the sample (Figure 57: spectra 3 and 4) where the globular/filament regions are identified by SEM.

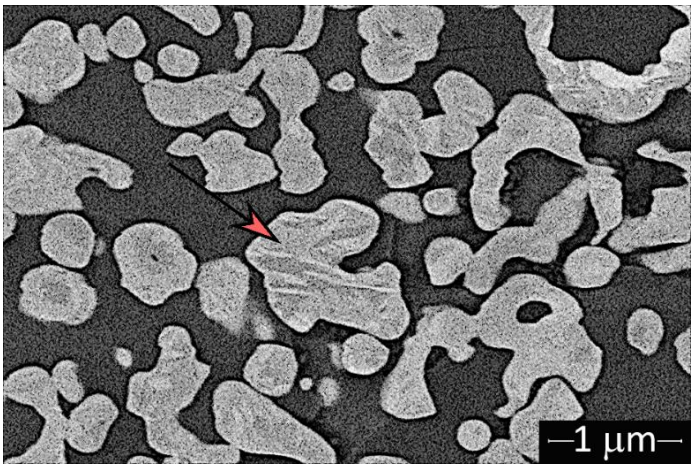

Figure 55 Martensitic striations identified in SPS YSZ sample [135]

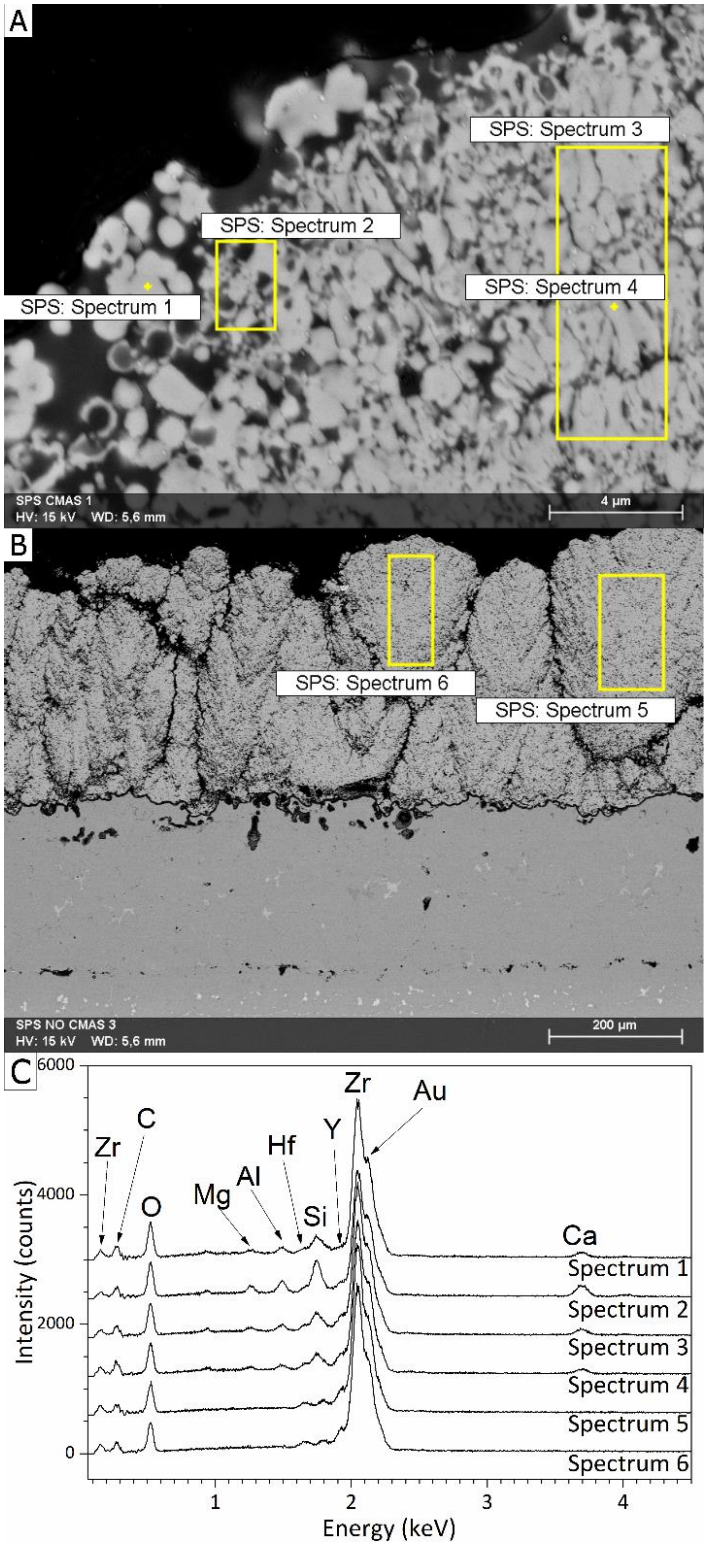

Figure 56 BSE –SEM micrograph and corresponding EDX spectra acquired on SPS coatings exposed (A) and not exposed (B) to the CMAS melt [135]

Table 9 Percent ratio between the mass fractions of Y_2O_3 and ZrO_2 as determinate by quantitative analysis on the EDX spectra in Figure 56 [135]

SPS Figure 56 ***(A-C)***	*Spectrum 1*	*Spectrum 2*	*Spectrum 3*	*Spectrum 4*	*Spectrum 5*	*Spectrum 6*
	3.7	7.9	9.8	10.1	10.4	10.4

Interior areas where grain-boundary separation occurred without formation of globular/filament morphologies, to the contrary, do not exhibit measurable alterations of the yttria/zirconia ratio, compared to the pristine coating (Figure 56: spectra 3, 4). In those areas, only tetragonal zirconia is identified (Figure 57: spectra 1 and 2), although CMAS attack is so extensive that even the optical micrographs (Figure 57A, B) do show that YSZ grains are separated by molten CMAS.

Overall, it is concluded that, in spite of its high chemical purity, the described SPS YSZ coating is unfit for operation in environments where low-melting silicate dust can be ingested into a turbine. The high density of inter-columnar gaps, the abundant intra-columnar porosity, and the extremely fine grain structure are all disadvantageous in this respect. SPS YSZ therefore needs suitable protection through a top layer that should prevent, as much as possible, any infiltration by the CMAS melt.

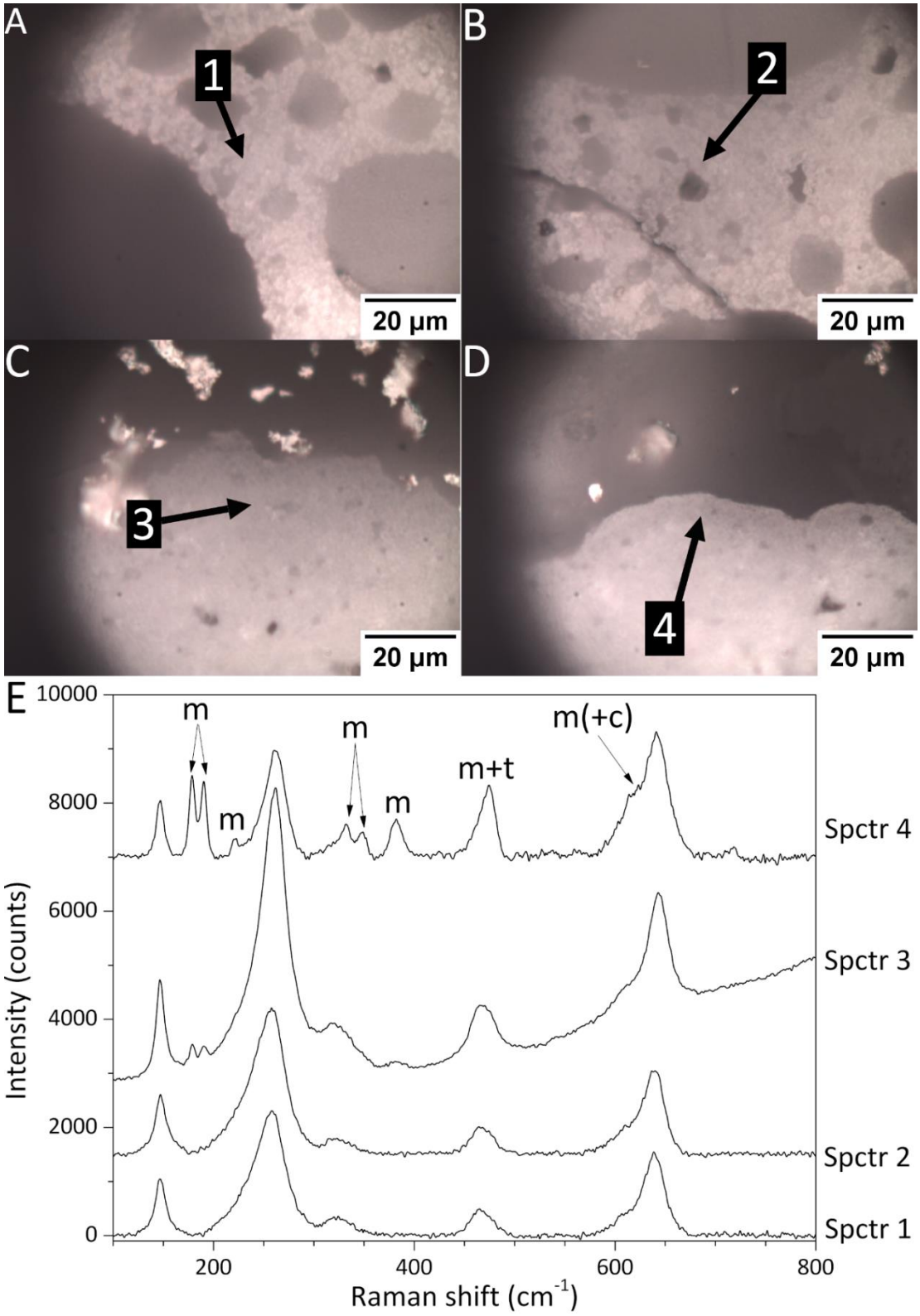

Figure 57 Optical micrographs of the SPS coating after CMAS corrosion (A-D), and corresponding micro-Raman spectra (E). Labels m, c, t indicate peaks assigned to monoclinic, cubic and tetragonal zirconia polymorphs, respectively. Note: Raman spectroscopy cannot differentiate between t and t' phase [135]

4 Results and Discussion Part II

In the previous chapter, the chemical interactions between the ZrO_2 + 7-8 wt.% Y_2O_3 (YSZ) TBC and the CMAS melt was discussed in detail, underlining the importance of the coating microstructure and the purity of the feedstock powders. Indeed, the results have shown that DVC coatings exhibit good CMAS resistance. Nonetheless, evidence of separation of columns could occur even within the dense "islands" of a DVC coating, because the large specific surface area of the boundaries among fine columnar grains constitutes a preferential site for CMAS attack. For this reason, the second part of the research was focused on the study of CMAS corrosion and TCF resistance of coatings with different chemistries (Gd/Yb/Y co-doped ZrO_2, $Gd_2Zr_2O_7$ and ZrO_2-55 wt.% Y_2O_3) with a DVC microstructure. The study also included bilayer systems consisting of Gd/Yb/Y co-doped ZrO_2, Gd_2ZrO_7 and ZrO_2-55 wt.% Y_2O deposited onto either DVC or porous YSZ layers. Indeed, the lower toughness of these alternative compositions in comparison to ZrO_2 + 7-8 wt.% Y_2O_3 means that (as shown in the Introduction) it is probably not possible to achieve satisfactory TCF resistance without a YSZ-based layer at the interface with the metallic bond coat, where the highest stresses are concentrated during thermal cycling and where delamination usually takes place. More specifically, systems comprise of a porous YSZ underlayer or a DVC YSZ underlayer were investigated to identify the most suitable combination. The second part of the thesis, shown in this chapter, is based on the paper "CMAS corrosion and thermal cycling fatigue resistance of alternative thermal barrier coating materials and architectures: A comparative evaluation" published on *Surface and Coatings Technology* [149].

4.1 Powders' and coatings' characterization

Particle size distributions, revealed from the laser scattering technique, are reported in Table 10 and in Figure 58. They are suitable for the plasma-spray process used to deposit the coatings. The cross-sectional micrographs of the feedstock powders are shown in Figure 59.

The ZrO_2-7 wt.% Y_2O_3 feedstock employed for porous layers, as well as the $Gd_2Zr_2O_7$ and Gd/Yb/Y co-doped ZrO_2 (Figure 59A, C, E) powders, were produced by an agglomeration and sintering process and they consist of spherical particles with internal porosity. The $Gd_2Zr_2O_7$ powders are denser than all other ones. By contrast, the ZrO_2-7 wt.% Y_2O_3 feedstock for the DVC underlayer and the ZrO_2-55 wt.% Y_2O_3 powder were obtained by fusing and crushing.

Accordingly, the SEM micrographs of these materials (Figure 59B,D) show very dense, irregular shapes.

Table 10 list of feedstock materials (Manufacturer / powders commercial designation are proprietary information)

Composition	**Particle size distribution : d_{10} / d_{50} / d_{90} [µm]**	**Manufacturing process**
ZrO_2-7 wt.% Y_2O_3 (for porous layers)	46/73/115	Agglomerated and sintered
ZrO_2-7 wt.% Y_2O_3 (for DVC layers)	22/35/54	Fused and crushed
$Gd_2Zr_2O_7$	20/31/46	Agglomerated and sintered
ZrO_2-55 wt.% Y_2O_3	21/35/59	Fused and crushed
ZrO_2-22 wt.% (Gd_2O_3-Yb_2O_3-Y_2O_3)	22/32/47	Agglomerated and sintered

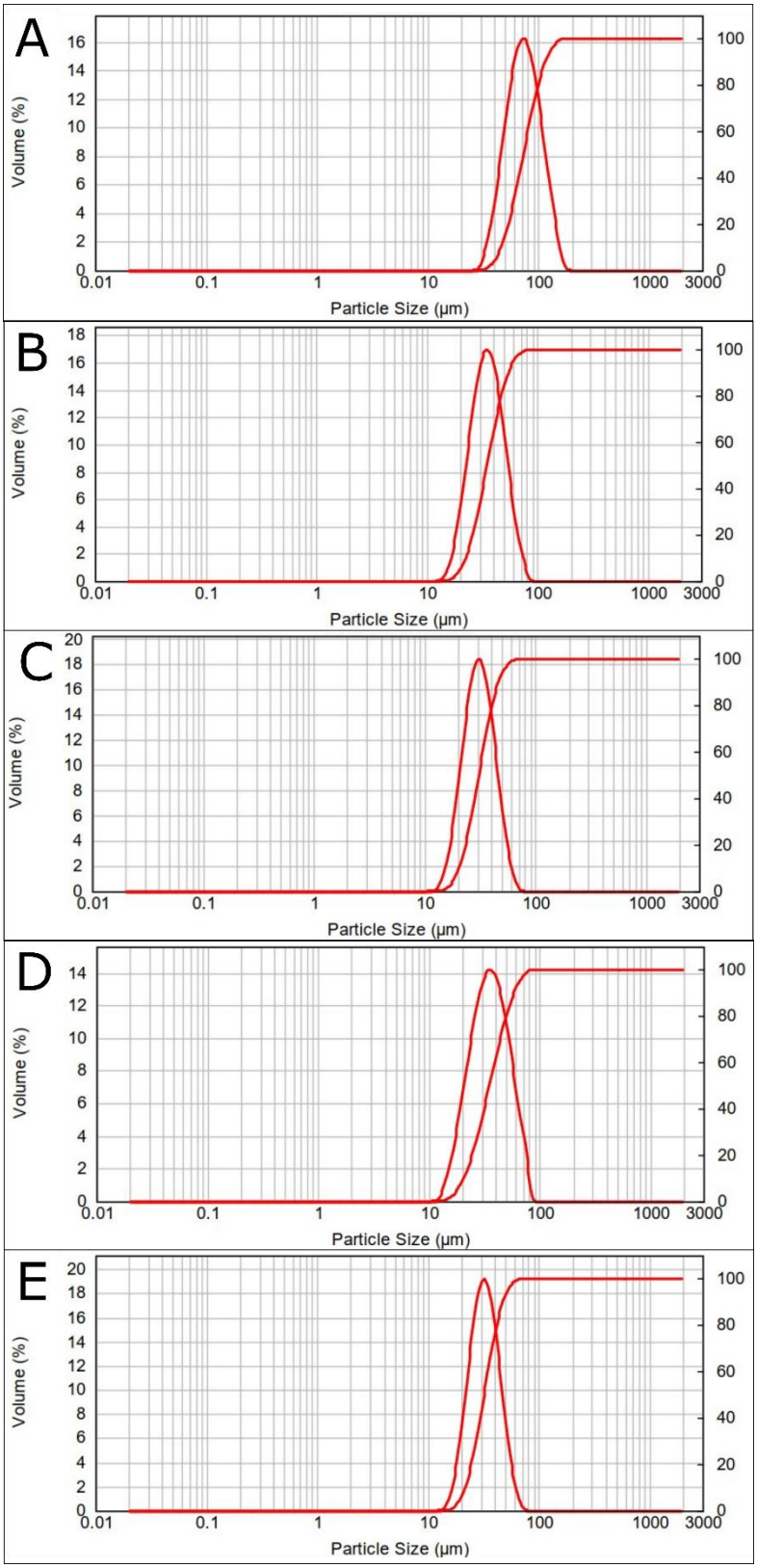

Figure 58 Particle size distributions of A) ZrO_2 -7 wt.% Y_2O_3 (agglomerated and sintered); B) ZrO_2-7 wt.% Y_2O_3 (fused and crushed); C) $Gd_2Zr_2O_7$; D) ZrO_2-55 wt.%Y_2O_3; E) ZrO_2-22 wt.% (Gd_2O_3-Yb_2O_3-Y_2O_3)

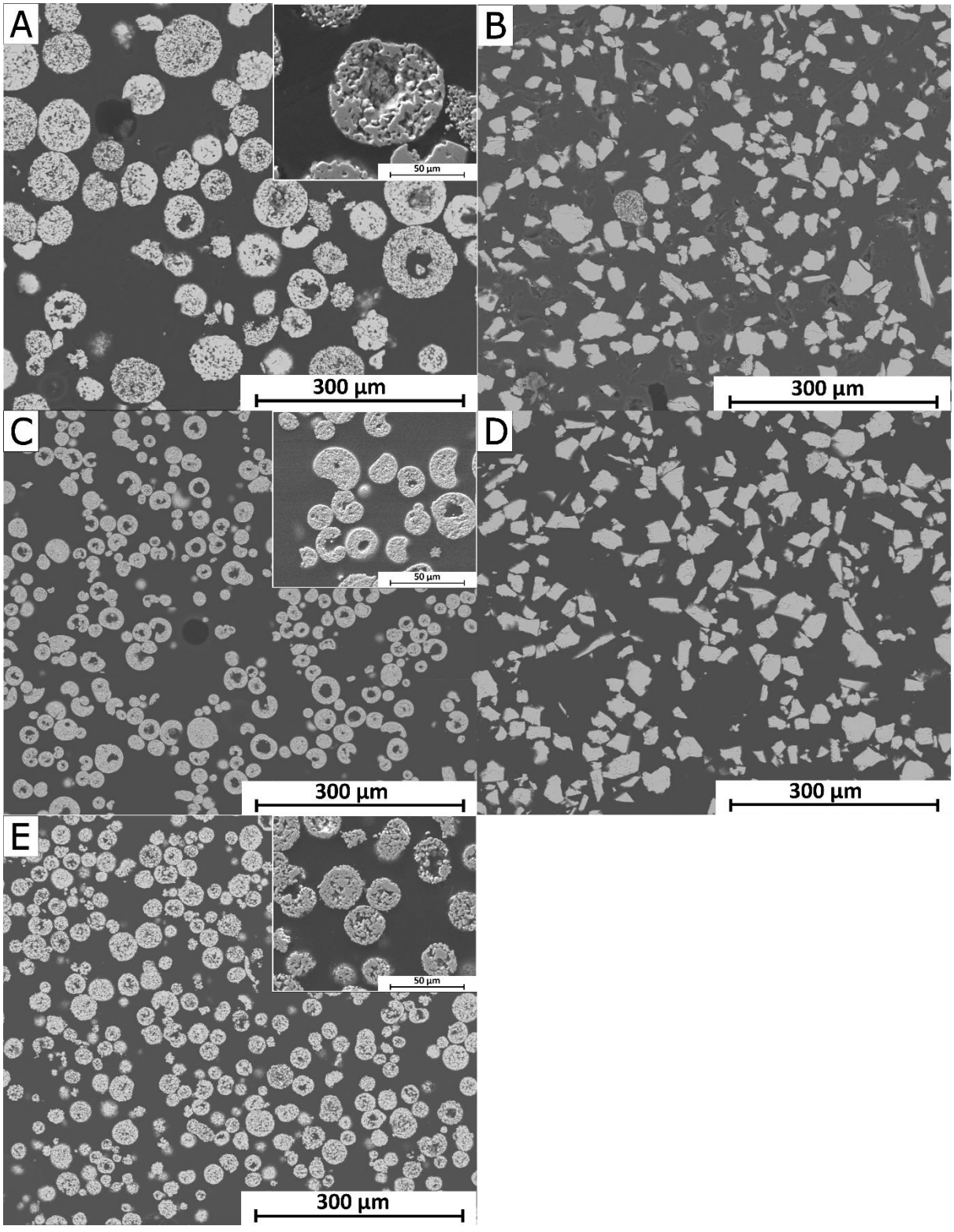

Figure 59 SE-SEM micrographs of the feedstock powders: A) ZrO_2-7 wt.% Y_2O_3 (agglomerated and sintered); B) ZrO_2-7 wt.% Y_2O_3 (fused and crushed); C) $Gd_2Zr_2O_7$; D) ZrO_2-55 wt.%Y_2O_3; E) ZrO_2-22 wt.% (Gd_2O_3-Yb_2O_3-Y_2O_3) [149]

The cross-sectional micrographs of the as-sprayed coatings are reported in Figure 60. The microstructures of all top coats are quite similar to one another and, in particular, some branching of the segmentation cracks along the interface between the deposition passes can be seen in all cases. This might have resulted from the feedstock powders being not optimized for the production of DVC architectures and/or from non-optimal deposition conditions. The internal porosity agglomerated and sintered powders, in particular, reduces the thermal conductivity of an individual particle and makes it difficult to achieve the high degree of melting required for this purpose. The thickness values of all coatings are reported in Table 11.

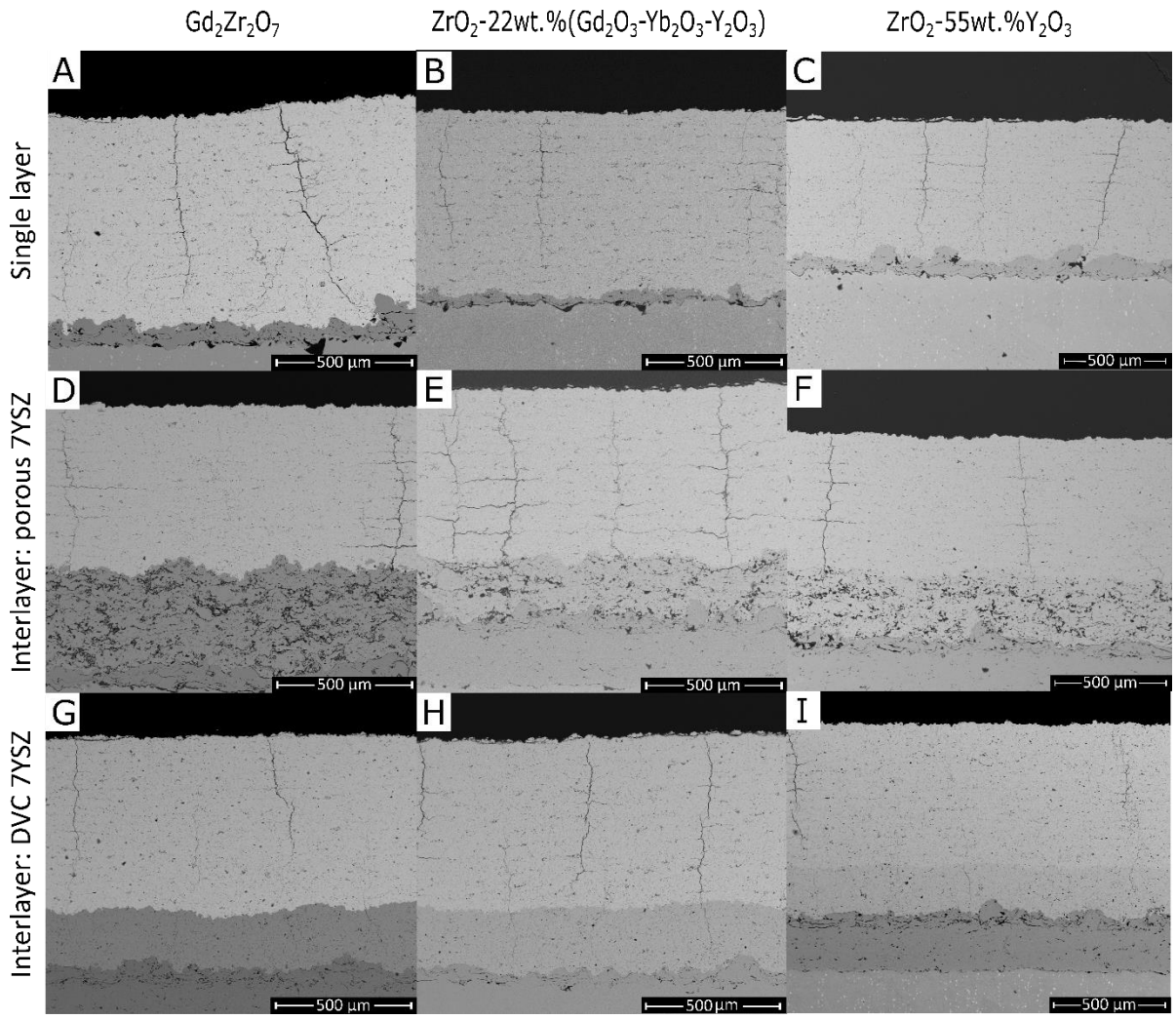

Figure 60 BSE-SEM micrographs of the monolayer coatings: A) $Gd_2Zr_2O_7$ (M3); B) Gd/Yb/Y-ZrO_2 (M4); C) ZrO_2-55 wt.%Y_2O_3 (M5); and bilayer coatings: D) $Gd_2Zr_2O_7$/porous 7YSZ (B1); E) Gd/Yb/Y-ZrO_2/porous 7YSZ (B2); F) ZrO_2-55 wt.%Y_2O_3/porous 7YSZ (B3); G) $Gd_2Zr_2O_7$/DVC 7YSZ (B4); H) Gd/Yb/Y-ZrO_2/DVC 7YSZ (B5); I) ZrO_2-55 wt.%Y_2O_3/DVC 7YSZ (B6) [149]

Table 11 Thickness and porosity values of the as-sprayed coatings

Samples	**Thickness (µm)**		**Porosity (%)**	
	Bottom layer	**Top layer**	**Bottom layer**	**Top layer**
M1	-	581 ± 38	-	14.2 ± 1.3
M2	-	534 ± 15	-	1.1 ± 0.3
M3	-	776 ± 46	-	1.1 ± 0.2
M4	-	668 ± 8	-	1.2 ± 0.3
M5	-	669 ± 33	-	1 ± 0.2
B1	336 ± 31	600 ± 21	15 ± 0.5	0.7 ± 0.2
B2	194 ± 33	611 ± 11	10.3 ± 1.1	0.8 ± 0.1
B3	250 ± 44	647 ± 20	10.8 ± 0.6	0.5 ± 0.2
B4	217 ± 26	629 ± 16	0.9 ± 0.2	0.3 ± 0.1
B5	229 ± 13	628 ± 5	0.9 ± 0.2	0.8 ± 0.2
B6	220 ± 20	630 ± 13	0.6 ± 0.2	0.4 ± 0.1

4.2 CMAS corrosion behaviour of Gd/Yb/Y co-doped ZrO_2 monolayer (M4) and corresponding bilayers (B2 and B5)

In Figure 61, macroscopic photographs of the samples after CMAS corrosion tests are reported. From the micrographs acquired on sample M4, i.e. the Gd/Yb/Y co-doped ZrO_2 monolayer (Figure 62A), it is apparent that molten CMAS, some of which remained as a layer on top of the coating, penetrated the vertical cracks. This can also be seen through EDX maps of sample B2 (Figure 63). EDX maps were useful to evaluate the CMAS infiltration at a macroscopic level, but they do not provide much information on the chemical interaction between the CMAS melt and the coating. As noted in Section 4.1, slight branching of the segmentation cracks along the interface between the deposition passes is visible (Figure 60B and Figure 62A - see circle).

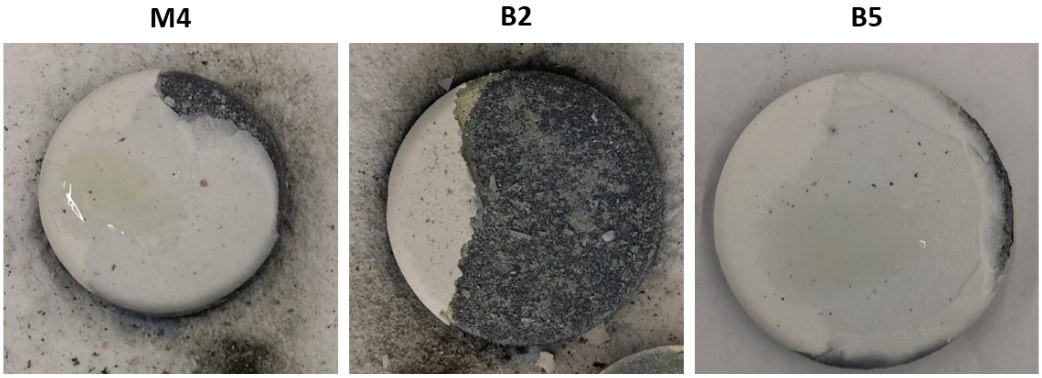

Figure 61 Photographs of samples M4, B2 and B5 after CMAS corrosion test

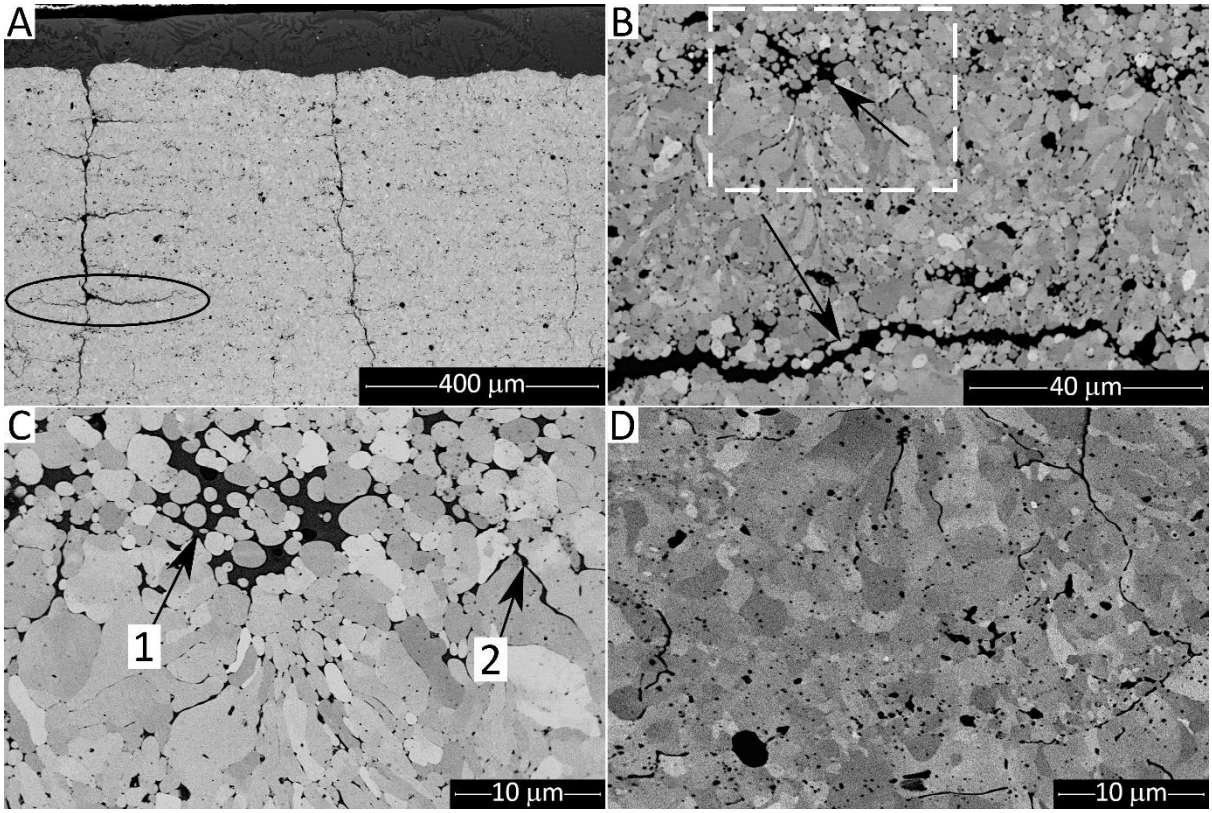

Figure 62 BSE-SEM micrographs of the monolayer Gd/Yb/Y-ZrO_2 (M4) sample after heating to 1250 °C with (A-C) and without (D) CMAS exposure. The dashed rectangle in panel B indicates the area magnified in panel C. The arrows in panel B indicate CMAS infiltration along branching cracks. In panel C, label 1 indicates an area of severe intergranular corrosion and label 2 indicates an area of moderate intergranular corrosion [149]

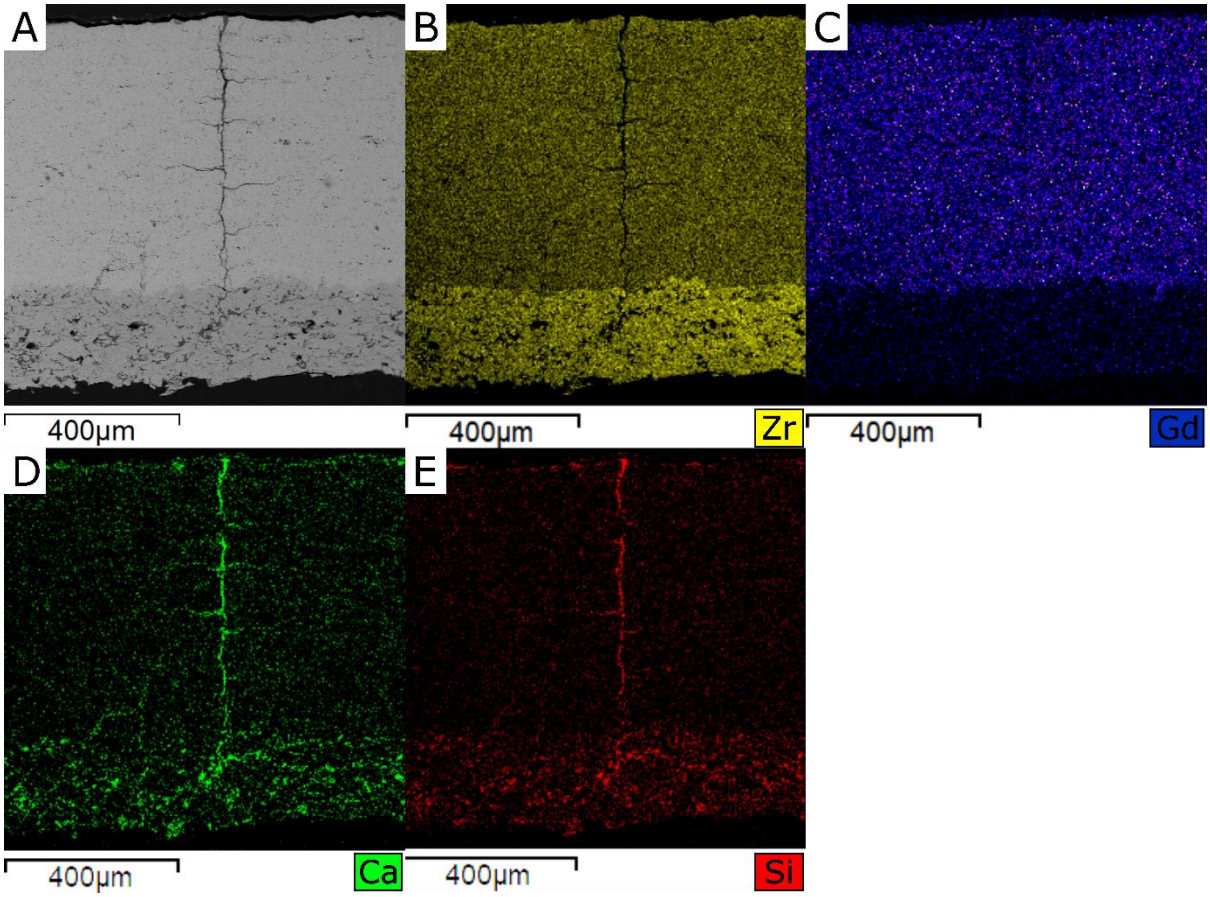

Figure 63 EDX maps acquired on the cross section of sample B2 after CMAS corrosion [149]

This defect is probably the result of non-optimal deposition conditions. Specifically, agglomerated and sintered powders are not ideally suited to produce DVC architectures, because their internal porosity makes it difficult to achieve the high degree of melting required for this purpose. Indeed, the agglomerated and sintered Gd/Yb/Y co-doped ZrO_2 powder (Figure 59E) is morphologically similar to the corresponding agglomerated and sintered 7YSZ powder (Figure 59A), both being made of loosely sintered particles with large pores. Such internal porosity probably reduces the thermal conductivity of the particles and makes it difficult to achieve complete melting, so that process parameters have to be set to such levels as to induce undesirable branching. The branching might be overcome if powders obtained by different processing routes would become available. The glass infiltrated these branching cracks (Figure 63D and Figure 63E). A signal of CMAS penetration is given by the many fine globular features identifiable around the cracks (Figure 62B, arrows; detail in Figure 62C, label 1). These are due to CMAS attacking the grain boundaries in the splats immediately adjacent

to the branching crack, so that grains were separated from one another and floated in the melt. CMAS proceeded along the grain boundaries, infiltrating towards the interior of the dense areas (Figure 62C, label 2). However, away from the cracks, the microstructure is much less altered: the bottom part of Figure 62C is indeed rather akin to the non-corroded area of Figure 62D and Figure 64, which shows some signs of sintering due to the rather high temperature (1250 °C) of the CMAS test. On the other hand, both on the top surface of the coating and along the sides of the transverse and branching cracks, no reaction products between the CMAS melt and the Gd/Yb/Y co-doped ZrO_2 layer can be found. It is therefore inferred that the mixed rare-earth stabilizers did not induce the precipitation of solid reaction products from the CMAS melt. Both internal areas (Figure 65, spectrum 1) and the globular structure around the cracks (Figure 65, spectrum 2) of sample M4 were analysed by Raman spectroscopy, showing a single peak at 615 cm^{-1} belonging to the cubic phase of zirconia. This suggests that not enough of the stabilizer mix was leached out of the undissolved parts of the grains to alter their original phase structure.

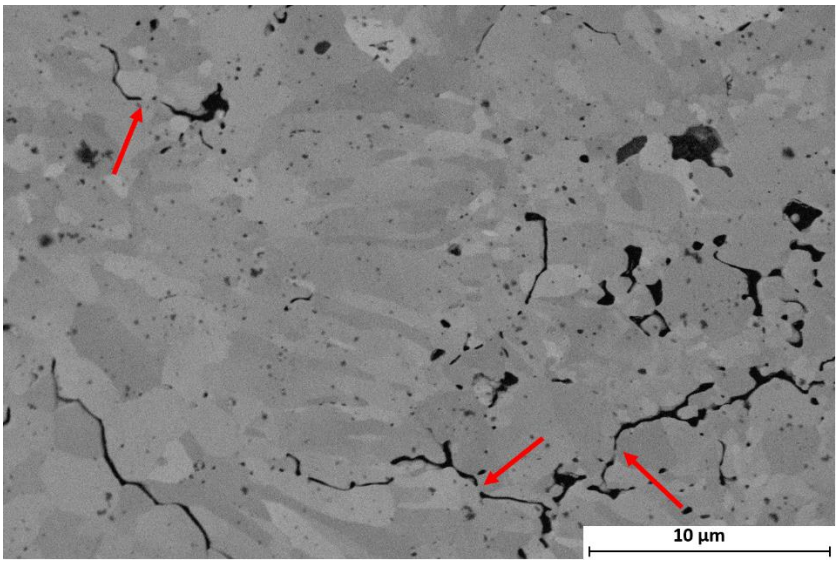

Figure 64 BSE-SEM micrograph at high magnification of the monolayer Gd/Yb/Y-ZrO_2 (M4) after heating to 1250 °C without CMAS exposure; red arrows indicate the signs of sintering due to the high temperature

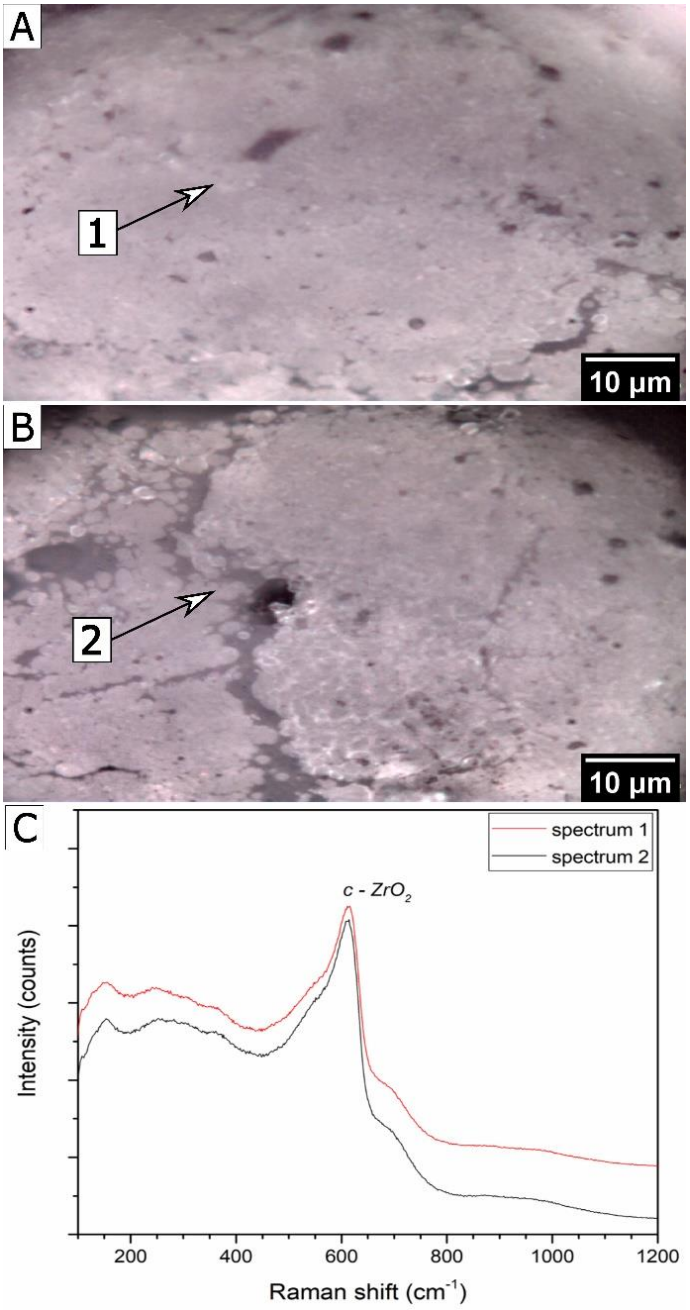

Figure 65 Optical micrographs of M4 in a dense area (A) and along a crack (B), and corresponding micro-Raman spectra (C) acquired on the positions marked by arrows [149]

Analogous considerations hold for the top coats of samples B2 (Gd/Yb/Y co-doped ZrO_2 + porous 7YSZ) and B5 (Gd/Yb/Y co-doped ZrO_2 + DVC 7YSZ). Indeed, the transverse and branching cracks in the co-doped top layer were infiltrated and CMAS started dissolving the boundaries of the zirconia-based grains along the crack surfaces, gradually moving toward the interior (Figure 66B and Figure 67B: compare to the non-corroded samples in the respective

panels E of the same figures, where necks formation along crack boundaries occurred instead). The interface between the top and bottom layers remained unaffected after the CMAS corrosion test, indicating good adhesion (Figure 66A and Figure 67A: compare to the same bilayer coatings heated to 1250 °C without CMAS in Figure 66D and Figure 67D, respectively).

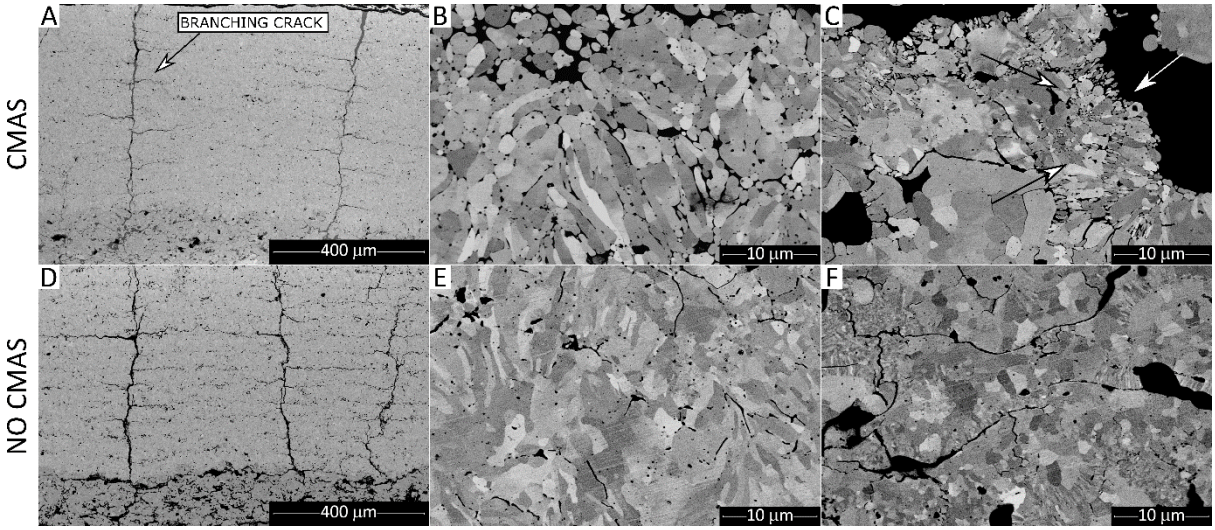

Figure 66 BSE-SEM micrographs of the bilayer with Gd/Yb/Y ZrO_2 top coat and porous 7YSZ bottom layer (B2), heated to 1250 °C with (A-C) and without (D-F) CMAS exposure: A,D: overviews; B,E: Gd/Yb/Y ZrO_2 top coat: C, F: 7YSZ bottom layer. Arrows in panel 59C indicate the separation of the grain boundaries due to the CMAS infiltration[149]

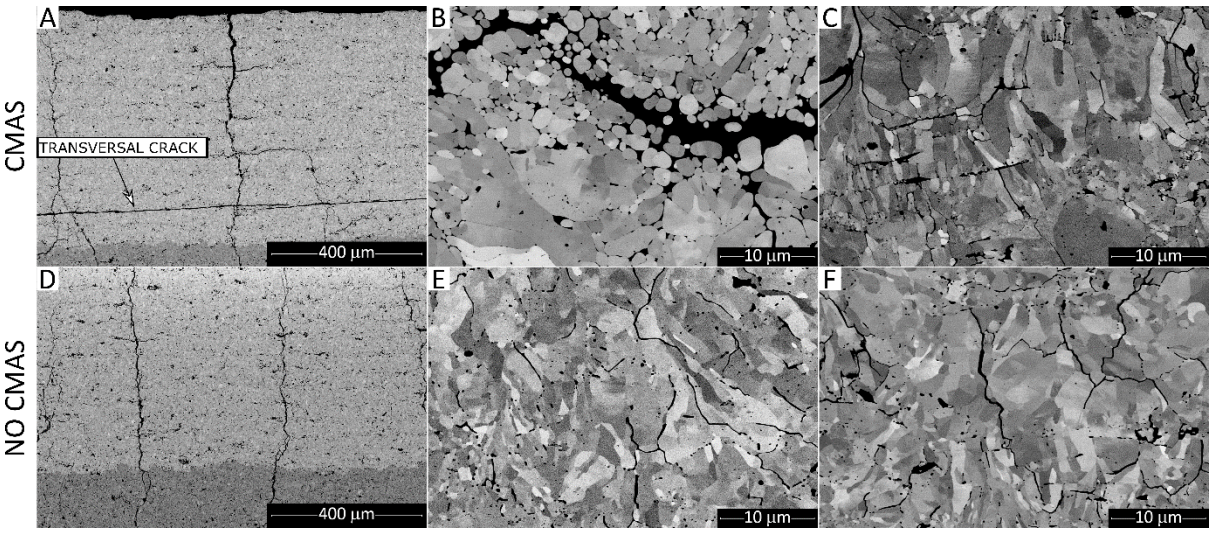

Figure 67 BSE-SEM micrographs of the bilayer with Gd/Yb/Y ZrO_2 top coat and DVC 7YSZ bottom layer (B5), heated to 1250 °C with (A-C) and without (D-F) CMAS exposure: A, C: overviews; B, E: Gd/Yb/Y ZrO_2 top coat: C, F: 7YSZ bottom layer [149]

The top coat of sample B5 exhibits a transversal crack just above the interface because of a "cold shock" caused by CMAS solidification upon cooling (Figure 67A). Indeed, infiltration of the cracks due to the isothermal testing conditions caused a complete loss of compliance and the stresses after cooling and CMAS solidification can lead to horizontal cracks.

However, the different architectures did affect the corrosion behaviour of these two coatings. As CMAS penetrated down to the 7YSZ porous layer, it spread inside its porosity as is visible in Figure 63 and therefore it compromised its integrity and cohesion by dissolving it just as it was seen for the single-layer system in chapter 3. By comparing Figure 66C to the corresponding un-corroded layer in Figure 66F, it is easy to observe that CMAS melt corroded the grain boundaries leading to their separation (Figure 66C - see arrows). On the contrary, in the sample B5 the presence of a DVC 7YSZ bottom layer did not offer an equally easy access to the CMAS melt to the interior of the dense areas (although CMAS did flow into the segmentation macro-cracks) and therefore no significant degradation of the microstructure occurred (compare Figure 67C to Figure 67F). In the CMAS-exposed portion of the sample, individual crystalline grains were distinguishable through the electron channelling contrast (Figure 67F), like they were in the non-exposed portion (Figure 67C), but intergranular separation was mostly not visible.

Micro-Raman spectra acquired on both top coats of samples B2 (Figure 68A, B, D: spectra 1 and 2) and B5 (Figure 68E, G: spectra 1 and 2) reveal the peak of cubic zirconia at 615 cm^{-1} both inside the coating (spectrum 1) and in correspondence of the globular areas along the boundaries of the vertical cracks (spectrum 2). This again confirms that, as long as the zirconia grains are not dissolved in the CMAS melt, they retain their cubic phase structure.

However, it should be noted that, on the top surface of the co-doped layer, porous annular features were found (Figure 69A). These features are identical to those reported in chapter 3 for 7YSZ. A high-magnification detail accordingly shows a banded structure indicative of the martensitic tetragonal-to-monoclinic transformation upon cooling (Figure 69B). It is inferred that extensive dissolution saturated the CMAS in ZrO_2 resulting in the re-precipitation of a non-stabilized compound that turned monoclinic upon cooling. However, this could not be confirmed by micro-Raman spectra because these features were smaller than the laser spot and the background by the CMAS glass covered the Raman spectrum of the zirconia phases. The amount of CMAS that reached the bottom layer was clearly not sufficient to destabilize the 7YSZ bottom layer, both in case of the DVC layer (Figure 68F, G: spectra 3 and 4) and of the

porous layer (Figure 68C, D: spectrum 3), despite the visible grain boundary corrosion mentioned previously.

Overall, it can be said that the CMAS corrosion resistance of the Gd/Yb/Y co-doped composition is not much better than that of a DVC layer of pure YSZ (compare to Figure 44 in chapter 3). Whilst the overall extent of damage to the Gd/Yb/Y co-doped ZrO_2 layer was likely worsened by the presence of branching cracks in comparison to a DVC YSZ coating, it would look like the CMAS advanced toward the interior of the coating through grain boundary corrosion, albeit slowly, just like it happens in CMAS-corroded YSZ DVC. Contrary to this conclusion, a few papers have recently suggested that horizontal crack branching, either in a columnar TBC by suspension plasma spraying [150] or in a feathery TBC by EB-PVD [151], could improve the resistance to CMAS-induced degradation. It was specifically argued that the horizontal cracks would siphon CMAS off the segmentation cracks or intercolumnar gaps through a capillary action. These "traps" would thus consume the CMAS and prevent it from filling the vertical cracks over their whole length, down to the interface with the underlying layers. Especially in [150], however, this beneficial effect was observed with a YAG-based TBC, which is intrinsically resistant to chemical corrosion by CMAS as it develops an yttrium-apatite layer along the reaction interface. Thus, CMAS would be trapped in the horizontal cracks without attacking the "bulk" of the TBC material. On the other hand, in the present case the CMAS melt can dissolve the grain boundaries of Gd/Yb/Y co-doped ZrO_2 and penetrate toward the interior of the material. Thus, the horizontal cracks would just increase the specific surface available to such dissolution process, leading to faster degradation of the intra-columnar material. The benefit of horizontal cracks acting as "traps" might also not be as significant in practice as it seems to be in an isothermal furnace test. A temperature gradient exists across a TBC under service conditions; therefore, the penetration of the molten CMAS could be hindered by its increased viscosity as the temperature decreases from the outer surface toward the interface with the bond coat. Whilst a test performed under thermal gradient conditions, e.g. a burner-rig test, would provide clearer information in this respect, this is outside the scope of the present research, which primarily aims to ascertain the reactivity of different TBC materials with state-of-the-art microstructures.

It is therefore apparent that the Gd/Yb/Y co-doped ZrO_2 system is unable to develop the reactive precipitation of protective solid compounds along the interface with CMAS.

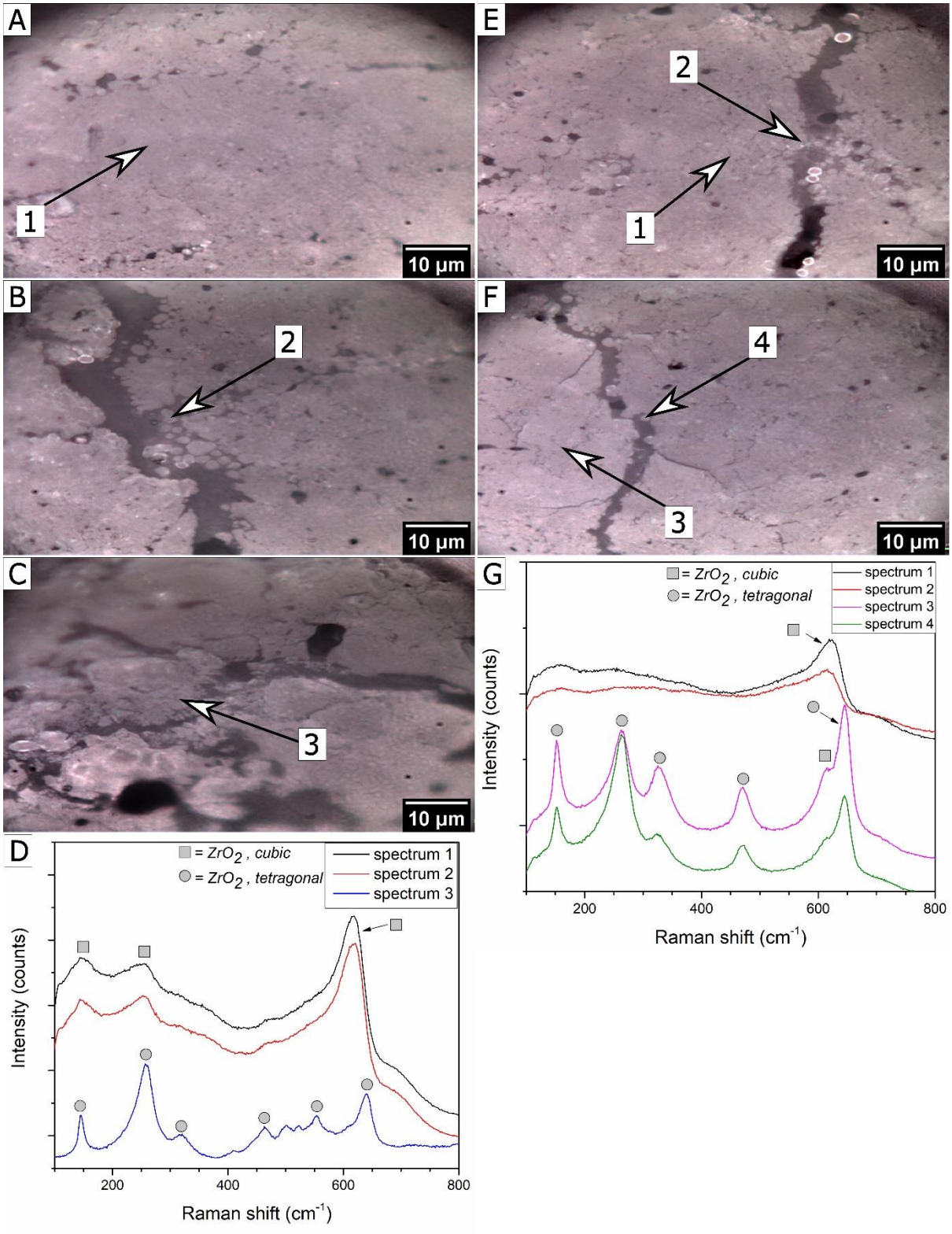

Figure 68 Optical micrographs of samples B2 (A, B, C) and B5 (E, F) after CMAS corrosion, and corresponding micro-Raman spectra (D, G). Panels C and F show the porous 7YSZ and DVC 7YSZ interlayer (respectively); all other images show the Gd/Yb/Y co-doped top layer[149]

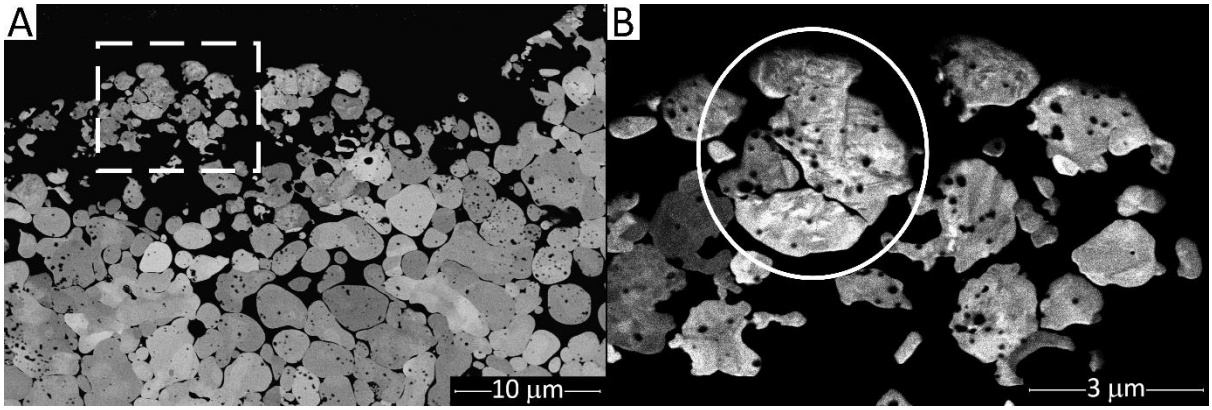

Figure 69 BSE-SEM micrographs of highly porous areas on the top surface of the Gd/Yb/Y co-doped ZrO_2 top layer in sample B2 after CMAS corrosion. Panel B shows a magnified view of the area marked in panel A; the circle in panel B shows a grain with visibly banded microstructure [149]

Optical basicity theory was applied to estimate the reactivity between all TBCs studied and CMAS. Using definition reported in Section 1.4.3, the optical basicities of $Gd_2Zr_2O_7$, the most reactive (toward CMAS) of all rare-earth zirconates, and of 7YSZ were computed to be 1.16 and 0.87 (Table 1) in [109].

Using the Λ_i data reported in Table 2 [109], the optical basicity of the current CMAS composition is approximately 0.69, which is within the typical range of 0.49-0.75 reported in the same reference for typical CMAS-based compositions. The optical basicity of the Gd/Yb/Y co-doped system is 0.88, which is almost the same as 7YSZ and does not differ enough from that of CMAS to trigger significant reaction. Thus, the Gd/Yb/Y co-doped system is continuously dissolved without developing any protective reaction layer, consistent with the present observations.

4.3 CMAS corrosion behaviour of $Gd_2Zr_2O_7$ monolayer (M3) and corresponding bilayers (B1 and B4)

Figure 70 shows the photographs of samples after the CMAS attack.

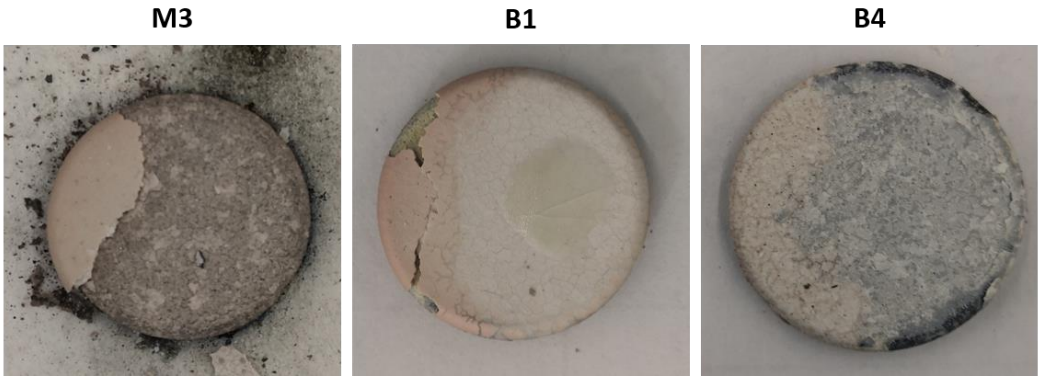

Figure 70 Photographs of samples M3, B1 and B4 after CMAS corrosion test

SEM micrographs (Figure 71A) show that more than half of the single-layer Gd-zirconate coating spalled off. Hence, the outer surface of the CMAS-corroded system could not be observed. As explained in the Introduction, one limitation of $Gd_2Zr_2O_7$ coating is its low toughness in comparison to 7YSZ. For example, Dwivedi et al. [57] measured K_{IC} values of 1.7-2.2 MPa·√m for all but the most defective APS 7YSZ coating they tested, and the values rose to around 4 MPa·√m after high-temperature sintering, whereas Gd-zirconate had a toughness of 1.0-1.2 MPa·√m that did not raise to more than 1.7 MPa·√m after sintering. The low toughness leads to early onset of delamination even at low stress. Its lower thermal expansion coefficient (in comparison to 7-8 YSZ) makes the situation even worse. A combination of thermal stress during cooling from 1250 °C to room temperature at the end of the furnace test and stiffening due to CMAS penetrating the segmentation cracks presumably caused the observed failure of the coating.

Nonetheless, the presence of CMAS within the vertical cracks can be seen even in the remaining part of the coating; hence, interactions between the CMAS melt and the coating can still be identified and discussed, because the surfaces of the segmentation cracks are equivalent to the outer surface of the compound in that they are in direct contact with a CMAS melt. The infiltration of the CMAS melt into the segmentation cracks is even more clearly visible in the EDX maps acquired on sample B1 (Figure 72). Notably, the top part of the segmentation crack

in Figure 71A seems to have been sealed by the formation of a compound with brighter contrast than CMAS in backscattered electrons imaging mode (see arrows). The Raman spectrum acquired on a vertical crack (Figure 73: spectrum 2) shows a strong peak at 878 cm^{-1} belonging to the gadolinium silicate $Ca_2Gd_8(SiO_4)_6O_2$, i.e. the apatite phase discussed in Section 1.5. This spectrum also contains Raman peaks due to the pyrochlore phase in the nearby coating: the peak at 315 cm^{-1} corresponds to the O-Gd-O bending vibration, and three bands at 420, 538, and 600 cm^{-1} can be assigned to Gd-O and two Zr-O stretching modes [152]. Additional peaks at 615 cm^{-1} and 400 cm^{-1} indicate the presence of the cubic fluorite zirconia phase. This is in accordance with many studies carried out on CMAS corrosion of gadolinium zirconate systems [123,153].

The formation of crystalline (solid) reaction products along the interface between the CMAS melt and $Gd_2Zr_2O_7$ did not prevent the CMAS melt from flowing into the segmentation cracks, but it did hinder further reaction. Thus, it prevented CMAS from penetrating toward the interior of the dense intracolumnar regions. In fact, unlike the pure YSZ and the co-stabilized layers described in chapter 3, grain boundaries seem completely unaffected. Grains are only told by their electron channeling contrast, without any visible sign of detachment and grain boundary corrosion (Figure 71B).

Notably, it looks like the branching cracks did not result in the CMAS attacking the grain boundaries of the intra-columnar regions, unlike the Gd/Yb/Y co-doped ZrO_2, due to the blocking effect of the reaction layer.

The protective effect of the reaction is also inferred by noting that the microcracks visible in the area not exposed to CMAS (Figure 71E, F) have been filled by a rather bright-contrast compound (Figure 71B- circle, C), not too dissimilar from the coating itself in its backscattered electrons contrast level. The $Gd_2Zr_2O_7$ DVC layer did, therefore, contain an interconnected crack network, apparently more developed than it is in the 7YSZ DVC layer (compare Figure 71E, F to Figure 44E). As reported by Kulkarni et al. [154], Gd-zirconate splats develop more microcracks during the thermal spray process than does 7YSZ due to its above-mentioned brittleness. The CMAS melt penetrated the interconnected network under the isothermal furnace treatment conditions (no temperature gradient across the coating) and reacted with Gd-zirconate just as it did in the larger segmentation cracks. It was thus converted to solid apatite, preventing any possibility for grain-boundary corrosion. A few internal parts where defects

must have been present in the as-deposited coating were also healed by reaction between CMAS and $Gd_2Zr_2O_7$ (Figure 71B, circle).

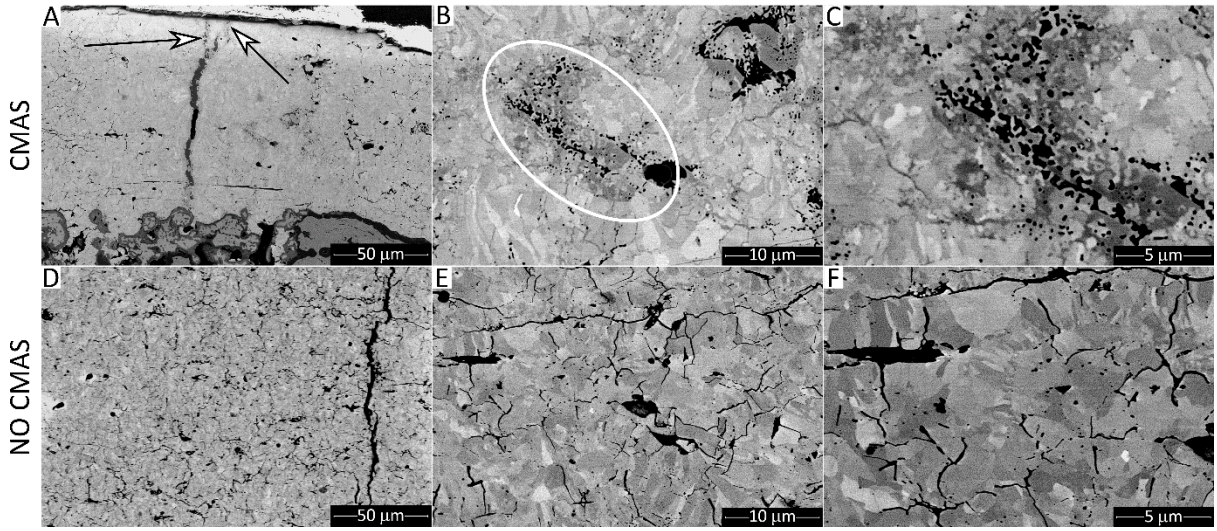

Figure 71 BSE-SEM micrographs of the monolayer $Gd_2Zr_2O_7$ (M3), acquired at different magnifications after heating to 1250 °C with (A-C) and without (D-F) CMAS exposure. Arrows in panel A: segmentation crack with precipitation of compounds; circle in panel B: CMAS-infiltrated defect with precipitation of compounds [149]

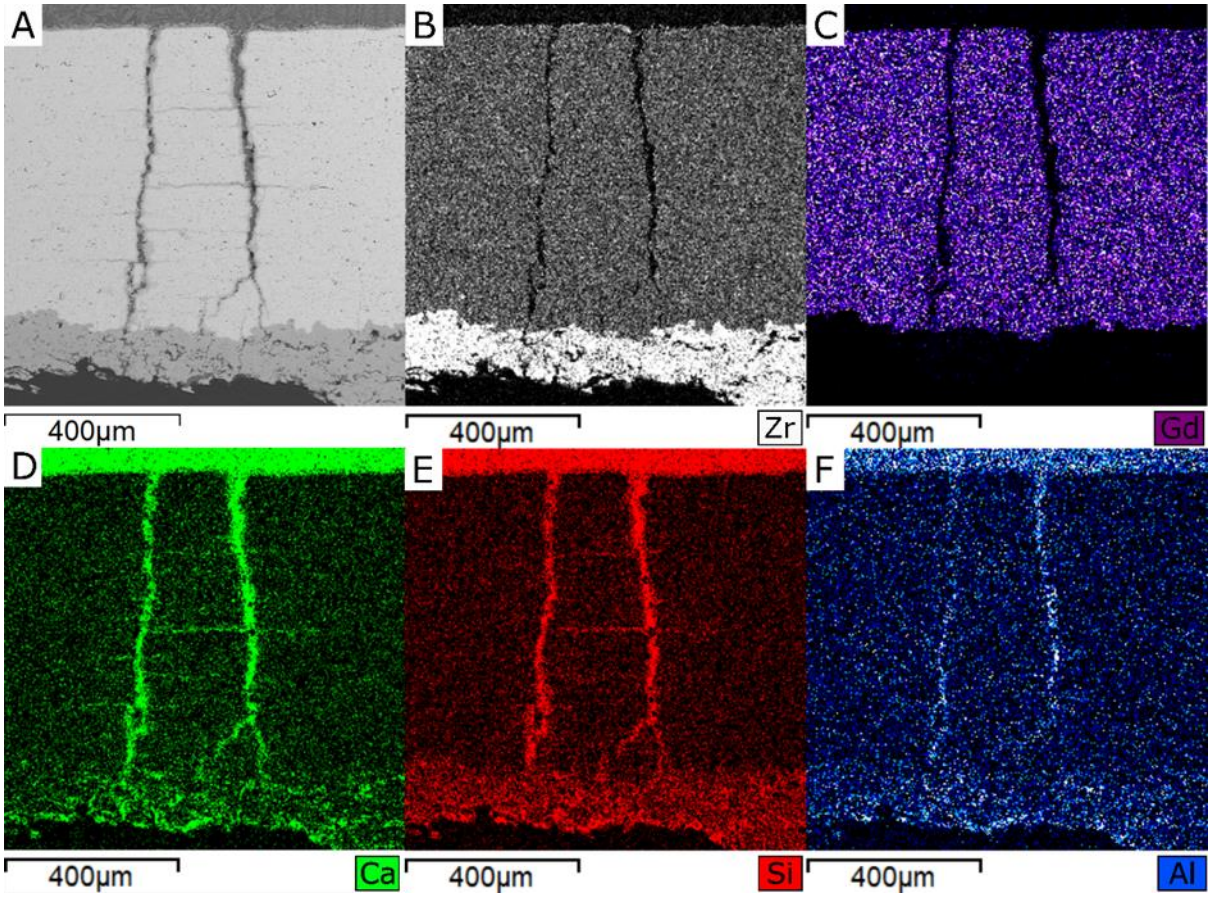

Figure 72 EDX maps acquired on the cross section of sample B1 after CMAS corrosion [149]

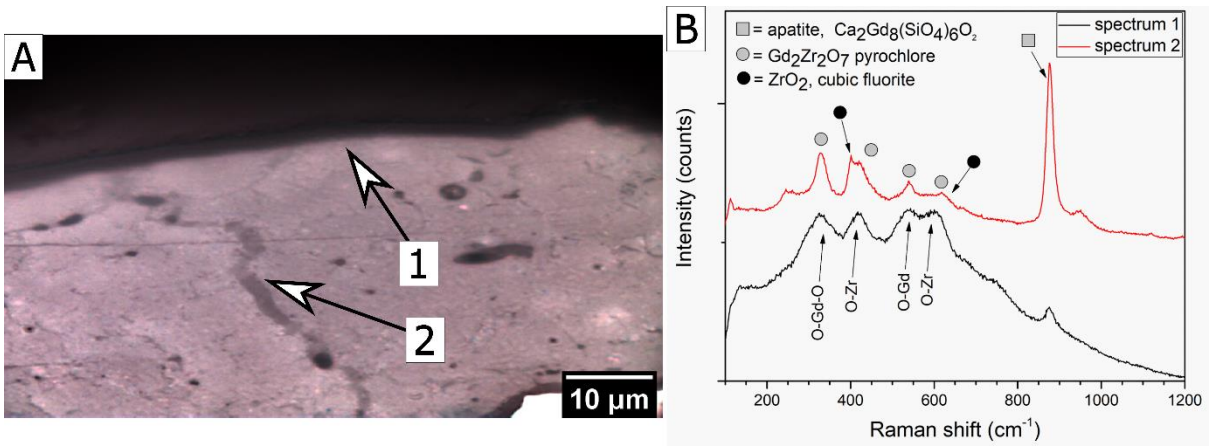

Figure 73 Optical micrograph of sample M3 after CMAS corrosion (A), and corresponding micro-Raman spectra (B) [149]

Sample B1 (Figure 74A-C) and sample B4 (Figure 74D-F) likewise exhibit a reaction between the CMAS melt and the $Gd_2Zr_2O_7$ top layer. Compounds precipitated around the sides of segmentation cracks (Figure 74A, B and D, E) and plugged the pre-existing network of interconnected microcracks (Figure 74C, F). EDX spectra acquired along a segmentation crack boundary of sample B1 reveals peaks belonging to Si, Ca, Gd and Zr, whilst other CMAS-related elements like Al and Mg are absent, suggesting the presence of the apatite phase $Ca_2Gd_8(SiO_4)_6O_2$ (Figure 75: spectrum 1). This is confirmed by Raman spectra acquired close to the sides of the segmentation cracks (sample B1: Figure 76A, C - spectrum 2; sample B4: Figure 76D, F - spectrum 2) and the outer surface (sample B1: Figure 76A, C - spectrum 4), dominated by the peak of apatite. Immediately behind the apatite reaction layer, towards the inside of the material, cubic fluorite (sample B1: Figure 76A, C - spectrum 4) is again present as the leftover from gadolinium depletion in the $Gd_2Zr_2O_7$ pyrochlore structure. Everywhere else in the internal area of the coating, Raman peaks correspond to $Gd_2Zr_2O_7$ with the pyrochlore structure (Figure 76A, C: spectrum 1; Figure 76D, F: spectrum 1) confirming the absence of phase alterations. The apatite-filled microcracks are too small to be detectable by micro-Raman spectroscopy, which probes areas of around 2 μm in lateral dimensions.

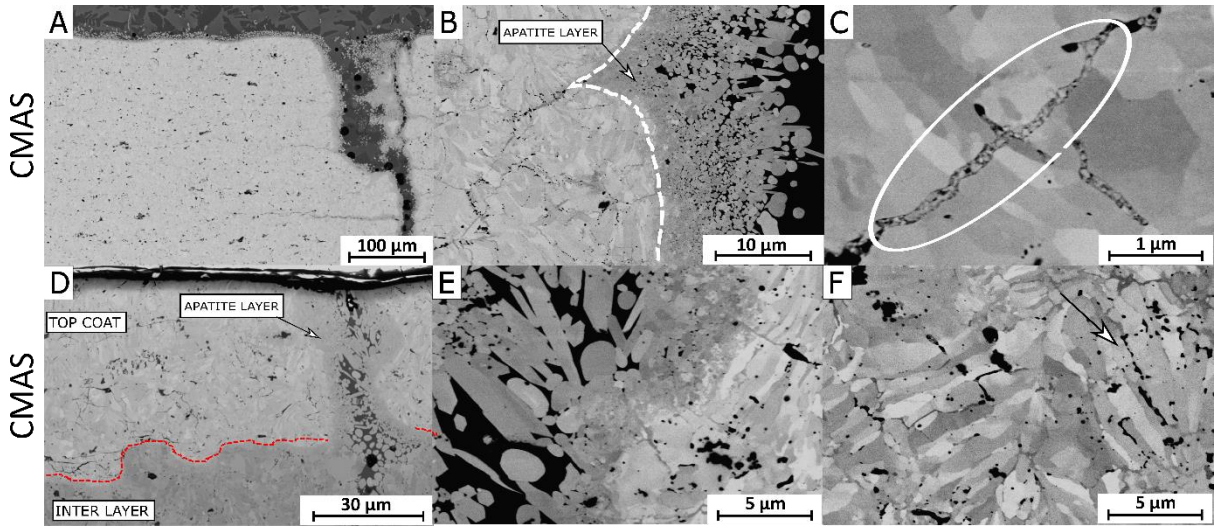

Figure 74 BSE-SEM micrographs of bilayers with $Gd_2Zr_2O_7$ top coat and porous 7YSZ (A, B, C: sample B1) or DVC YSZ (D, E, F: sample B4) interlayer after CMAS corrosion; red line in panel D indicates the interface between DVC YSZ interlayer and DVC $Gd_2Zr_2O_7$ top coat [149]

However, spallation of the coating after CMAS attack occurred within the APS 7YSZ interlayer, which was chemically degraded by the CMAS as it penetrated through the segmentation cracks of the top layer. This can be also noticed in the EDX map of Figure 72. The previous analysis indeed showed that the interface reaction between CMAS and $Gd_2Zr_2O_7$ prevented the degradation of the latter, but it did not seal its pores and cracks, and allowed the CMAS melt to flow through them. In particular, just as reported in chapter 3, porous 7YSZ (Figure 77A, B) is much more degraded than the DVC interlayer (Figure 77C, D). Again, the temperature gradient that is expected in service means that it is unlikely for a CMAS melt to reach the YSZ interlayer in a practical condition. Nonetheless, the porous layer constitutes a potential risk because it could be structurally undermined by CMAS corrosion in case it is exposed.

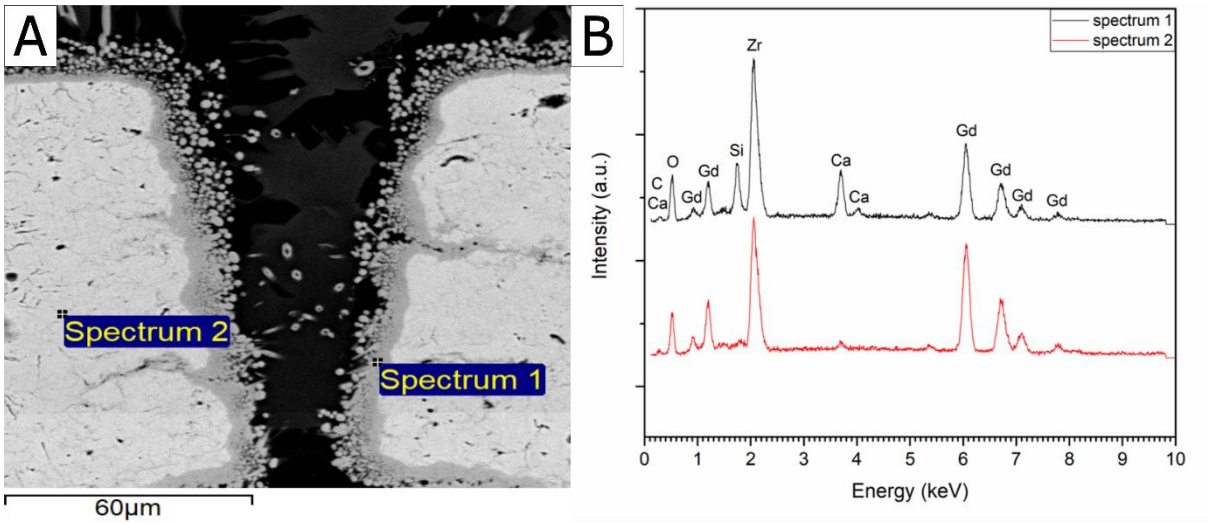

Figure 75 EDX spectra acquired on the top coat of sample B1 after exposure to CMAS [149]

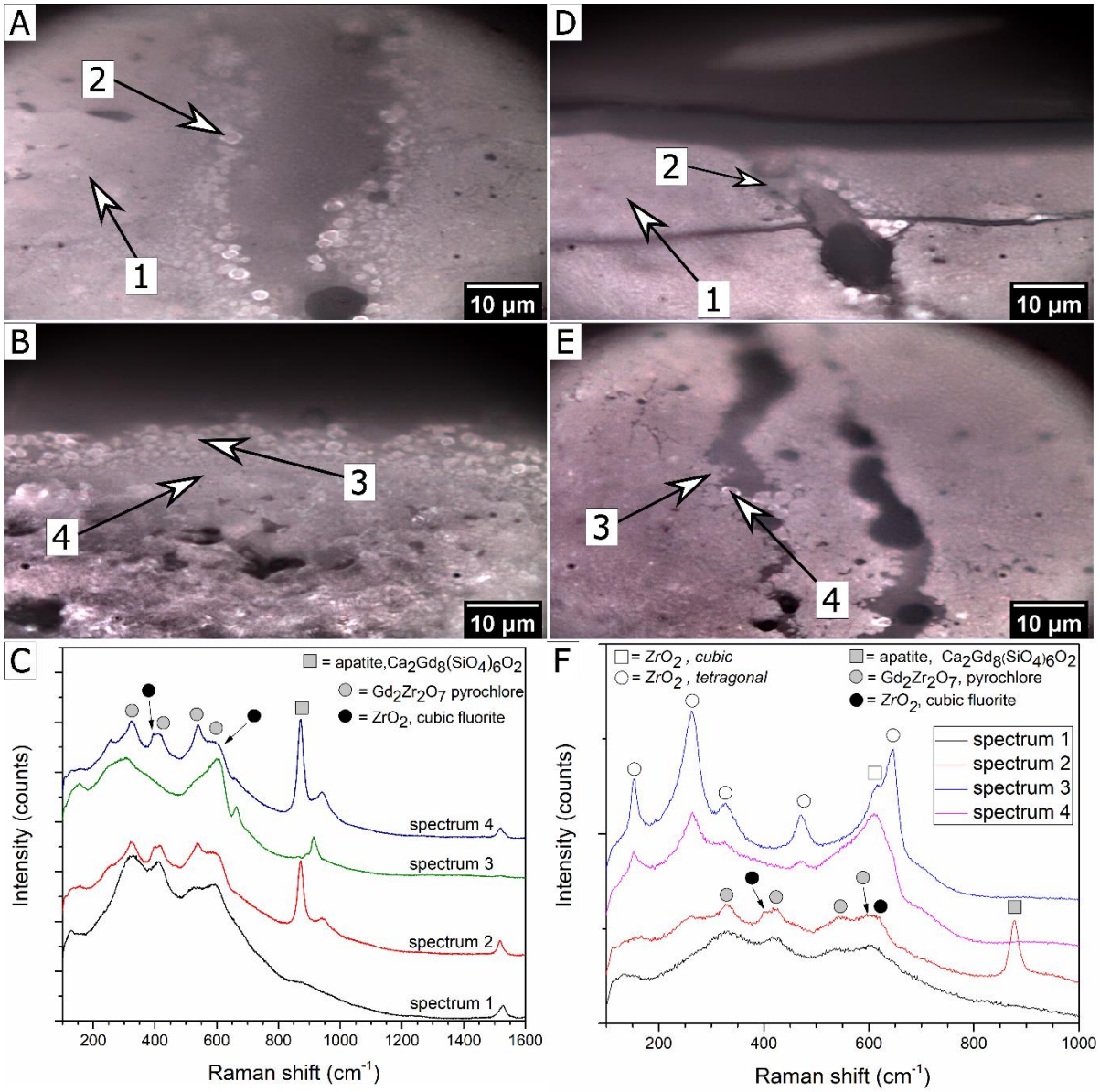

Figure 76 Optical micrographs of B1 (A, B, C) and B4 (D, E, F) samples after CMAS corrosion, and corresponding micro-Raman spectra. Specifically, panel E shows the DVC 7YSZ interlayer, whereas all other images refer to the $Gd_2Zr_2O_7$ top layer [149]

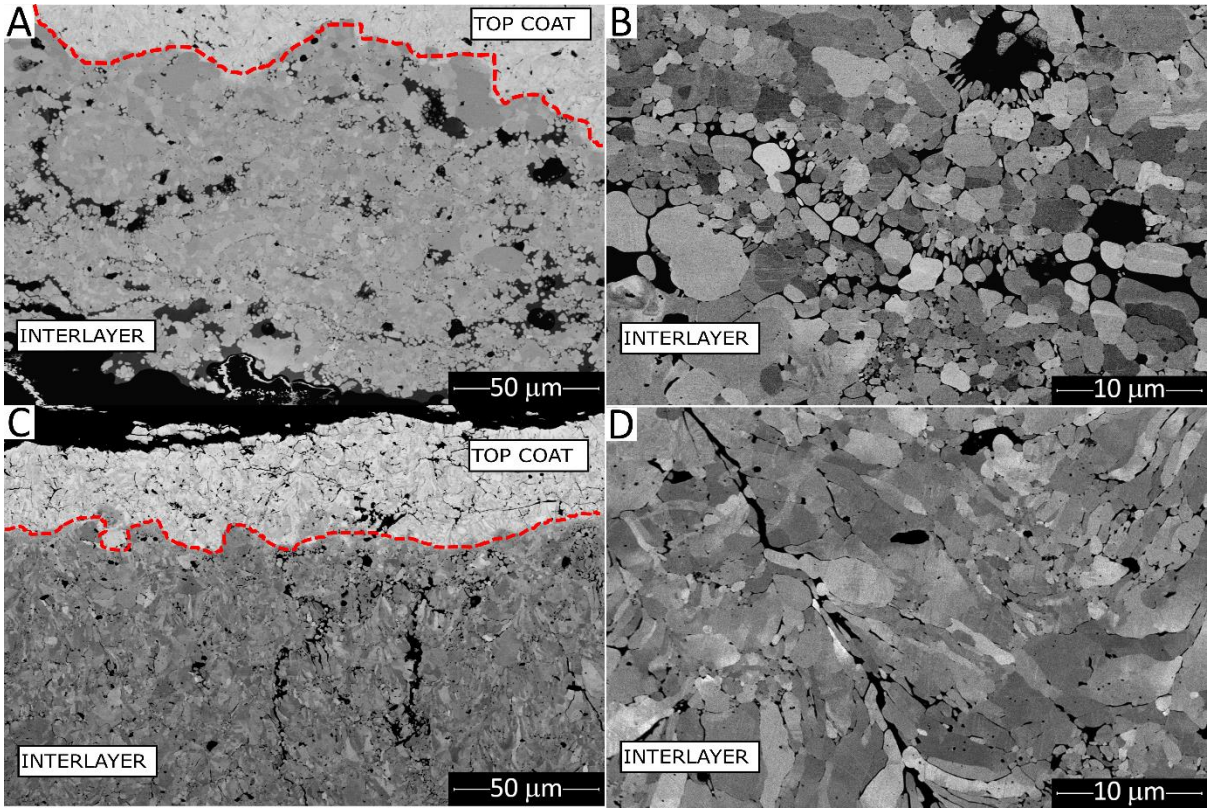

Figure 77 BSE-SEM micrographs of the interface between the porous $Gd_2Zr_2O_7$ top layer and the porous 7YSZ interlayer (A) or DVC 7YSZ interlayer (C), with corresponding high-magnification details of the interlayers (B: porous; D: DVC) after CMAS attack [149]

4.4 CMAS corrosion behaviour of ZrO_2-55 wt.%Y_2O_3 monolayer (M5) and corresponding bilayers (B3 and B6)

Figure 78 shows samples after CMAS corrosion test.

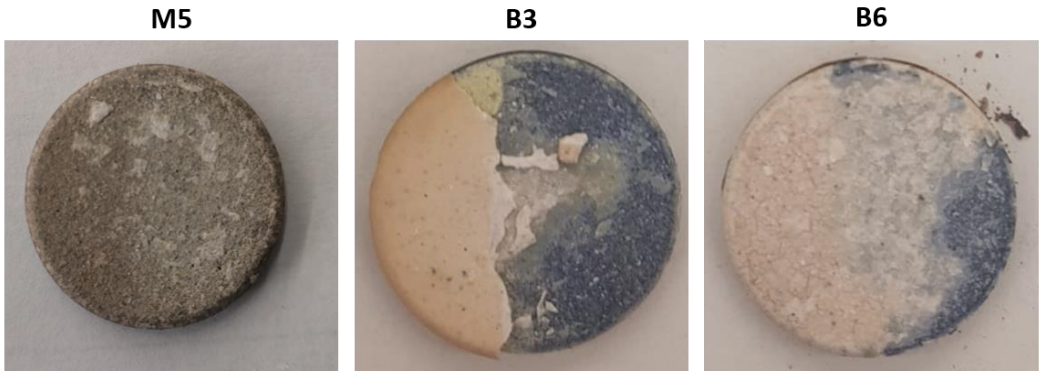

Figure 78 Photographs of samples M5, B3, and B6 after CMAS corrosion test

In the case of sample M5 (ZrO_2-55 wt.% Y_2O_3), the coating spalled after the test in the region subjected to CMAS corrosion and also in the area heated without CMAS, as shown in Figure 79A. This means that the single-layer ZrO_2-55 wt.% Y_2O_3 system suffers from the same issues as single-layer Gd zirconate. In fact, the cubic crystalline phase developed by the ZrO_2-55 wt.% Y_2O_3 system has lower fracture toughness than t'-7YSZ, which leads to coating failure [155]. The portion of the coating that remained adherent to the substrate (and could therefore still be observed) does not exhibit grain-boundary dissolution (Figure 79B). Specifically, individual grains identifiable through the electron channeling contrast in Figure 79B were tightly adherent to one another. Segmentation cracks show the formation of reaction products brighter than the CMAS phase, and the microcracks, again particularly numerous due to the tendency of the brittle ZrO_2-55 wt.% Y_2O_3 splats to crack more frequently than 7YSZ ones during the plasma spray process as explained in Section 3.3, are partly plugged with the same products (Figure 79B - arrows).

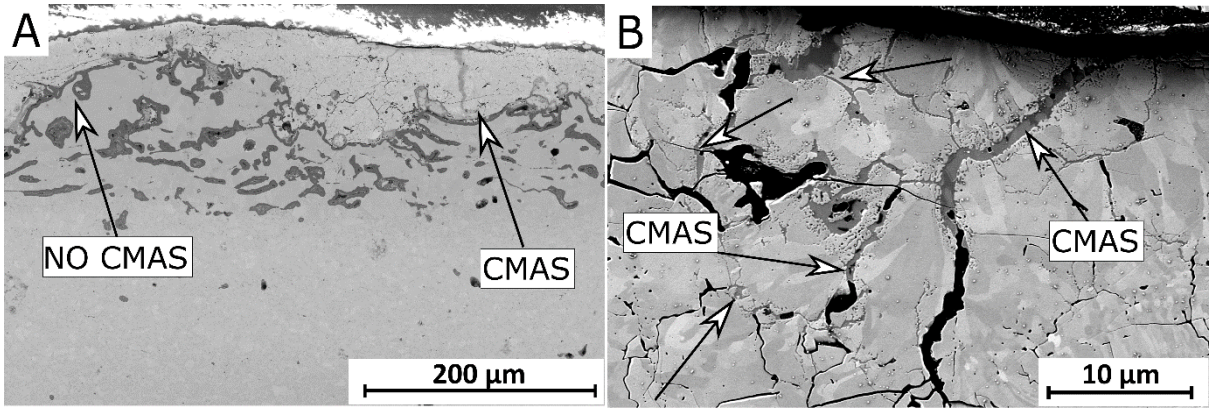

Figure 79 BSE-SEM micrographs of the monolayer 55YSZ (M5) coating after CMAS exposure: overview (A) and detail (B). The arrows in panel B indicate reaction products within macro- and micro-cracks [149]

In the bi-layer samples B3 and B6, the ZrO_2-55 wt.% Y_2O_3 top layer remained partially attached to the YSZ bottom layers (Figure 80A, D), although it did crack and delaminate quite severely, especially with the DVC 7YSZ interlayer (Figure 80D). As can be observed in Figure 80B, the ZrO_2-55 wt.% Y_2O_3 top layer is microstructurally unaffected, but its interface between with the underlayer is degraded. On the top coat (Figure 80A, marked with a black circle) precipitates with different morphologies were once again identified along the interface with CMAS. In more details, bright elongated grains (EDX spectrum 1 in Figure 81) contain intense peaks of Si, Y, Ca, and O, suggesting the formation of a silicate rich in yttrium and calcium.

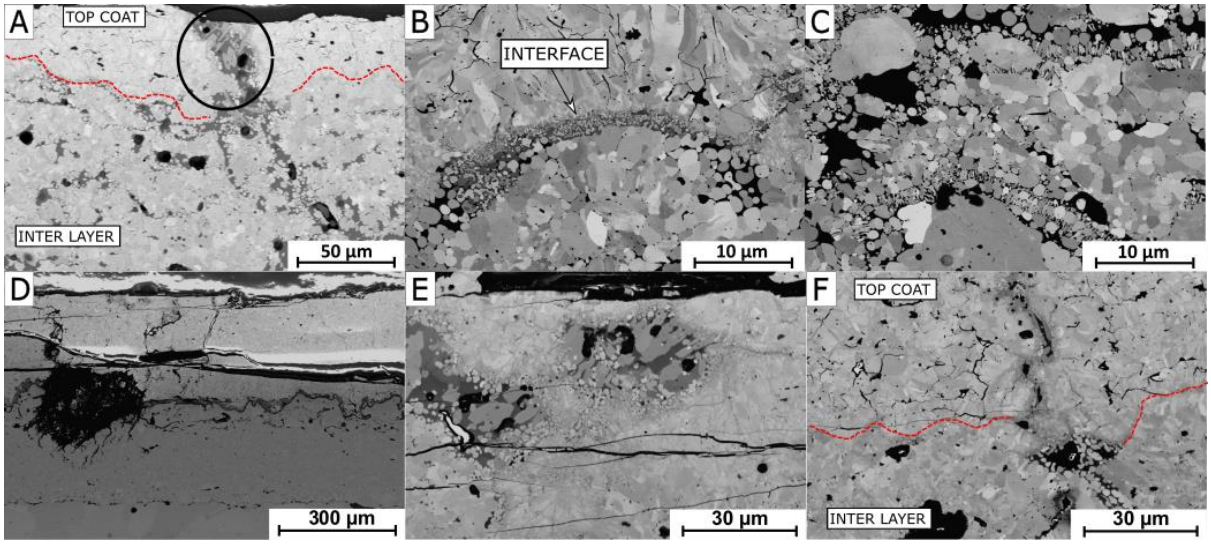

Figure 80 BSE-SEM micrographs of bilayers with ZrO_2-55 wt.% Y_2O_3 top coat (A, B) and 7YSZ porous bottom layer (B3) (C); ZrO_2-55 wt.% Y_2O_3 top coat (D, E) and 7YSZ DVC bottom layer (B6) (F) [149].

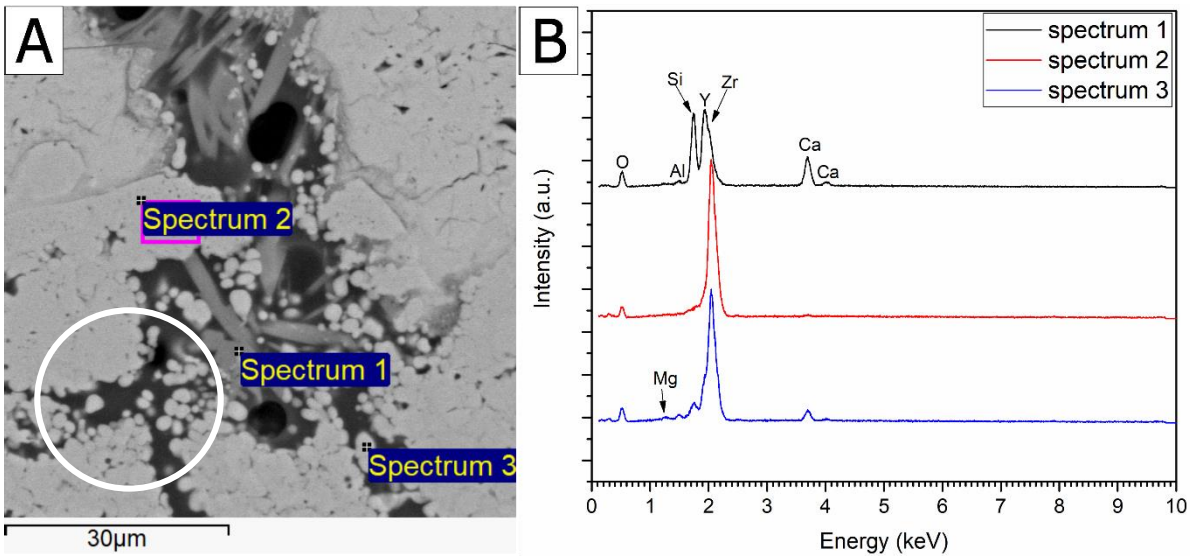

Figure 81 EDX analysis acquired on the top coat of sample B3 [149]

The characteristic Raman peak of the apatite phase accordingly appeared at 875 cm^{-1} along the interface between the coating and CMAS (Figure 82B-C, spectra 2 and 3). Micro-Raman spectra in the interior of the ZrO_2-55 wt.% Y_2O_3 top layer (Figure 82A, C: spectrum 1; Figure 82B, D: spectrum 1), instead, show a weak, broad band indicating the presence of cubic zirconia phase. Consistent with the expectations put forward in the Introduction, an yttrium-based

silicate is therefore developed as the main reaction product between CMAS and ZrO_2-55 wt.% Y_2O_3, like Gd-apatite was formed from $Gd_2Zr_2O_7$. Its formation within the macro- as well as micro-cracks prevented the CMAS melt from attacking the coating, so that grain-boundary dissolution was not observed, just as it happened for $Gd_2Zr_2O_7$. The branching cracks (Figure 60) also had no apparent negative effect. Nonetheless, the Y-apatite might not be as effective in preventing CMAS infiltration as is the Gd-apatite. In fact, Y-apatite crystals float within the CMAS melt (Figure 80A and Figure 81) instead of forming a more continuous layer along the interface with CMAS, as $Gd_2Zr_2O_7$ did (Figure 74B, E and Figure 75). Accordingly, rounded particles can be seen to detach from the ZrO_2-55 wt.% Y_2O_3 surface (Figure 81A-circle), which means that some grain-boundary corrosion did happen in this case. It did not proceed further into the dense part of the layer probably because, as CMAS entered tinier cracks, it was entirely saturated with yttria and, thus, it solidified completely.

Whilst the present findings do confirm that "high-yttria" compounds do precipitate apatite when in contact with a CMAS melt [109,156], the comparison would therefore suggest no benefit over Gd-zirconate.

Interestingly, this is consistent with the prediction from optical basicity, which, for the ZrO_2-55 wt.% Y_2O_3 composition, is computed as 0.99, numerically undistinguishable from that of the $2ZrO_2{\cdot}Y_2O_3$ composition in [109] and lower than that of Gd-zirconate.

Regarding the bottom layers, molten CMAS penetrates massively into and, again, attacks severely the porous 7YSZ layer (Figure 80C), whereas the DVC 7YSZ coating exhibits less widespread damage (Figure 80F).

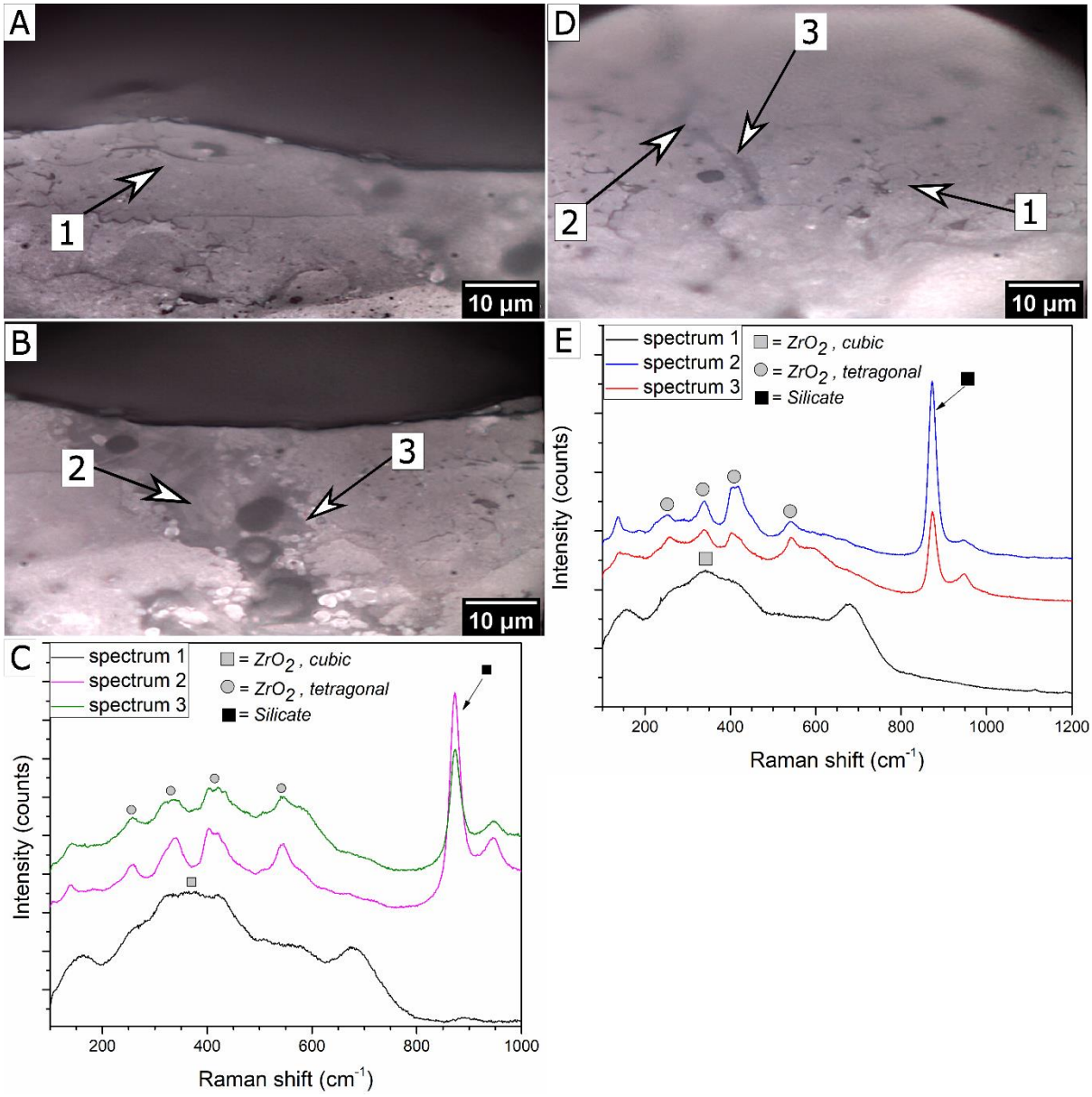

Figure 82 Optical micrographs of samples B3 (A, B) and B6 (D) after CMAS corrosion, and corresponding micro-Raman spectra (C and E, respectively) [149]

4.5 Thermal cycling behaviour

An essential requirement that TBCs must satisfy is to maintain protection for a large number of thermal cycles. Because there is no internationally accepted standard for thermal cycling furnace testing of TBC systems, the thermal cycling lifetime of the monolayer and bilayer systems was evaluated comparatively with porous and DVC 7YSZ layers of standard industrial quality as references. The number of thermal cycles to failure, normalized over a threshold value corresponding to an OEM acceptance level [60], is reported in Figure 83 for each of the tested systems.

It is preliminarily remarked that, among the reference samples, DVC 7YSZ has lower thermal cycling lifetime than porous 7YSZ. This can be explained with the greater compliance of porous layers. On the other hand, this result contradicts the previous findings by Viswanathan et al. [157], who reported longer thermal cycling lifetime for a DVC 7YSZ layer than for porous ones, despite the lower elastic modulus of the latter, and ascribed it to the significantly higher fracture toughness of the DVC layer. This discrepancy means that, whilst a monotonic correlation between the elastic modulus and toughness of 7YSZ coatings certainly exists as demonstrated in [57,157], the exact balance between these two properties, i.e. whether the benefit of higher toughness offsets the negative consequences of higher stiffness or not, probably varies a lot with the specific microstructural details of each sample. It is not the subject of this research to investigate the thermal cycling fatigue as a function of elastic modulus and fracture toughness. The way this balance reflects on the thermal cycling lifetime might also depend on the exact thermal cycling conditions. For example, each thermal cycle in [157] lasted 24 h, whilst the cycle described in Section 2.3 lasted about 70 min. A 24-h cycle with long isothermal holding might promote sintering and thus be more disadvantageous for a porous TBCs, which specifically relies on the compliance provided by its network of pores and microcracks.

All the other DVC monolayer systems showed even lower thermal cycling lifetime compared to both 7YSZ references, with the $Gd_2Zr_2O_7$ and ZrO_2-55wt.% Y_2O_3 exhibiting particularly poor performance, as could be reasonably expected based on the lower fracture toughness [43]. For these reasons, the addition of a 7YSZ bottom layer is mandatory to increase the final thermomechanical performances of TBCs. Among the bilayer systems, the porous 7YSZ bottom layer yielded much better performances than the DVC one with the $Gd_2Zr_2O_7$ and ZrO_2-55wt.% Y_2O_3 top coats. These top layers have lower thermal expansion coefficient than 7YSZ,

so a highly compliant underlayer might be needed to prevent too much stress from building up at the interface with the TGO and the bond coat. Specifically, the thermal expansion coefficient of $Gd_2Zr_2O_7$ is quoted as 8.1-10.5 × 10^{-6} K^{-1} at 200-1000 °C [43]. Data for ZrO_2-55wt.% Y_2O_3 is not available. Hayashi et al. experimented that the thermal expansion coefficient decreases with the increasing of the Y_2O_3 content [158]. Based on the results of Hayashi et al. the thermal expansion coefficient of ZrO_2-55wt.% Y_2O_3 should be lower than 7YSZ CTE.

Interestingly, the Gd/Yb/Y co-doped ZrO_2 top layer was the only one that exhibited equally good thermal cycling lifetime even with a DVC YSZ bottom layer, because its thermal expansion coefficient was better matched to the 7YSZ (lower overall amount of stabilizers). Notably, this system performed even better than single-layer DVC 7YSZ.

Overall, the best performances were obtained with the GZO/porous 7YSZ (B1) and Gd/Yb/Y-ZrO_2/ porous and DVC YSZ (B2 and B5) systems, whose thermal cycling fatigue test was stopped without visible failure in all cases. The 55YSZ/porous 7YSZ (B3) system, on the other hand, did not exhibit satisfactory performances, and it even showed extreme scatter among distinct specimens, as testified by the extremely wide error range in Figure 83.

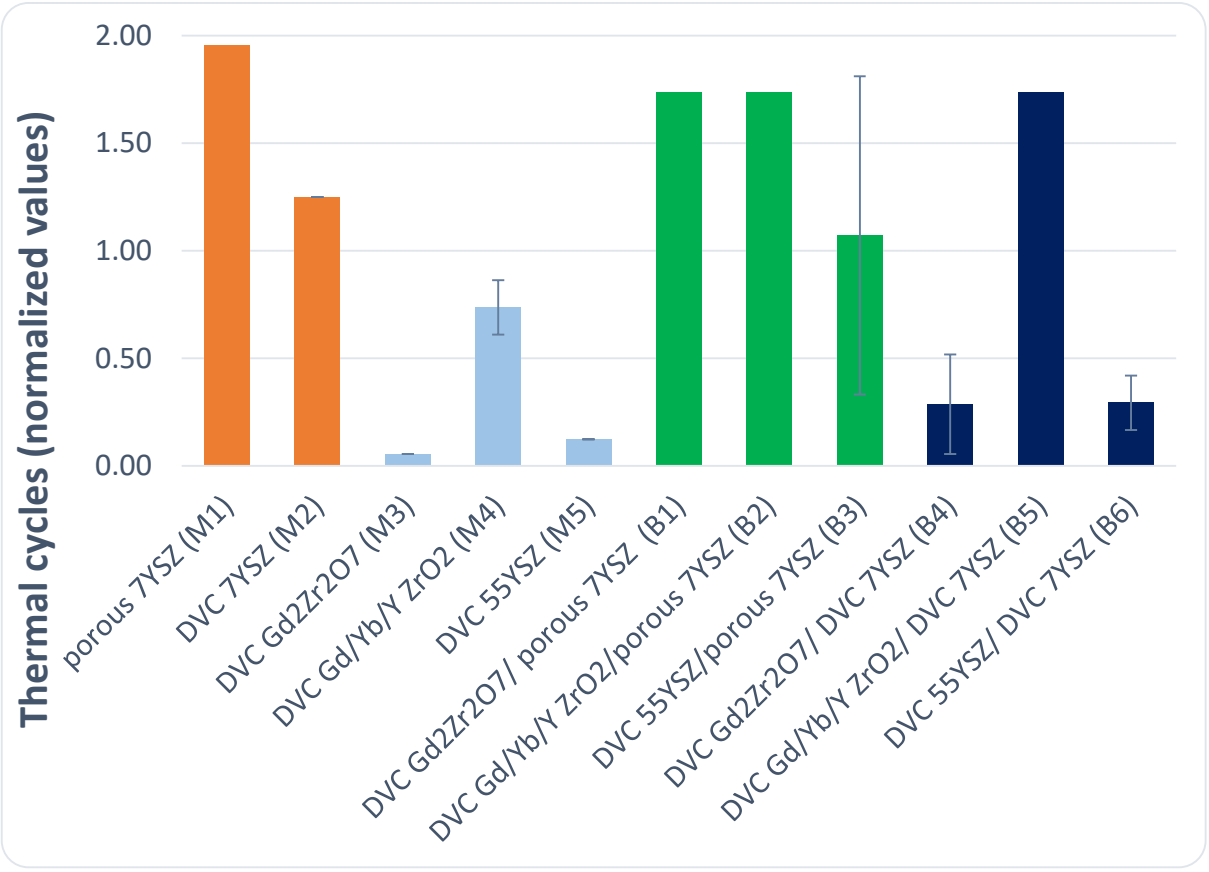

Figure 83 Number of thermal cycles to failure for monolayers (light blue), bilayers with a porous bottom layer (green), bilayers with a DVC bottom layer (blue), and reference 7YSZ samples with porous and DVC microstructures (red). Note that all tests on the $Gd_2Zr_2O_7$/porous 7YSZ (B1), Gd/Yb/Y co-doped ZrO_2/porous 7YSZ (B2) and Gd/Yb/Y co-doped ZrO_2/DVC 7YSZ (B5) samples were stopped after reaching a sufficiently large number of cycles, which is why no error bar appears in the plot [149]

As the more performant samples B1, B2, and B5 did not spall off before the test was interrupted (Figure 84), it was possible to analyze their cross-section and identify the extant damage (Figure 85). In all cases, delamination cracks run close to the interface between the bottom 7YSZ layer and the TGO and/or inside the TGO, following what can be called an "adhesive failure" mode that has been widely documented in the literature and summarized by the present authors in [61]. Cracks start either in the 7YSZ layer, just above the roughness crests of the bond coat, or in the TGO itself, running from one roughness crest to the other across the YSZ layer. Nonetheless, the $Gd_2Zr_2O_7$/porous YSZ sample (Figure 85A, B) also shows delamination cracks inside the 7YSZ layer itself, due to the additional stress imposed by the lower CTE of the top coat.

In general, these findings are consistent with the notion that the best performing among the multilayer coatings are those where the failure location is in proximity to the TGO interface (adhesive failure) rather than within the multilayer ceramic system itself (e.g. between the top and bottom layer) [56].

At higher magnification it is also possible to observe that sintering reduced the amount and size of pores in all layers after exposure at high temperatures (Figure 85B, D, F). The stiffening that comes with sintering contributes to promoting the formation of delamination cracks.

It is also noted that the TGO thickness is greater than the 5 - 6 µm threshold (Figure 86A, B) above which, according to the literature, damage generation and propagation accelerates significantly [59,61,159]. At this threshold, stresses in the TGO indeed become too large for its fracture toughness. Exposing the Al-depleted top region of the bond coat, transition metal oxides are formed which accelerate the growth of the TGO and, at the same time, impair its fracture toughness, further worsening the situation [61]. Indeed, after the thermal exposure, EDX analysis confirms that oxide protrusions based on Cr, Co and Ni were formed (Figure 86: spectrum 1) in addition to the Al, O-based scale (spectrum 3).

It is therefore inferred that, in all the mentioned systems, the 7YSZ bottom layer offers good cohesion with the $Gd_2Zr_2O_7$ and Gd/Yb/Y co-doped top layer so that delamination is controlled by Al-depletion of the bond coat with the growth of transition metal oxides, as in a conventional TBC.

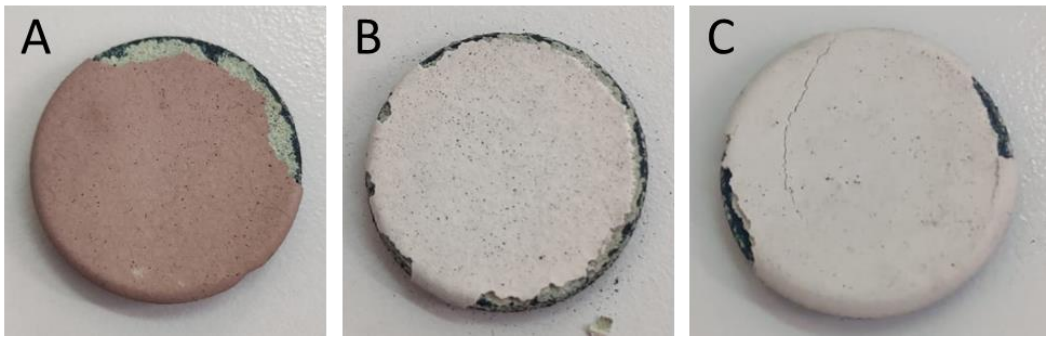

Figure 84 Photographs of thermal cycled samples: A) B1; B) B2; C) B5

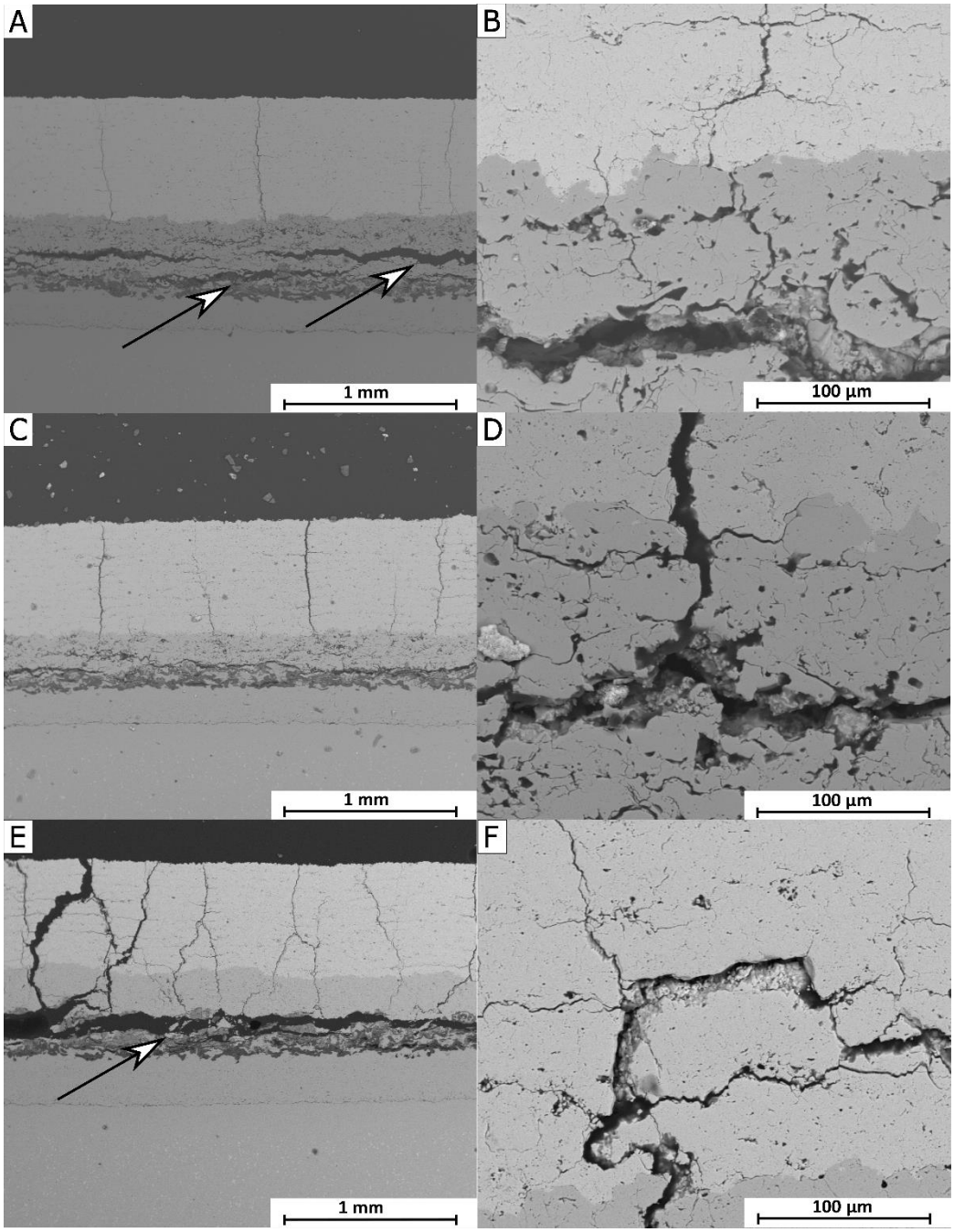

Figure 85 BSE_SEM micrographs obtained after thermal cycling test of sample B1 (A, B); sample B2 (C, D); sample B5 (E, F) [149]

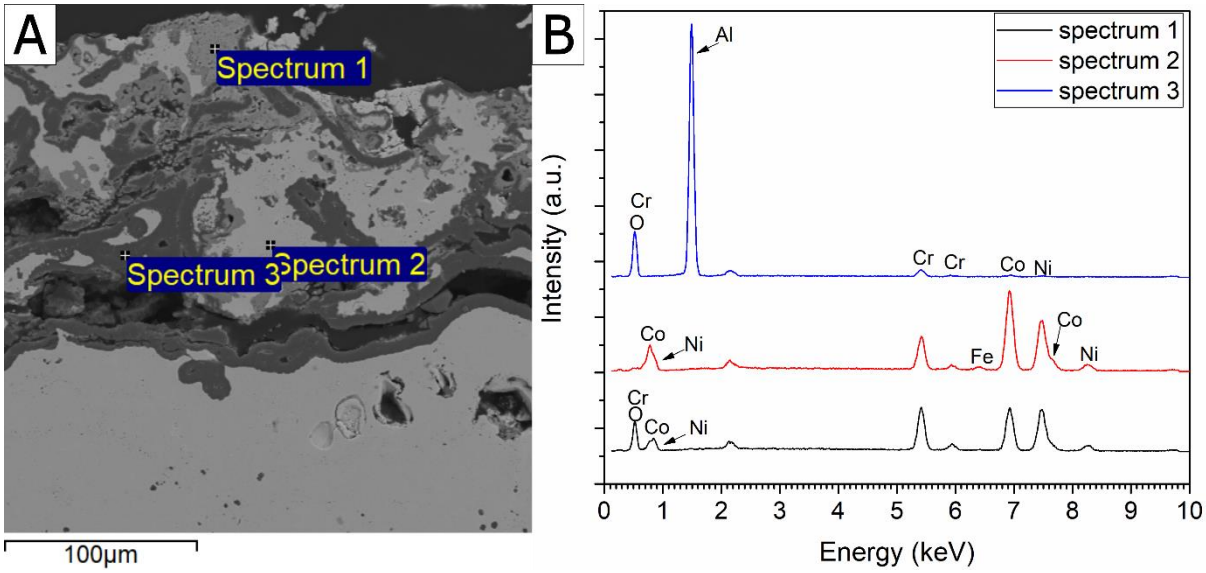

Figure 86 EDX analyses of the TGO layer in sample B5 after thermal cycling fatigue testing [149]

5 Conclusion

This thesis contains two main parts: 1) the first part is focused on the chemical corrosion of plasma-sprayed ZrO_2 + 7-8 wt.% Y_2O_3 (YSZ) thermal barrier coatings (TBCs) by a molten CaO-MgO-Al_2O_3-SiO_2 (CMAS) deposit. The tested TBCs include: two conventional atmospheric plasma-sprayed (APS) samples with standard and high chemical purity YSZ; a dense-vertically cracked (DVC) APS coating; and a suspension plasma sprayed (SPS) coating. The mechanism of dissolution and re-precipitation occur in all samples. Molten CMAS attacks and dissolves preferentially the boundaries among YSZ grains. When the attack is especially extensive, YSZ grains are completely separated from one another and "left afloat" in the molten glass. Dissolution then proceeds from the boundary toward the core of each grain. Yttria-lean zirconia can precipitate from the ZrO_2-saturated melt giving rise to peculiar, globular or fibrous structures. Yttria-lean zirconia precipitates consist of transformable (t) phase at high temperature and undergo martensitic transformation to the monoclinic (m) phase upon cooling to room temperature.

The intensity of the attack is affected by both microstructure and chemical purity of the coatings. In particular, it was found that chemical purity of the feedstock powders plays an important role, affecting the final performances of TBCs.

- When comparing two conventional APS samples having similar porosity, the one with lower chemical purity experienced more severe degradation.

Comparing different microstructures (porous APS, DVC APS and SPS coatings), the following considerations were made:

- In porous APS coatings, fine-grained regions produced by molten YSZ particles are more severely attacked than coarse-grained, unmelted particles.
- Within the dense "islands" of a DVC coating, slight degradation could occur because the large specific surface of the boundaries among fine columnar grains constitutes a preferential site for CMAS attack. The main issue for the DVC-APS sample is, however, the large-scale penetration of CMAS into the segmentation cracks. As CMAS solidifies during cooling, it compromises the compliance of the coating and causes "cold shock".
- The SPS coating experienced by far the most severe degradation. Its main drawbacks under CMAS corrosion are those very features that are generally considered the most desirable in a SPS TBC. Namely, high linear density of inter-columnar gaps, high intra-

columnar porosity, and fine grain size, which are supposed to provide simultaneously high compliance and low thermal conductivity, also favour CMAS corrosion. CMAS penetrates along inter-columnar gaps, infiltrates the abundant intra-columnar porosity, and attacks the boundaries among the YSZ grains, which are much finer even when compared to the DVC coating. Those small grains are thus separated from one another, and the mechanical integrity of the coating is compromised to such an extent that large-scale frothing occurs.

The second part of the thesis was aimed to investigate the resistance to CMAS corrosion (in isothermal conditions) and to thermal cycling fatigue of three novel thermal barrier coating materials, namely $Gd_2Zr_2O_7$, ZrO_2-55wt.% Y_2O_3 and Gd/Yb/Y co-doped ZrO_2. These were obtained both in the form of single, dense-vertically cracked (DVC) layers, plasma sprayed onto an MCrAlY bond coat obtained by HVOF process, and as top layers in bi-layer systems with a bottom layer of ZrO_2-7wt.% Y_2O_3 (7YSZ), having either porous or DVC microstructure. It was found that:

1) $Gd_2Zr_2O_7$ is highly reactive towards the CMAS melt. Initial dissolution of Gd_2O_3, which leaves a layer of Gd-depleted fluorite just behind the $Gd_2Zr_2O_7$/CMAS reaction interface, leads to the precipitation of a solid layer of Gd-apatite, blocking further penetration. This was seen to happen both along the surfaces of the large segmentation cracks of the DVC microstructure, and inside the tiny intra- and inter-lamellar microcracks. Unlike 7YSZ, which suffers extensive grain-boundary dissolution, there is no sign of grain-boundary degradation in the $Gd_2Zr_2O_7$ layer.
2) A similar mechanism is true also for ZrO_2-55wt.% Y_2O_3, with the formation of Y-apatite. Although no sign of grain-boundary corrosion was found inside the coating, the Y-apatite precipitates did not form as continuous a layer along the reaction interface as did the Gd-apatite. Therefore, some grain boundary corrosion took place along the boundaries of the large segmentation cracks. This means that this system might not be equally well resistant to CMAS corrosion as $Gd_2Zr_2O_7$. Therefore, gadolinium zirconate is the most desirable material to maximize CMAS resistance.
3) Gd/Yb/Y co-doped ZrO_2 does not resist CMAS corrosion because it does not develop any interface reaction. Therefore, the CMAS melt attacks and dissolves its grain boundaries at approximately the same rate as it does with 7YSZ.

4) The overall corrosion resistance of the coatings we tested ranks according to the magnitude of the difference between the optical basicity of each composition and that of the CMAS melt. Accordingly, the Gd/Yb/Y co-doped ZrO_2 composition has almost the same optical basicity as 7YSZ.
5) A downside of the $Gd_2Zr_2O_7$ and ZrO_2-55wt.% Y_2O_3 compositions is that, because of their inherent brittleness, they develop a large amount of microcracks even within the dense parts of the DVC microstructure. Although this did not lead to any visible grain-boundary corrosion of the top layer (see point 1), the reaction between the coating material and the CMAS is apparently not able to seal the pores before the CMAS penetrates down to the 7YSZ bottom layer. Especially the porous 7YSZ layer is, therefore, severely attacked by CMAS. This occurrence might undermine the structural integrity of the bi-layer system. However, this might not be too much of a concern in practical applications, because, unlike the present isothermal furnace test, a temperature gradient exists across a TBC as the metal substrate is air-cooled, so that the temperature at the 7YSZ underlayer would likely fall below the CMAS solidification temperature.
6) All the single-layers, and particularly $Gd_2Zr_2O_7$ and ZrO_2-55wt.% Y_2O_3, have very poor thermal cycling fatigue resistance. The use of a 7YSZ bottom layer, especially of a porous one, enhances the thermal cycling fatigue resistance significantly. In particular, the $Gd_2Zr_2O_7$/porous 7YSZ and the Gd/Yb/Y co-doped ZrO_2 with either porous or DVC bottom layers survived all the thermal cycling fatigue tests without spalling off macroscopically. Their damage mechanism seems to be similar to that of a conventional, single-layer 7YSZ TBC, with delamination cracks running at or close to the interface with the TGO layer and no cohesive failure along the interface between the ceramic layers, although delamination cracks within the 7YSZ layer also appeared in the $Gd_2Zr_2O_7$/porous 7YSZ system.

A porous 7YSZ bottom layer would therefore seem advantageous to achieve adequate thermal cycling fatigue resistance for practical use, although it remains to be seen whether this underlayer would be damaged by CMAS penetration under thermal gradient conditions, as mentioned above.

6 Developments

As discussed in Section 1, the proper selection of thermal barrier coatings for aeronautical and industrial gas turbines components is a theme of growing concern. This PhD research was aimed to address this vast topic from the point of view of two of the main degradation mechanisms of TBCs: CMAS corrosion and thermal cycling failure. The work performed during this Ph.D. research is certainly not exhaustive taking in account that there are other mechanisms (e.g. erosion) which can lead to the failure of TBCs. Moreover, other factors (e.g. morphology of the feedstock powders) can affect the TBCs performances. Thus, further researches on TBCs are currently being carried out:

1) *Effect of Powder Morphology on 7-8YSZ TBCs Performances:* The goal of this work is to investigate how Agglomerated and Sintered (A&S), Hollow Spherical (HOSP) and Fused and Crushed (F&C) 7-8YSZ powders affect the performances of Atmospherically Plasma Sprayed (APS) TBCs.

2) *Erosion resistance of 7-8YSZ coatings obtained by APS and SPS process:* This research is focused on the evaluation of the erosion resistance of YSZ TBCs deposited by conventional atmospheric plasma spraying (APS) and suspension plasma spraying (SPS). The latter is a novel, promising technique for the production of fine-structured coatings, but limited information is available on the erosion behaviour of SPS TBCs [160–162], especially when exposed to high temperature. For this purpose, a gas jet erosion rig operated at 950 ± 10 °C with ≈ 45 μm-sized alumina sand at a 2 g/min flow rate and 65 m/s speed was employed for testing the erosion resistance.

References

[1] https://www.grandviewresearch.com/industry-analysis/gas-turbine-market), (n.d.).

[2] https://upload.wikimedia.org/wikipedia/commons/4/4c/Jet_engine.svg, (n.d.).

[3] L.S. Langston, Turbines, Gas, Encycl. Energy. 6 (2004) 221–230. https://doi.org/10.1016/b0-12-176480-x/00098-x.

[4] H.I.H. Saravanamuttoo, H. Cohen, G.F.C. Rogers, A.C. Nix, P. V. Straznicky, Gas Turbine Theory, 7th ed., 2017, ISBN:9781292093093.

[5] M.P. Boyce, Advanced industrial gas turbines for power generation, Elsevier Masson SAS., 2012. https://doi.org/10.1533/9780857096180.44.

[6] T.J. Carter, Common failures in gas turbine blades, Eng. Fail. Anal. 12 (2005) 237–247. https://doi.org/10.1016/j.engfailanal.2004.07.004.

[7] https://www.sulzer.com/en/shared/services/lifetime-assessments, (2022).

[8] J.C. Han, Gas Turbine Heat Transfer and Cooling Technology, 2001, ISBN:0791835332.

[9] D.R. Clarke, M. Oechsner, N.P. Padture, Thermal-barrier coatings for more efficient gas-turbine engines, MRS Bull. 37 (2012) 891–898. https://doi.org/10.1557/mrs.2012.232.

[10] N.P. Padture, M. Gell, E.H. Jordan, Thermal barrier coatings for gas-turbine engine applications, Science (80-.). 296 (2002) 280–284. https://doi.org/10.1126/science.1068609.

[11] C.U. Hardwicke, Y.C. Lau, Advances in thermal spray coatings for gas turbines and energy generation: A review, J. Therm. Spray Technol. 22 (2013) 564–576. https://doi.org/10.1007/s11666-013-9904-0.

[12] S. Bose, High Temperature Coatings, 2007, ISBN:9780750682527. https://doi.org/10.1016/B978-0-7506-8252-7.X5000-8.

[13] R.C. Reed, The Superalloy fundamentals and applications, Cambridge, 2006, ISBN:9789896540821.

[14] M. Gupta, Design of Thermal Barrier Coatings, 2015, ISBN:9783319172538. https://doi.org/10.1007/978-3-319-17254-5.

[15] M. Ahrens, R. Vaßen, D. Stöver, Stress distributions in plasma-sprayed thermal barrier coatings as a function of interface roughness and oxide scale thickness, Surf. Coatings Technol. 161 (2002) 26–35. https://doi.org/10.1016/S0257-8972(02)00359-6.

[16] K.J. Nicholls, J. R.; Lawson, Methods to reduce the thermal conductivity of EB-PVD TBC's, Surf. Coatings Technol. 151–152 (2002) 383–391.

[17] D.P.H. Hasselman, L.F. Johnson, L.D. Bentsen, R. Syed, H.L. Lee, M. V. Swain, Thermal diffusivity and conductivity of dense polycrystalline ZrO_2 ceramics: a survey, Am. Ceram. Soc. Bull. 66 (1987) 799–806.

[18] S. V. Shinde, E.J. Gildersleeve V, C.A. Johnson, S. Sampath, Segmentation crack formation dynamics during air plasma spraying of zirconia, Acta Mater. 183 (2020) 196–206. https://doi.org/10.1016/j.actamat.2019.10.052.

[19] R. Vaßen, E. Bakan, D. Mack, S. Schwartz-Lückge, D. Sebold, Y. Jung Sohn, D. Zhou,

O. Guillon, Performance of YSZ and $Gd_2Zr_2O_7$/YSZ double layer thermal barrier coatings in burner rig tests, J. Eur. Ceram. Soc. 40 (2020) 480–490. https://doi.org/10.1016/j.jeurceramsoc.2019.10.021.

[20] X.Q. Cao, R. Vassen, D. Stoever, Ceramic materials for thermal barrier coatings, J. Eur. Ceram. Soc. 24 (2004) 1–10. https://doi.org/10.1016/S0955-2219(03)00129-8.

[21] R. Vassen, X. Cao, F. Tietz, D. Basu, D. Sto, Zirconates as New Materials for Thermal Barrier Coatings, J. Am. Ceram. Soc. 83 (2004) 2023–2028. https://doi.org/https://doi.org/10.1111/j.1151-2916.2000.tb01506.x.

[22] H. Xu, H. Guo, Thermal barrier coatings, in: Woodhead Publ. Ltd., 2011, ISBN:978-0-85709-082-9.

[23] A.F. Renteria, B. Saruhan, U. Schulz, H.J. Raetzer-Scheibe, J. Haug, A. Wiedenmann, Effect of morphology on thermal conductivity of EB-PVD PYSZ TBCs, Surf. Coatings Technol. 201 (2006) 2611–2620. https://doi.org/10.1016/j.surfcoat.2006.05.003.

[24] R.G. Wellman, M.J. Deakin, J.R. Nicholls, The effect of TBC morphology on the erosion rate of EB PVD TBCs, Wear. 258 (2005) 349–356. https://doi.org/10.1016/j.wear.2004.04.011.

[25] S. Sampath, U. Schulz, M.O. Jarligo, S. Kuroda, Processing science of advanced thermal-barrier systems, MRS Bull. 37 (2012) 903–910. https://doi.org/10.1557/mrs.2012.233.

[26] P. Fauchais, A. Vardelle, Thermal Sprayed Coatings Used Against Corrosion and Corrosive Wear, Adv. Plasma Spray Appl. (2012). https://doi.org/10.5772/34448.

[27] W. Chi, S. Sampath, H. Wang, Microstructure-thermal conductivity relationships for plasma-sprayed yttria-stabilized zirconia coatings, J. Am. Ceram. Soc. 91 (2008) 2636–2645. https://doi.org/10.1111/j.1551-2916.2008.02476.x.

[28] A. Nouri, A. Sola, Powder morphology in thermal spraying, J. Adv. Manuf. Process. 1 (2019) 1–19. https://doi.org/10.1002/amp2.10020.

[29] O.P. Solonenko, I.P. Gulyaev, A. V. Smirnov, Thermal plasma processes for production of hollow spherical powders: Theory and experiment, J. Therm. Sci. Technol. 6 (2011) 219–234. https://doi.org/10.1299/jtst.6.219.

[30] L.M. Berger, Application of hardmetals as thermal spray coatings, Int. J. Refract. Met. Hard Mater. 49 (2015) 350–364. https://doi.org/10.1016/j.ijrmhm.2014.09.029.

[31] P.K. Mehrotra, Powder Processing and Green Shaping, Elsevier Ltd, 2014, ISBN:9780080965284. https://doi.org/10.1016/B978-0-08-096527-7.00007-6.

[32] R.M. German, Consolidation Techniques, Elsevier Ltd, 2014, ISBN:9780080965284. https://doi.org/10.1016/B978-0-08-096527-7.00008-8.

[33] L. Pawlowski, The Science and Engineering of Thermal Spray Coatings: Second Edition, 2008, ISBN:9780471490494. https://doi.org/10.1002/9780470754085.

[34] T.A. Taylor, US Patent No. 5073433, (1991).

[35] D. Chen, C. Dambra, M. Dorfman, Process and properties of dense and porous vertically-cracked yttria stabilized zirconia thermal barrier coatings, Surf. Coatings Technol. 404 (2020) 126467. https://doi.org/10.1016/j.surfcoat.2020.126467.

[36] H. Guo, H. Murakami, S. Kuroda, Effects of heat treatment on microstructures and physical properties of segmented thermal barrier coatings, Mater. Trans. 46 (2005) 1775–1778. https://doi.org/10.2320/matertrans.46.1775.

[37] B. Lv, R. Mücke, X. Fan, T.J. Wang, O. Guillon, R. Vaßen, Sintering resistance of advanced plasma-sprayed thermal barrier coatings with strain-tolerant microstructures, J. Eur. Ceram. Soc. 38 (2018) 5092–5100. https://doi.org/10.1016/j.jeurceramsoc.2018.07.013.

[38] M.I. Boulos, P.L. Fauchais, J.V.R. Heberlein, Thermal Spray Fundamentals, Therm. Spray Fundam. (2021). https://doi.org/10.1007/978-3-030-70672-2.

[39] F. Tarasi, M. Medraj, A. Dolatabadi, J. Oberste-Berghaus, C. Moreau, Effective parameters in axial injection suspension plasma spray process of alumina-zirconia ceramics, J. Therm. Spray Technol. 17 (2008) 685–691. https://doi.org/10.1007/s11666-008-9259-0.

[40] L. Pawlowski, Suspension and solution thermal spray coatings, Surf. Coatings Technol. 203 (2009) 2807–2829. https://doi.org/10.1016/j.surfcoat.2009.03.005.

[41] A. Ganvir, R.F. Calinas, N. Markocsan, N. Curry, S. Joshi, Experimental visualization of microstructure evolution during suspension plasma spraying of thermal barrier coatings, J. Eur. Ceram. Soc. 39 (2019) 470–481. https://doi.org/10.1016/j.jeurceramsoc.2018.09.023.

[42] L. Łatka, Thermal Barrier Coatings Manufactured by Suspension Plasma Spraying - A Review, Adv. Mater. Sci. 18 (2018) 95–117. https://doi.org/10.1515/adms-2017-0044.

[43] P.G. Lashmi, P. V. Ananthapadmanabhan, G. Unnikrishnan, S.T. Aruna, Present status and future prospects of plasma sprayed multilayered thermal barrier coating systems, J. Eur. Ceram. Soc. 40 (2020) 2731–2745. https://doi.org/10.1016/j.jeurceramsoc.2020.03.016.

[44] N. Curry, K. VanEvery, T. Snyder, J. Susnjar, S. Bjorklund, Performance testing of suspension plasma sprayed thermal barrier coatings produced with varied suspension parameters, Coatings. 5 (2015) 338–356. https://doi.org/10.3390/coatings5030338.

[45] S. Mahade, N. Curry, S. Björklund, N. Markocsan, P. Nylén, Thermal conductivity and thermal cyclic fatigue of multilayered Gd_2/Zr_2O_7/YSZ thermal barrier coatings processed by suspension plasma spray, Surf. Coatings Technol. 283 (2015) 329–336. https://doi.org/10.1016/j.surfcoat.2015.11.009.

[46] M. Goral, S. Kotowski, A. Nowotnik, M. Pytel, M. Drajewicz, J. Sieniawski, PS-PVD deposition of thermal barrier coatings, Surf. Coatings Technol. 237 (2013) 51–55. https://doi.org/10.1016/j.surfcoat.2013.09.028.

[47] M. Goral, S. Kotowski, J. Sieniawski, The technology of plasma spray physical vapour deposition, High Temp. Mater. Process. 32 (2013) 33–39. https://doi.org/10.1515/htmp-2012-0051.

[48] K. Von Niessen, M. Gindrat, Vapor phase deposition using a plasma spray process, J. Eng. Gas Turbines Power. 133 (2011) 1–7. https://doi.org/10.1115/1.4002469.

[49] G. Mauer, A. Hospach, N. Zotov, R. Vaßen, Process conditions and microstructures of ceramic coatings by gas phase deposition based on plasma spraying, J. Therm. Spray Technol. 22 (2013) 83–89. https://doi.org/10.1007/s11666-012-9838-y.

[50] R. Kurz, K. Brun, Gas turbine tutorial–Maintenance and operating practices effects on degradation and life, Proc. 36th Turbomach. (2007) 173–186.

[51] L. Steinberg, R. Naraparaju, M. Heckert, C. Mikulla, U. Schulz, C. Leyens, Erosion behavior of EB-PVD 7YSZ coatings under corrosion/erosion regime: Effect of TBC microstructure and the CMAS chemistry, J. Eur. Ceram. Soc. 38 (2018) 5101–5112. https://doi.org/10.1016/j.jeurceramsoc.2018.06.039.

[52] J.R. Nicholls, M.J. Deakin, D.S. Rickerby, A comparison between the erosion behaviour of thermal spray and electron beam physical vapour deposition thermal barrier coatings, Wear. 233–235 (1999) 352–361. https://doi.org/10.1016/S0043-1648(99)00214-8.

[53] H.E. Eaton, R.C. Novak, Particulate erosion of plasma-sprayed porous ceramic, Surf. Coatings Technol. 30 (1987) 41–50. https://doi.org/10.1016/0257-8972(87)90006-5.

[54] R.G. Wellman, J.R. Nicholls, A review of the erosion of thermal barrier coatings, J. Phys. D. Appl. Phys. 40 (2007). https://doi.org/10.1088/0022-3727/40/16/R01.

[55] C.G. Levi, J.W. Hutchinson, M.H. Vidal-Sétif, C.A. Johnson, Environmental degradation of thermal-barrier coatings by molten deposits, MRS Bull. 37 (2012) 932–941. https://doi.org/10.1557/mrs.2012.230.

[56] V. Viswanathan, G. Dwivedi, S. Sampath, Multilayer, multimaterial thermal barrier coating systems: Design, synthesis, and performance assessment, J. Am. Ceram. Soc. 98 (2015) 1769–1777. https://doi.org/10.1111/jace.13563.

[57] G. Dwivedi, V. Viswanathan, S. Sampath, A. Shyam, E. Lara-Curzio, Fracture toughness of plasma-sprayed thermal barrier ceramics: Influence of processing, microstructure, and thermal aging, J. Am. Ceram. Soc. 97 (2014) 2736–2744. https://doi.org/10.1111/jace.13021.

[58] D.R. Mumm, G.A. Evans, Mechanisms controlling the performance and durability of thermal barrier coatings, Key Eng. Mater. 197 (2001) 199–230. https://doi.org/10.4028/www.scientific.net/kem.197.199.

[59] H. Dong, G.J. Yang, C.X. Li, X.T. Luo, C.J. Li, Effect of TGO thickness on thermal cyclic lifetime and failure mode of plasma-sprayed TBCs, J. Am. Ceram. Soc. 97 (2014) 1226–1232. https://doi.org/10.1111/jace.12868.

[60] C. Giolli, A. Scrivani, G. Rizzi, F. Borgioli, G. Bolelli, L. Lusvarghi, Failure mechanism for thermal fatigue of thermal barrier coating systems, J. Therm. Spray Technol. 18 (2009) 223–230. https://doi.org/10.1007/s11666-009-9307-4.

[61] G. Bolelli, M.G. Righi, M.Z. Mughal, R. Moscatelli, O. Ligabue, N. Antolotti, M. Sebastiani, L. Lusvarghi, E. Bemporad, Damage progression in thermal barrier coating systems during thermal cycling: A nano-mechanical assessment, Mater. Des. 166 (2019) 107615. https://doi.org/10.1016/j.matdes.2019.107615.

[62] X.C. Zhang, B.S. Xu, H.D. Wang, Y.X. Wu, Effects of oxide thickness, Al_2O_3 interlayer and interface asperity on residual stresses in thermal barrier coatings, Mater. Des. 27 (2006) 989–996. https://doi.org/10.1016/j.matdes.2005.02.008.

[63] M. Martena, D. Botto, P. Fino, S. Sabbadini, M.M. Gola, C. Badini, Modelling of TBC system failure: Stress distribution as a function of TGO thickness and thermal expansion mismatch, Eng. Fail. Anal. 13 (2006) 409–426. https://doi.org/10.1016/j.engfailanal.2004.12.027.

[64] M. Jinnestrand, S. Sjöström, Investigation by 3D FE simulations of delamination crack initiation in TBC caused by alumina growth, Surf. Coatings Technol. 135 (2001) 188–195. https://doi.org/10.1016/S0257-8972(00)01084-7.

[65] A. Rabiei, A.G. Evans, Failure mechanisms associated with the thermally grown oxide in plasma-sprayed thermal barrier coatings, Acta Mater. 48 (2000) 3963–3976. https://doi.org/10.1016/S1359-6454(00)00171-3.

[66] M. Madhwal, E.H. Jordan, M. Gell, Failure mechanisms of dense vertically-cracked thermal barrier coatings, Mater. Sci. Eng. A. 384 (2004) 151–161. https://doi.org/10.1016/j.msea.2004.05.061.

[67] R. Vaßen, F. Cernuschi, G. Rizzi, A. Scrivani, N. Markocsan, L. Ostergren, A. Kloosterman, R. Mevrel, J. Feist, J. Nicholls, Recent activities in the field of thermal barrier coatings including burner rig testing in the european union., Adv. Eng. Mater. 10 (2008) 907–921. https://doi.org/10.1002/adem.200800015.

[68] R. Eriksson, H. Brodin, S. Johansson, L. Östergren, X.H. Li, Influence of isothermal and cyclic heat treatments on the adhesion of plasma sprayed thermal barrier coatings, Surf. Coatings Technol. 205 (2011) 5422–5429. https://doi.org/10.1016/j.surfcoat.2011.06.007.

[69] S. Rezanka, G. Mauer, R. Vaßen, Improved thermal cycling durability of thermal barrier coatings manufactured by PS-PVD, J. Therm. Spray Technol. 23 (2014) 182–189. https://doi.org/10.1007/s11666-013-9971-2.

[70] N. Curry, Z. Tang, N. Markocsan, P. Nylén, Influence of bond coat surface roughness on the structure of axial suspension plasma spray thermal barrier coatings - Thermal and lifetime performance, Surf. Coatings Technol. 268 (2015) 15–23. https://doi.org/10.1016/j.surfcoat.2014.08.067.

[71] B. Bernard, A. Quet, L. Bianchi, V. Schick, A. Joulia, A. Malié, B. Rémy, Effect of Suspension Plasma-Sprayed YSZ Columnar Microstructure and Bond Coat Surface Preparation on Thermal Barrier Coating Properties, J. Therm. Spray Technol. 26 (2017) 1025–1037. https://doi.org/10.1007/s11666-017-0584-z.

[72] N. Kumar, M. Gupta, D.E. Mack, G. Mauer, R. Vaßen, Columnar Thermal Barrier Coatings Produced by Different Thermal Spray Processes, J. Therm. Spray Technol. 30 (2021) 1437–1452. https://doi.org/10.1007/s11666-021-01228-5.

[73] G. Mauer, R. Vaßen, Coatings with Columnar Microstructures for Thermal Barrier Applications, Adv. Eng. Mater. 22 (2020) 1–9. https://doi.org/10.1002/adem.201900988.

[74] E. Bakan, R. Vaßen, Ceramic Top Coats of Plasma-Sprayed Thermal Barrier Coatings: Materials, Processes, and Properties, J. Therm. Spray Technol. 26 (2017) 992–1010. https://doi.org/10.1007/s11666-017-0597-7.

[75] A. Guignard, G. Mauer, R. Vaßen, D. Stöver, Deposition and characteristics of submicrometer-structured thermal barrier coatings by suspension plasma spraying, J. Therm. Spray Technol. 21 (2012) 416–424. https://doi.org/10.1007/s11666-012-9762-1.

[76] R. Darolia, Thermal barrier coatings technology : critical review , progress update , remaining challenges and Thermal barrier coatings technology : critical review , progress update , remaining challenges and prospects, 2016, ISBN:0000000019.

https://doi.org/10.1179/1743280413Y.0000000019.

[77] A. Bacciochini, F. Ben-Ettouil, E. Brousse, J. Ilavsky, G. Montavon, A. Denoirjean, S. Valette, P. Fauchais, Quantification of void networks of as-sprayed and annealed nanostructured yttria-stabilized zirconia (YSZ) deposits manufactured by suspension plasma spraying, Surf. Coatings Technol. 205 (2010) 683–689. https://doi.org/10.1016/j.surfcoat.2010.06.013.

[78] V. Lughi, V.K. Tolpygo, D.R. Clarke, Microstructural aspects of the sintering of thermal barrier coatings, Mater. Sci. Eng. 368 (2004) 212–221. https://doi.org/10.1016/j.msea.2003.11.018.

[79] F. Cernuschi, L. Lorenzoni, S. Ahmaniemi, P. Vuoristo, T. Mäntylä, Studies of the sintering kinetics of thick thermal barrier coatings by thermal diffusivity measurements, J. Eur. Ceram. Soc. 25 (2005) 393–400. https://doi.org/10.1016/j.jeurceramsoc.2004.01.009.

[80] M.H. Vidal-Setif, N. Chellah, C. Rio, C. Sanchez, O. Lavigne, Calcium-magnesium-alumino-silicate (CMAS) degradation of EB-PVD thermal barrier coatings: Characterization of CMAS damage on ex-service high pressure blade TBCs, Surf. Coatings Technol. 208 (2012) 39–45. https://doi.org/10.1016/j.surfcoat.2012.07.074.

[81] M.P. Borom, C.A. Johnson, L.A. Peluso, Role of environmental deposits and operating surface temperature in spallation of air plasma sprayed thermal barrier coatings, Surf. Coatings Technol. 86–87 (1996) 116–126. https://doi.org/10.1016/S0257-8972(96)02994-5.

[82] R. Naraparaju, U. Schulz, P. Mechnich, P. Döbber, F. Seidel, Degradation study of 7wt.% yttria stabilised zirconia (7YSZ) thermal barrier coatings on aero-engine combustion chamber parts due to infiltration by different CaO-MgO-Al_2O_3-SiO_2 variants, Surf. Coatings Technol. 260 (2014) 73–81. https://doi.org/10.1016/j.surfcoat.2014.08.079.

[83] P. Mechnich, W. Braue, Solid-state CMAS corrosion of an EB-PVD YSZ coated turbine blade: Zr^{4+} partitioning and phase evolution, J. Am. Ceram. Soc. 98 (2015) 296–302. https://doi.org/10.1111/jace.13241.

[84] J.L. Smialek, F.A. Archer, R.G. Garlick, The Chemistry of Saudi Arabian sand: a deposition problem on helicopter turbine airfoils, in: Int. SAMPE Met. Met. Process. Conf., 1992, ISBN:0938994662: pp. 63–77.

[85] W. Braue, P. Mechnich, Recession of an EB-PVD YSZ coated turbine blade by $CaSO_4$ and Fe, Ti-Rich CMAS-Type deposits, J. Am. Ceram. Soc. 94 (2011) 4483–4489. https://doi.org/10.1111/j.1551-2916.2011.04747.x.

[86] R.G. Wellman, J.R. Nicholls, Erosion, corrosion and erosion-corrosion of EB PVD thermal barrier coatings, Tribol. Int. 41 (2008) 657–662. https://doi.org/10.1016/j.triboint.2007.10.004.

[87] R. Wellman, G. Whitman, J.R. Nicholls, CMAS corrosion of EB PVD TBCs: Identifying the minimum level to initiate damage, Int. J. Refract. Met. Hard Mater. 28 (2010) 124–132. https://doi.org/10.1016/j.ijrmhm.2009.07.005.

[88] Z. Chen, H. Zheng, G. Li, H. Li, P. Peng, Mechanism of crack nucleation and growth in YSZ thermal barrier coatings corroded by CMAS at high temperatures: First-principles

calculation, Corros. Sci. 142 (2018) 258–265. https://doi.org/10.1016/j.corsci.2018.07.033.

[89] E. Gildersleeve, V. Viswanathan, S. Sampath, Molten silicate interactions with plasma sprayed thermal barrier coatings: Role of materials and microstructure, J. Eur. Ceram. Soc. 39 (2019) 2122–2131. https://doi.org/10.1016/j.jeurceramsoc.2019.01.023.

[90] D.E. Mack, T. Wobst, M.O.D. Jarligo, D. Sebold, R. Vaßen, Lifetime and failure modes of plasma sprayed thermal barrier coatings in thermal gradient rig tests with simultaneous CMAS injection, Surf. Coatings Technol. 324 (2017) 36–47. https://doi.org/10.1016/j.surfcoat.2017.04.071.

[91] C. Mercer, S. Faulhaber, A.G. Evans, R. Darolia, A delamination mechanism for thermal barrier coatings subject to calcium-magnesium-alumino-silicate (CMAS) infiltration, Acta Mater. 53 (2005) 1029–1039. https://doi.org/10.1016/j.actamat.2004.11.028.

[92] H. Zhao, C.G. Levi, H.N.G. Wadley, Molten silicate interactions with thermal barrier coatings, Surf. Coatings Technol. 251 (2014) 74–86. https://doi.org/10.1016/j.surfcoat.2014.04.007.

[93] C.G. Levi, J.W. Hutchinson, A.G. Evans, Mechanisms of cracking and delamination within thick thermal barrier systems in aero-engines subject to calcium-magnesium-alumino-silicate (CMAS) penetration, Mater. Sci. Eng. 490 (2008) 26–35. https://doi.org/10.1016/j.msea.2008.01.006.

[94] X. Shan, Z. Zou, L. Gu, L. Yang, F. Guo, X. Zhao, P. Xiao, Buckling failure in air-plasma sprayed thermal barrier coatings induced by molten silicate attack, Scr. Mater. 113 (2016) 71–74. https://doi.org/10.1016/j.scriptamat.2015.09.029.

[95] F.H.. Stott, D.J.. de Wet, R. Taylor, The effects of molten silicate deposits on the stability of thermal barrier coatings for turbine applications at very high temperatures, in: Int. SAMPE Met. Met. Process. Conf., 1992.

[96] E. Bohorquez, B. Sarley, J. Hernandez, R. Hoover, L. Tetard, R. Naraparaju, U. Schulz, S. Raghavan, Investigation of the effects of CMAS-infiltration in EB-PVD 7% yttria-stabilized Zirconia via Raman spectroscopy, in: AIAA/ASCE/AHS/ASC Struct. Struct. Dyn. Mater. Conf. 2018, 2018, ISBN:9781624105326: pp. 1–6. https://doi.org/10.2514/6.2018-0096.

[97] B. Zhang, W. Song, H. Guo, Wetting, infiltration and interaction behavior of CMAS towards columnar YSZ coatings deposited by plasma spray physical vapor, J. Eur. Ceram. Soc. 38 (2018) 3564–3572. https://doi.org/10.1016/j.jeurceramsoc.2018.04.013.

[98] S. Krämer, J. Yang, C.G. Levi, C.A. Johnson, Thermochemical interaction of thermal barrier coatings with molten CaO-MgO-Al_2O_3-SiO_2 (CMAS) deposits, J. Am. Ceram. Soc. 89 (2006) 3167–3175. https://doi.org/10.1111/j.1551-2916.2006.01209.x.

[99] J. Xia, L. Yang, R.T. Wu, Y.C. Zhou, L. Zhang, K.L. Huo, M. Gan, Degradation mechanisms of air plasma sprayed free-standing yttria-stabilized zirconia thermal barrier coatings exposed to volcanic ash, Appl. Surf. Sci. 481 (2019) 860–871. https://doi.org/10.1016/j.apsusc.2019.03.084.

[100] A. Nieto, M. Walock, Calcia-Magnesia-Alumina-Silicate (CMAS) Infiltration Behavior in High Temperature Ceramics and Coatings, in: 2018 Jt. Propuls. Conf., 2018, ISBN:9781624105708: pp. 1–12. https://doi.org/10.2514/6.2018-4833.

[101] J.A. Krogstad, S. Krämer, D.M. Lipkin, C.A. Johnson, D.R.G. Mitchell, J.M. Cairney, C.G. Levi, Phase stability of t′-zirconia-based thermal barrier coatings: Mechanistic insights, J. Am. Ceram. Soc. 94 (2011) 168–177. https://doi.org/10.1111/j.1551-2916.2011.04531.x.

[102] H. Peng, L. Wang, L. Guo, W. Miao, H. Guo, S. Gong, Degradation of EB-PVD thermal barrier coatings caused by CMAS deposits, Prog. Nat. Sci. Mater. Int. 22 (2012) 461–467. https://doi.org/10.1016/j.pnsc.2012.06.007.

[103] Z. Cai, J. Jiang, W. Wang, Y. Liu, Z. Cao, CMAS penetration-induced cracking behavior in the ceramic top coat of APS TBCs, Ceram. Int. 45 (2019) 14366–14375. https://doi.org/10.1016/j.ceramint.2019.04.152.

[104] W. Li, H. Zhao, X. Zhong, L. Wang, S. Tao, Air plasma-sprayed yttria and yttria-stabilized zirconia thermal barrier coatings subjected to calcium-magnesium-alumino-silicate (CMAS), J. Therm. Spray Technol. 23 (2014) 975–983. https://doi.org/10.1007/s11666-014-0107-0.

[105] A. Nieto, R. Agrawal, L. Bravo, C. Hofmeister-Mock, M. Pepi, A. Ghoshal, Calcia–magnesia–alumina–silicate (CMAS) attack mechanisms and roadmap towards Sandphobic thermal and environmental barrier coatings, Int. Mater. Rev. 66 (2021) 451–492. https://doi.org/10.1080/09506608.2020.1824414.

[106] S. Rezanka, D.E. Mack, G. Mauer, D. Sebold, O. Guillon, R. Vaßen, Investigation of the resistance of open-column-structured PS-PVD TBCs to erosive and high-temperature corrosive attack, Surf. Coatings Technol. 324 (2017) 222–235. https://doi.org/10.1016/j.surfcoat.2017.05.003.

[107] L. Li, N. Hitchman, J. Knapp, Failure of thermal barrier coatings subjected to CMAS attack, J. Therm. Spray Technol. 19 (2010) 148–155. https://doi.org/10.1007/s11666-009-9356-8.

[108] Z. Tian, J. Zhang, L. Zheng, W. Hu, X. Ren, Y. Lei, J. Wang, General trend on the phase stability and corrosion resistance of rare earth monosilicates to molten calcium–magnesium–alumino silicate at 1300 °C, Corros. Sci. 148 (2019) 281–292. https://doi.org/10.1016/j.corsci.2018.12.032.

[109] A.R. Krause, B.S. Senturk, H.F. Garces, G. Dwivedi, A.L. Ortiz, S. Sampath, N.P. Padture, $2ZrO_2{\cdot}Y_2O_3$ thermal barrier coatings resistant to degradation by molten CMAS: Part I, Optical basicity considerations and processing, J. Am. Ceram. Soc. 97 (2014) 3943–3949. https://doi.org/10.1111/jace.13210.

[110] J.A. Duffy, Optical Basicity: A Practical Acid-Base Theory for Oxides and Oxyanions, J. Chem. Educ. 73 (1996) 1138. https://doi.org/10.1021/ed073p1138.

[111] W.R. Chen, L.R. Zhao, Review - Volcanic Ash and its Influence on Aircraft Engine Components, Procedia Eng. 99 (2015) 795–803. https://doi.org/10.1016/j.proeng.2014.12.604.

[112] R. Vaßen, M.O. Jarligo, T. Steinke, D.E. Mack, D. Stöver, Overview on advanced thermal barrier coatings, Surf. Coatings Technol. 205 (2010) 938–942. https://doi.org/10.1016/j.surfcoat.2010.08.151.

[113] D. Zhu, R.A. Miller, Development of advanced low conductivity thermal barrier coatings, Int. J. Appl. Ceram. Technol. 1 (2004) 86–94. https://doi.org/10.1111/j.1744-

7402.2004.tb00158.x.

[114] D. Zhu, J.A. Nesbitt, C.A. Barrett, T.R. McCue, R.A. Miller, Furnace Cyclic Oxidation Behavior of Multicomponent Low Conductivity Thermal Barrier Coatings, J. Therm. Spray Technol. 13 (2004) 84–92. https://doi.org/10.1361/10599630418185.

[115] H. Fang, W. Wang, J. Huang, Y. Li, D. Ye, Corrosion behavior and thermos-physical properties of a promising Yb_2O_3 and Y_2O_3 co-stabilized ZrO_2 ceramic for thermal barrier coatings subject to calcium-magnesium-aluminum-silicate (CMAS) depositio, Corros. Sci. 182 (2021).

[116] L. Cai, W. Ma, B. Ma, F. Guo, W. Chen, H. Dong, Y. Shuang, Air Plasma-Sprayed $La_2Zr_2O_7SrZrO_3$ Composite Thermal Barrier Coating Subjected to CaO-MgO-Al_2O_3-SiO_2 (CMAS), J. Therm. Spray Technol. 26 (2017) 1076–1083. https://doi.org/10.1007/s11666-017-0587-9.

[117] J. Zeng, J. Sun, P. Liang, X. Yang, S. Dong, J. Jiang, L. Deng, X. Zhou, X. Cao, Heat-treated lanthanum magnesium hexaaluminate coatings exposed to molten calcium-magnesium-alumino-silicate, Ceram. Int. 45 (2019) 11723–11733. https://doi.org/10.1016/j.ceramint.2019.03.048.

[118] J. Wu, N.P. Padture, P.G. Klemens, M. Gell, E. García, P. Miranzo, M.I. Osendi, Thermal conductivity of ceramics in the ZrO_2-$GdO_{1.5}$ system, J. Mater. Res. 17 (2002) 3193–3200. https://doi.org/10.1557/JMR.2002.0462.

[119] J. Lian, L. Wang, J. Chen, K. Sun, R.C. Ewing, J.M. Farmer, L.A. Boatner, The order-disorder transition in ion-irradiated pyrochlore, Acta Mater. 51 (2003) 1493–1502. https://doi.org/10.1016/S1359-6454(02)00544-X.

[120] R.M. Leckie, S. Krämer, M. Rühle, C.G. Levi, Thermochemical compatibility between alumina and ZrO_2-$GdO_{3/2}$ thermal barrier coatings, Acta Mater. 53 (2005) 3281–3292. https://doi.org/10.1016/j.actamat.2005.03.035.

[121] L. Guo, M. Li, C. Zhang, X. Huang, F. Ye, Dy_2O_3 stabilized ZrO_2 as a toughening agent for $Gd_2Zr_2O_7$ ceramic, Mater. Lett. 188 (2017) 142–144. https://doi.org/10.1016/j.matlet.2016.11.038.

[122] M.P. Schmitt, J.L. Stokes, B.L. Gorin, A.K. Rai, D. Zhu, T.J. Eden, D.E. Wolfe, Effect of Gd content on mechanical properties and erosion durability of sub-stoichiometric $Gd_2Zr_2O_7$, Surf. Coatings Technol. 313 (2017) 177–183. https://doi.org/10.1016/j.surfcoat.2016.12.045.

[123] H. Wang, A. Bakal, X. Zhang, E. Tarwater, Z. Sheng, J.W. Fergus, CaO-MgO-Al_2O_3-SiO_2 (CMAS) Corrosion of $Gd_2Zr_2O_7$ and $Sm_2Zr_2O_7$, J. Electrochem. Soc. 163 (2016) C643–C648. https://doi.org/10.1149/2.0301610jes.

[124] P. Carpio, M.D. Salvador, A. Borrell, E. Sánchez, Thermal behaviour of multilayer and functionally-graded YSZ/$Gd_2Zr_2O_7$ coatings, Ceram. Int. 43 (2017) 4048–4054. https://doi.org/10.1016/j.ceramint.2016.11.178.

[125] H. Guo, Y. Wang, L. Wang, S. Gong, Thermo-physical properties and thermal shock resistance of segmented $La_2Ce_2O_7$/YSZ thermal barrier coatings, J. Therm. Spray Technol. 18 (2009) 665–671. https://doi.org/10.1007/s11666-009-9350-1.

[126] R. Vaßen, F. Traeger, D. Stöver, New Thermal Barrier Coatings Based on Pyrochlore / YSZ Double-Layer Systems, Int. J. Appl. Ceram. Technol. 61 (2004) 351–361.

[127] J. Wilden, A. Wank, Application study on ceria based thermal barrier coatings, Materwiss. Werksttech. 32 (2001) 654–659. https://doi.org/10.1002/1521-4052(200108)32:8<654::AID-MAWE654>3.0.CO;2-4.

[128] P.F. Mensah, R. Diwan, S. Nandlkolla, O. Coker, P. Sahoo, Thermo-mechanical study of ther role of $Gd_2Zr_2O_7$ (GZ) in improving life of YSZ abd GZ double layered thermal barrier coatings, Proc. ASME Int. Mech. Eng. Congr. Expo. (2012).

[129] E. Bakan, D.E. Mack, G. Mauer, R. Mücke, R. Vaßen, Porosity-Property Relationships of Plasma-Sprayed $Gd_2Zr_2O_7$/YSZ Thermal Barrier Coatings, J. Am. Ceram. Soc. 98 (2015) 2647–2654. https://doi.org/10.1111/jace.13611.

[130] S. Mahade, D. Zhou, N. Curry, N. Markocsan, P. Nylén, R. Vaßen, Tailored microstructures of gadolinium zirconate/YSZ multi-layered thermal barrier coatings produced by suspension plasma spray: Durability and erosion testing, J. Mater. Process. Technol. 264 (2019) 283–294. https://doi.org/10.1016/j.jmatprotec.2018.09.016.

[131] R. Wang, T. shun Dong, H. dou Wang, Y. lan Di, G. lu Li, Y. Feng, CMAS corrosion resistance in high temperature and rainwater environment of double-layer thermal barrier coatings odified by rare earth, Ceram. Int. 45 (2019) 17409–17419. https://doi.org/10.1016/j.ceramint.2019.05.301.

[132] Y. Ozgurluk, A.C. Karaoglanli, H. Ahlatci, Comparison of calcium–magnesium-alumina-silicate (CMAS) resistance behavior of produced with electron beam physical vapor deposition (EB-PVD) method YSZ and $Gd_2Zr_2O_7$/YSZ thermal barrier coatings systems, Vacuum. 194 (2021) 110576. https://doi.org/10.1016/j.vacuum.2021.110576.

[133] R. Chidambaram Seshadri, S. Sampath, Characteristics of Conventional and Cascaded Arc Plasma Spray-Deposited Ceramic Under Standard and High-Throughput Conditions, J. Therm. Spray Technol. 28 (2019) 690–705. https://doi.org/10.1007/s11666-019-00841-9.

[134] J.-L. Marques, G. Forster, J. Schein, Multi-Electrode Plasma Torches: Motivation for Development and Current State-of-the-Art, Open Plasma Phys. J. 2 (2009) 89–98. https://doi.org/10.2174/1876534300902020089.

[135] S. Morelli, V. Testa, G. Bolelli, O. Ligabue, E. Molinari, N. Antolotti, L. Lusvarghi, CMAS corrosion of YSZ thermal barrier coatings obtained by different thermal spray processes, J. Eur. Ceram. Soc. 40 (2020) 4084–4100. https://doi.org/10.1016/j.jeurceramsoc.2020.04.058.

[136] W.J. Boettinger, U.R. Kattner, K.-W. Moon, J.H. Perepezko, Dta and Heat-Flux Dsc Measurements of Alloy Melting and Freezing, 2007, ISBN:9780080446295. https://doi.org/10.1016/b978-008044629-5/50005-7.

[137] Y. Wu, H. Luo, C. Cai, Y. Wang, Y. Zhou, L. Yang, G. Zhou, Comparison of CMAS corrosion and sintering induced microstructural characteristics of APS thermal barrier coatings, J. Mater. Sci. Technol. 35 (2019) 440–447. https://doi.org/10.1016/j.jmst.2018.09.046.

[138] M. Ohring, The material science of thin films, 2002, ISBN:012524990X.

[139] A.J. Schwartz, M. Kumar, D.P. Field, B.L. Adams, eds., Electron Backscatter Diffraction in Materials Science, Springer, 2013, ISBN:978-0-387-88135-5. https://doi.org/10.1007/978-0-387-88136-2.

[140] R. Vaßen, N. Czech, W. Malléner, W. Stamm, D. Stöver, Influence of impurity content and porosity of plasma-sprayed yttria-stabilized zirconia layers on the sintering behaviour, Surf. Coatings Technol. 141 (2001) 135–140. https://doi.org/10.1016/S0257-8972(01)01269-5.

[141] H.E. Eaton, R.C. Novak, Sintering studies of plasma-sprayed zirconia, Surf. Coatings Technol. 32 (1987) 227–236. https://doi.org/10.1016/0257-8972(87)90109-5.

[142] N. Curry, W. Janikowski, Z. Pala, M. Vilémová, N. Markocsan, Impact of impurity content on the sintering resistance and phase stability of dysprosia- and yttria-stabilized zirconia thermal barrier coatings, J. Therm. Spray Technol. 23 (2014) 160–169. https://doi.org/10.1007/s11666-013-0014-9.

[143] M.A. Helminiak, N.M. Yanar, F.S. Pettit, T.A. Taylor, G.H. Meier, Factors affecting the microstructural stability and durability of thermal barrier coatings fabricated by air plasma spraying, Mater. Corros. 63 (2012) 929–939. https://doi.org/10.1002/maco.201206646.

[144] F.H. Stott, D.J. De Wet, R. Taylor, Degradation of Thermal-Barrier Coatings at Very High Temperatures, MRS Bull. 19 (1994) 46–49. https://doi.org/10.1557/S0883769400048223.

[145] D.E. Mack, R. Laquai, B. Müller, O. Helle, D. Sebold, R. Vaßen, G. Bruno, Evolution of porosity, crack density, and CMAS penetration in thermal barrier coatings subjected to burner rig testing, J. Am. Ceram. Soc. 102 (2019) 6163–6175. https://doi.org/10.1111/jace.16465.

[146] G.M. Ingo, G. Padeletti, Segregation aspects at the fracture surfaces of 8 wt.% yttria-zirconia thermal barrier coatings, Surf. Interface Anal. 21 (1994) 450–454. https://doi.org/10.1002/sia.740210623.

[147] G.M. Ingo, Combined use of XPS, XAES and SIMS for the characterization of fracture surfaces of CeO_2-Y_2O_3-ZrO_2 coatings, Appl. Surf. Sci. 70–71 (1993) 235–239. https://doi.org/10.1016/0169-4332(93)90434-D.

[148] X. Shan, L. Luo, W. Chen, Z. Zou, F. Guo, L. He, A. Zhang, X. Zhao, P. Xiao, Pore filling behavior of YSZ under CMAS attack: Implications for designing corrosion-resistant thermal barrier coatings, J. Am. Ceram. Soc. 101 (2018) 5756–5770. https://doi.org/10.1111/jace.15790.

[149] S. Morelli, S. Bursich, V. Testa, G. Bolelli, A. Miccichè, L. Lusvarghi, CMAS corrosion and thermal cycling fatigue resistance of alternative thermal barrier coating materials and architectures: A comparative evaluation, Surf. Coatings Technol. 439 (2022). https://doi.org/10.1016/j.surfcoat.2022.128433.

[150] R. Kumar, J. Wang, C. Jiang, D. Cietek, J. Favata, S. Shahbazmohamadi, J. Roth, M. Gell, E.H. Jordan, Low Thermal Conductivity Yttrium Aluminum Garnet Thermal Barrier Coatings Made by the Solution Precursor Plasma Spray: Part I—Processing and Properties, J. Therm. Spray Technol. 27 (2018) 781–793. https://doi.org/10.1007/s11666-018-0728-9.

[151] R. Naraparaju, M. Hüttermann, U. Schulz, P. Mechnich, Tailoring the EB-PVD columnar microstructure to mitigate the infiltration of CMAS in 7YSZ thermal barrier coatings, J. Eur. Ceram. Soc. 37 (2017) 261–270.

https://doi.org/10.1016/j.jeurceramsoc.2016.07.027.

[152] S. Kim, S. Lee, Y. Oh, H. Kim, B. Jang, S. Kim, Characteristics of Bulk and Coating in $Gd_{2-x}Zr_{2+x}O_{7+0.5}$ (x=0.0, 0.5, 1.0) System for Thermal Barrier Coatings, J. Korean Ceram. Soc. 53 (2016) 652–658. https://doi.org/http://dx.doi.org/10.4191/kcers.2016.53.6.652.

[153] S. Duluard, E. Delon, J. Bonino, A. Malié, A. Joulia, L. Bianchi, P. Gomez, F. Ansart, Transient and steady states of $Gd_2Zr_2O_7$ and $2ZrO_2{\cdot}Y_2O_3$ (ss) interactions with calcium magnesium aluminium silicates, J. Eur. Ceram. Soc. 39 (2019) 1451–1462. https://doi.org/https://doi.org/10.1016/j.jeurceramsoc.2018.12.016.

[154] A.A. Kulkarni, A. Goland, H. Herman, A.J. Allen, J. Ilavsky, G.G. Long, C.A. Johnson, J.A. Ruud, Microstructure-Property Correlations in Industrial Thermal Barrier Coatings, J. Am. Ceram. Soc. 87 (2004) 1294–1300. https://doi.org/10.1111/j.1151-2916.2004.tb07725.x.

[155] A. Loganathan, A.S. Gandhi, Effect of phase transformations on the fracture toughness of t' yttria stabilized zirconia, Mater. Sci. Eng. A. 556 (2012) 927–935. https://doi.org/10.1016/j.msea.2012.07.095.

[156] A.R. Krause, H.F. Garces, C.E. Herrmann, N.P. Padture, Resistance of $2ZrO_2{\cdot}Y_2O_3$ top coat in thermal/environmental barrier coatings to calcia-magnesia-aluminosilicate attack at 1500 °C, J. Am. Ceram. Soc. 100 (2017) 3175–3187. https://doi.org/10.1111/jace.14854.

[157] V. Viswanathan, G. Dwivedi, S. Sampath, Engineered Multilayer Thermal Barrier Coatings for Enhanced Durability and Functional Performance, J. Am. Ceram. Soc. 97 (2014) 2770–2778. https://doi.org/10.1111/jace.13033.

[158] H. Hayashi, T. Saitou, N. Maruyama, H. Inaba, K. Kawamura, M. Mori, Thermal expansion coefficient of yttria stabilized zirconia for various yttria contents, Solid State Ionics. 176 (2005) 613–619. https://doi.org/10.1016/j.ssi.2004.08.021.

[159] C.J. Li, H. Dong, H. Ding, G.J. Yang, C.X. Li, The Correlation of the TBC Lifetimes in Burner Cycling Test with Thermal Gradient and Furnace Isothermal Cycling Test by TGO Effects, J. Therm. Spray Technol. 26 (2017) 378–387. https://doi.org/10.1007/s11666-017-0530-0.

[160] R.S. Lima, B.M.H. Guerreiro, M. Aghasibeig, Microstructural Characterization and Room-Temperature Erosion Behavior of As-Deposited SPS, EB-PVD and APS YSZ-Based TBCs, J. Therm. Spray Technol. 28 (2019) 223–232. https://doi.org/10.1007/s11666-018-0763-6.

[161] N. Curry, S. Mahade, A. Venkat, S. Joshi, Erosion performance of suspension plasma spray thermal barrier coatings - A comparison with state of art coatings, Surf. Coatings Technol. 437 (2022) 128311. https://doi.org/10.1016/j.surfcoat.2022.128311.

[162] W. Algenaid, A. Ganvir, R.F. Calinas, J. Varghese, K. V. Rajulapati, S. Joshi, Influence of microstructure on the erosion behaviour of suspension plasma sprayed thermal barrier coatings, Surf. Coatings Technol. 375 (2019) 86–99. https://doi.org/10.1016/j.surfcoat.2019.06.075.

Acknowledgments

Throughout the writing of this dissertation I have received a great deal of support and assistance.

My gratitude goes to my my supervisors, Prof. Luca Lusvarghi and Dr. Giovanni Bolelli, for their technical support and for giving me the opportunity to increase my knowledge in material science and, at the same time, to improve my social and communication skills.

I would like to express my gratitude to all the staff of the company Lincotek S.p.A for their help in providing raw materials and deposition facilities. They gave me the opportunity to be part of this project. Thanks to Simone Bursich: his friendly collaboration and his valuable advice have contributed to finalize the research.

My sincere thanks also go to Dr. Omar Ligabue who has contributed to make this research work possible.

I would like to thank Claudia, Caterina, Alle, Fre, Ale, and Luca for their moral support, suggestions and help with laboratory testing. It has been a great fun to be around you.

I must thank Veronica for many reasons. Too many to be all mentioned here. I couldn't have asked for a better friend/colleague to work with over the last few years.

Thanks to Miky for his support, comforting words, and encouragement. *Ok, grazie mille.*

Thanks to my family for being always by my side, though far apart. I love you much.

My heartfelt thanks to all of you.